Impact of pathogenic SMS2 variants on lipid landscapes and membrane properties along the secretory pathway

Dissertation

submitted to the

Department of Biology/Chemistry, University of Osnabrück, Germany

to obtain the degree "*Doctor Rerum Naturalium"* (Dr. rer. nat.)

Presented by

Tolulope Tolu Victor Sokoya

Born in Lagos, Nigeria

Osnabrück, March 2022

Referees:

Prof. Dr. Joost Holthuis
Molecular Cell Biology, University of Osnabrück

Prof. Dr. Jacob Piehler
Biophysics, University of Osnabrück

For I know the plans I have for you, declares the Lord, plans to prosper you and not to harm you, plans to give you hope and a future.

Jeremiah 29:11

SUMMARY

Sphingomyelin (SM) is a major component of mammalian cell membranes. Its bulk production in the *trans*-Golgi provides a thermodynamic trap for cholesterol synthesized in the ER to promote the formation of a SM/sterol concentration gradient along the secretory pathway. This gradient marks a fundamental transition in physical membrane properties that helps specify organelle identity and function. A previous study identified mutations in SM synthase SMS2 as the underlying cause of a hereditary form of osteoporosis and skeletal dysplasia. This work shows that two missense SMS2 variants linked to the most severe bone phenotype, p.I62S and p.M64R, retain full enzymatic activity but are unable to leave the ER owing to a defective autonomous ER export signal. Consequently, bulk production of SM is mistargeted to the ER, the site for *de novo* synthesis of the SM precursor ceramide. Combining organellar lipidomics with the application of lipid reporters, I find that cells harboring these pathogenic SMS2 variants accumulate plasma membrane-like SM levels in the ER and display a disrupted SM asymmetry at the plasma membrane, presumably due to a constitutive SM scrambling in the ER. These aberrant SM distributions also occur in patient-derived fibroblasts and are accompanied by significant imbalances in cholesterol organization and lipid order along the secretory pathway. Moreover, I find that a more common nonsense SMS2 variant associated with a milder bone phenotype, p.R50X, yields a truncated but catalytically active enzyme that is mistargeted to an early Golgi compartment. Collectively, these data indicate that pathogenic SMS2 variants undermine the capacity of cells to uphold nonrandom lipid distributions in the secretory pathway that may be critical for the bone forming activity of osteogenic cells.

ZUSAMMENFASSUNG

Sphingomyelin (SM) ist ein wichtiger Teil der Membranen von Säugetieren. Dessen hauptsächliche Produktion im *trans*-Golgi stellt eine thermodynamische Falle für Cholesterin dar, das im ER synthetisiert wird, um die Bildung eines SM/Sterol-Konzentrationsgradienten entlang des Sekretionsweges zu fördern. Dieser Gradient markiert einen grundlegenden Übergang in den physikalischen Membraneigenschaften, der zur Identifizierung und Funktion der Organellen beiträgt. Eine frühere Studie hat Mutationen in der SM Synthase SMS2 als zugrundeliegende Ursache für eine erbliche Variante von Osteoporose und skeletaler Dysplasie identifiziert. Diese Arbeit zeigt, dass zwei Missense-SMS2-Varianten, die mit dem gravierendsten Knochenphänotyp verbunden sind, p.I62S und p.M64R, die volle enzymatische Aktivität beibehalten, aber nicht in der Lage sind, das ER aufgrund eines defekten autonomen ER-Exportsignals zu verlassen. Dadurch wird die Produktion von SM ins ER verlagert, wo auch die *de-novo* Synthese von Ceramid, dem SM Vorläufer, stattfindet. Durch die Kombination organellarer Lipidomik sowie durch die Anwendung von Lipidreportern habe ich herausgefunden, dass Zellen, die diese pathogenen SMS2-Varianten besitzen, plasmamembranähnliche SM-Konzentrationen im ER akkumulieren und eine gestörte SM-Asymmetrie an der Plasmamembran aufweisen, was vermutlich auf ein konstitutives SM-Scrambling im ER zurückzuführen ist. Diese abweichenden SM-Verteilungen treten auch in von Patienten stammenden Fibroblasten auf und werden von erheblichen Ungleichgewichten in der Cholesterinorganisation und der Lipidanordnung entlang des Sekretionsweges begleitet. Darüber hinaus habe ich herausgefunden, dass eine häufigere Nonsense-Variante von SMS2, die mit einem milderen Knochenphänotyp verbunden ist, p.R50X, zu einem verkürzten, aber katalytisch aktiven Enzym führt, das in einem frühen Golgi-Kompartiment fehllokalisiert ist. Zusammengenommen deuten diese Daten daraufhin, dass pathogene SMS2 Varianten die zelluläre Fähigkeit zur Aufrechterhaltung nicht-zufälliger Lipidverteilungen im sekretorischen Weg, welche möglicherweise für die knochenbildende Aktivität osteogener Zellen entscheidend sind, stören.

TABLE OF CONTENTS

1. INTRODUCTION

1.1. Membrane lipid diversity

Lipid membranes are not just passive barriers but functional entities that define the boundaries of subcellular organelles and those between a cell and its environment. They host about one-third of proteins, making them the sites for a major portion of cellular bioactivity (Krogh *et al.*, 2001). Membrane lipids have a wide array of functions, including as energy storage molecules, structural components, signalling molecules, organelle identifiers and recruitment platforms for proteins. Cells make massive amount of lipids with thousands of different lipids catalogued by lipidomic profiling strategies (Wenk, 2010). The reason for this diversity is not completely understood. Membrane lipid diversity can be categorized into two. First, chemical diversity which describes the enormous diversity in the structure of lipids, and second, compositional diversity which describes diversity in the type and abundance of lipids between species, tissues, cells, organelles, and between leaflets of the same bilayer (Harayama and Reizmann, 2018).

Structurally, lipids differ in characteristics such as head group, charge, number, length, and saturation state of acyl chains. These structural properties influence the biophysical nature of membranes contributing to membrane curvature, thickness, charge, and fluidity. Membrane curvature depends on the molecular geometry of its constituent lipids, with cone-shaped lipids having a propensity to form non-bilayer structures and cylindrical-shaped lipids forming bilayers (**Fig. 1a**; de Kroon *et al.*, 2013). The fluidity of a membrane is dependent on the transition temperature of its constituent lipids, which is largely a function of the length and saturation state of hydrophobic chains. Generally, longer acyl chains are correlated with decreased fluidity and unsaturated acyl chains to increased fluidity (**Fig. 1b;** Renne and de Kroon, 2018). The physicochemical integrity of biological membranes is under tight regulation. Perturbations by temperature or dietary supplementations leads to significant acyl chain remodelling (Klose *et al.*, 2012; Levental *et al.*, 2020).

Phospholipids (glycerophospholipids) and sphingolipids, stabilized by sterols constitute the framework of biological membranes. Phospholipids are a class of lipids typically consisting of a glycerol backbone, a phosphate head group and two hydrophobic acyl chains attached to the sn-1 and sn-2 positions. Phospholipids are diverse in their head group component, as well as in the length and degree of *cis*-unsaturation of their acyl chains. Head groups of phospholipids can be anionic in phosphatidylinositol (PI) and phosphatidylserine (PS) or zwitterionic in phosphatidylcholine (PC) and phosphatidylethanolamine (PE). PC accounts for more than 50 % of phospholipids in eukaryotic membranes and usually contains one cis-unsaturated acyl chain. Owing to its large polar head group and two acyl chains (**Fig. 1a)**, PC has a cylindrical shape and spontaneously forms liquid crystalline bilayers making it the ideal lipid to preserve the fluidity and stability of cellular membranes. On the other hand, PE takes on a conical shape due to its small polar head group and imposes negative curvature stress on membranes, a property important for membrane budding, fission and fusion events (**Fig. 1a**; van Meer, Voelker and Feigenson, 2008; Wang and Tontonoz, 2019). PE as well as the mitochondrial lipid, cardiolipin cannot form bilayers on their own. The nonbilayer propensity of PE and CL is proportional to the length and unsaturation of their

acyl chains. Although relatively low in abundance, PI and PS are important determinants of membrane surface charge and influence the interaction of membranes with positively charged integral and peripheral membrane proteins (Magalhaes and Glogauer, 2010). Mono-acyl phospholipids contain one acyl chain and include lysophosphatidic acid and lysophosphatidylcholine which easily leave membranes and perform signalling functions (Meyer zu Heringdorf and Jakobs, 2007).

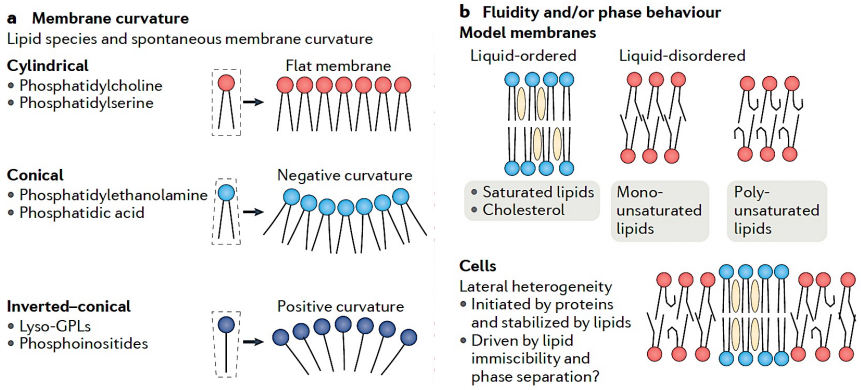

Fig. 1. Lipid structure subserves lipid function.
(**a**) Membrane curvature is determined by lipid shape. Lipids (e.g., phosphatidylcholine, phosphatidylserine) with equal area of head group to acyl chain ratio form cylindrical shape and zero membrane curvature. Lipids (e.g., phosphatidylethanolamine and phosphatidic acid) with small area of head group to acyl chain ratio form conical shape and induce negative curvature while lipids (e.g., lyso-glycerophospholipids, phosphoinositides) with large area of head group to acyl chain ratio induce positive curvature. (**b**) Membrane fluidity is largely a function of the unsaturation of acyl chains. Saturated acyl chains and cholesterol generate liquid-ordered, less fluid membranes and unsaturated lipids introduce kinks generating liquid-disordered, fluid membranes. Lateral heterogeneities in membranes are thought to be initiated by lipids and stabilized by proteins. Figure adapted from Harayama and Riezman (2018).

Sphingolipids are a distinct class of lipids that differ from glycerophospholipids in that they have a sphingoid base backbone instead of a glycerol. Sphingoid bases, also known as long-chain bases are amino alcohol precursors of ceramide and complex sphingolipids (Quinville *et al.*, 2021). Sphingosine, sphinganine and their phosphorylated derivatives are relatively low abundant, bioactive sphingoid bases that play important roles in signalling (Rosen *et al.*, 2013; Blaho *et al.*, 2014). The head group of sphingolipids can be hydroxyl in ceramide, phosphoethanolamine in ceramidephosphoethanolamine (CPE) or phosphocholine in sphingomyelin. Glycosphingolipids contain monosaccharides such as glucose in glucosylceramide (GlcCer), galactose in galactosylceramide (GalCer) or other mono-, di-, and higher oligosaccharides. Sphingolipids typically contain *N*-acylated saturated or *trans*-unsaturated acyl chains which form taller and narrower cylinders than those of PC giving them the propensity to form more tightly packed membranes (Slotte, 2013). The tightly packed immobile acyl chains of sphingolipids are fluidized by sterols (**Fig. 1b**). Cholesterol is the most abundant mammalian sterol and consists of a hydrophobic core consisting of a short hydrocarbon tail with four fused benzene rings and a hydroxyl group. According to the “umbrella” model, the preferential mixing of sterols with sphingolipids is caused by shielding of the non-polar sterol by the sphingolipid headgroup (Huang and

Fegeinson, 1999). Cholesterol has also been shown to modulate and enhance the intermolecular hydrogen bonding of SM (Bjokorborn *et al.*, 2011).

1.2. Lipids display non-random distributions in cells

Lipids are neither randomly nor uniformly distributed in organellar membranes. Each organelle is decorated by characteristic lipids in specific orientation that confer complementary properties which in turn define organellar identity and subserve organellar function. Two factors are crucial in determining the lipid composition of organelles: local lipid metabolism and selective lipid transport. Lipid metabolism is highly compartmentalized and as such local lipid metabolism is the first determinant of the lipid composition of an organelle. For example, the inner mitochondrial membrane contains the machinery for the synthesis and remodelling of cardiolipin, a lipid that is almost exclusively found in the mitochondria where it functions in respiration and energy conversion (**Fig. 2;** Paradies *et al*., 2019). Another example is the local metabolism at the plasma membrane (PM) which produces a pool of bioactive lipids that mediate diverse signalling roles and serve in cell recognition (**Fig. 2**; Hannun and Obeid 2008).

However, local metabolism alone does not explain the distribution of lipids as organelles contain lipids synthesized elsewhere and delivered by lipid transport (Vance, 2015; van Meer and de Kroon, 2011). For instance, the PM is not equipped with machinery to produce sterol and depends almost entirely on transport mechanisms for its full complement of sterol. In another vein, the sequential steps in the synthesis of some lipids take place in different organelle. For example, the machinery for the synthesis of most sphingolipids is localized in the Golgi complex, yet ceramide, the precursor of sphingolipids is produced in the endoplasmic reticulum (ER; **Fig. 2**). In addition, organelles also display non-random distribution in their acyl chain unsaturation with saturated acyl chains being enriched along the secretory pathway at the expense of monounsaturated acyl chains (Ernst *et al.*, 2016).

Another layer of non-random lipid composition is in the individual leaflet of the same membrane-bound organelle (Clarke *et al.,* 2020). This phenomenon known as lipid asymmetry describes the orientation of lipids towards or away from the cytosol. Lipids are asymmetrically distributed between the two leaflets of the Golgi, PM and lyso/endosomal membranes with PS and PE enriched in the cytosolic leaflet and, SM and glycosphingolipids enriched on the non-cytosolic or luminal leaflet (Kobayashi and Mennon, 2018). Lipid asymmetry confers the two leaflets of a membrane with distinct biophysical properties and varying functions. For instance, under physiological conditions, PS is exclusively located in the inner leaflet of the PM, where it serves as an essential co-factor for PKC and Na/K ATPase (Newton and Keranen, 1994; Habeck *et al.*, 2017). However, PS externalization serves as a “eat me” signal for the clearance of apoptotic corpses or “clot” signal in blood coagulation (Fadeel and Xue, 2009; Leventis and Grinstein, 2010). Organelles are also asymmetric in the degree of unsaturation of acyl chains with the membrane of red blood cells containing twofold more double bonds in the cytoplasmic versus exoplasmic leaflet (Lorent *et al.,* 2020).

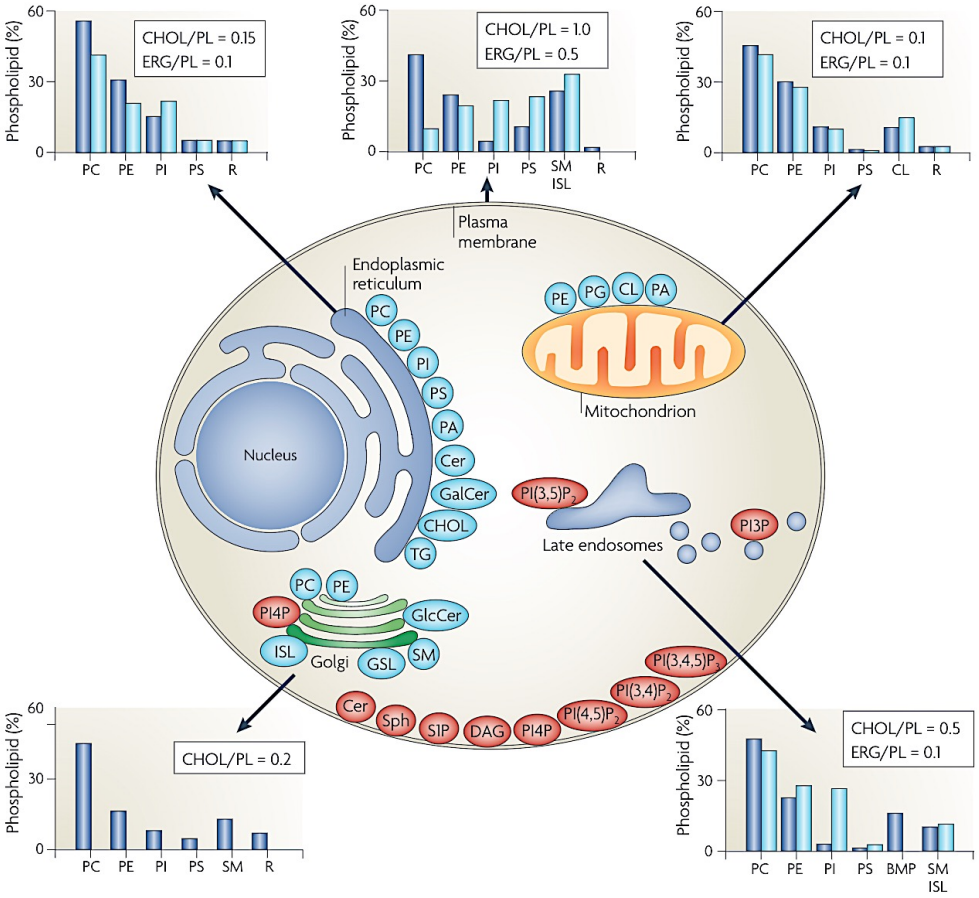

Fig. 2. Lipids display nonrandom distribution in cells.
Cellular membranes differ in their lipid composition. The lipid compositional data (shown in graphs) are expressed as a percentage of the total phospholipid (PL) in mammals (*blue*) and yeast (*light blue*). As a measure of sterol content, the molar ratio of cholesterol (CHOL; in mammals) and ergosterol (ERG; in yeast) to phospholipid is shown. The site of synthesis of the major phospholipids (*blue*) and lipids that are involved in signalling and organelle recognition pathways (*red*) are depicted. The major glycerophospholipids assembled in the endoplasmic reticulum (ER) are phosphatidylcholine (PC), phosphatidylethanolamine (PE), phosphatidylinositol (PI), phosphatidylserine (PS), and phosphatidic acid (PA). In addition, the ER synthesizes Cer, galactosylceramide (GalCer), cholesterol, and ergosterol. Both the ER and lipid droplets participate in steryl ester and triacylglycerol (TAG) synthesis. The Golgi is the assembly site of sphingomyelin (SM), complex glycosphingolipids (GSLs), and yeast inositol sphingolipid (ISL) synthesis. Some amount of PC and PE are synthesized in the Golgi. Cardiolipin (CL), PE, and PA comprise 45% of PL in the mitochondria. PG, phosphatidylglycerol; $PI(3,5)P_2$, phosphatidylinositol-(3,5)-bisphosphate; $PI(4,5)P_2$, phosphatidylinositol-(4,5)-bisphosphate; $PI(3,4,5)P_3$, phosphatidylinositol-(3,4,5)-trisphosphate; PI4P, phosphatidylinositol-4-phosphate; R, remaining lipids; S1P, sphingosine-1-phosphate; Sph, sphingosine. Figure adapted from van Meer, Voelker and Feigenson, (2008).

1.3. Organellar lipid codes

While some rare lipids such as phosphoinositides contribute to organelle function by binding specific proteins, numerous recognition processes within or on organellar bilayers are specified by physicochemical membrane properties that are determined by the collective behavior of bulk lipids. Particularly striking are the lipid-induced changes in bilayer-thickness, lipid packing density, and surface charge that segregate early from late

organelles in the secretory pathway (Bigay and Antonny, 2012; Holthuis and Menon, 2014). On one hand, the ER membrane is characterized by low sphingolipid and sterol content, and a neutral cytosolic surface charge. On the other hand, the PM is characterized by a high sphingolipid and sterol content, and a highly negative cytosolic surface charge (**Fig. 3**, Holthuis and Mennon, 2014). The Golgi serves as an important transition between these two physically and functionally distinct regions- the thin and loosely packed ER and *cis*-Golgi, and the thick and tightly packed *trans*-Golgi and PM.

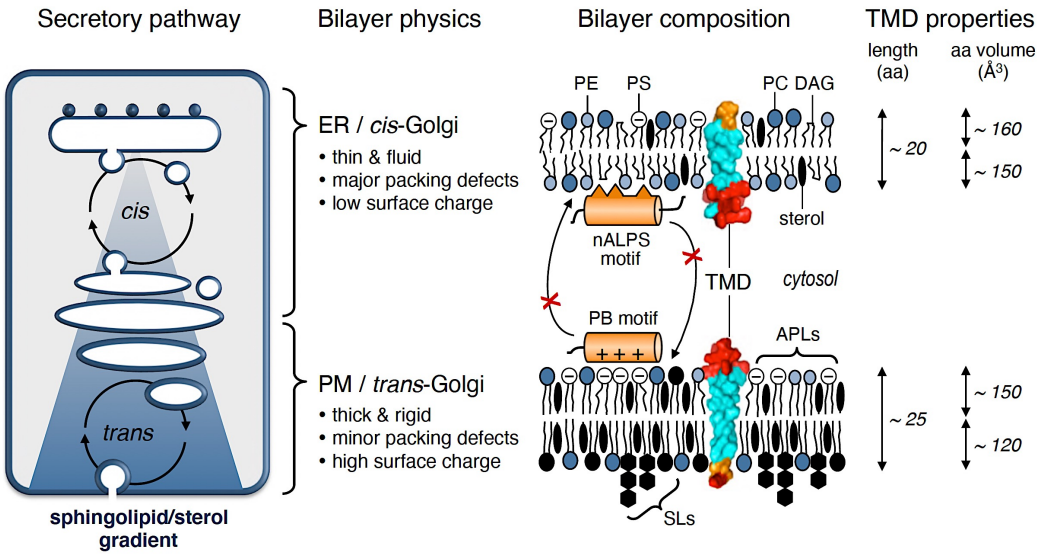

Figure 3. Early and late secretory organelles display contrasting lipid compositions and physical properties.
Physical membrane properties are influenced by lipid composition. Lipids with short and unsaturated acyl chains, predominantly glycerophospholipids, promote fluidity. Thickness is promoted by sphingolipids (SLs), which have long and saturated acyl chains, and by sterols, which order and stretch the acyl chains. Lipids with unsaturated acyl chains and/or small head groups, such as phosphatidylethanolamine (PE) or diacylglycerol (DAG), increase packing defects of the membrane. Surface charge is determined by the chemical properties of the lipid head group, which is neutral in phosphatidylcholine (PC) and negative in phosphatidylserine (PS). The ER has a thin bilayer, loose lipid packing and neutral cytosolic surface charge, adapted for its biogenic function. On the other hand, the plasma membrane has a thick bilayer, tight lipid packing and negative cytosolic surface charge, adapted for its barrier function. These contrasting physical properties are reflected in the length and geometry of the transmembrane domains (TMDs) of ER- and PM-resident proteins, and permit organelle-specific recruitment of peripheral membrane proteins (orange cylinders). APLs, aminophospholipid translocases; nALPS, neutral Arf lipid packing sensor; PB, polybasic. Figure adapted from Panatala, Hennrich and Holthuis, (2015).

These contrasting lipid codes are reflected in the length and geometry of the membrane spans of organelle-resident proteins (**Fig.3**; Sharpe *et al.*, 2010) and facilitate organelle-specific recruitment of peripheral membrane proteins involved in protein secretion or cell signaling such as the small GTPases Sar1 and K-Ras that control COPII vesicle formation at the ER and cell proliferation at the PM, respectively (**Fig.3**; Bigay and Antonny, 2012; Magdeleine *et al.*, 2016; Zhou and Hancock, 2018). Cells exploit diverse strategies to preserve the unique lipid codes of their secretory organelles against intermixing by vesicular traffic. These include cytoplasmic transfer proteins that allow specific lipids to bypass vesicular connections by facilitating their monomeric exchange at contact sites between

different organelles (Wong *et al*., 2019). In addition, organelles like the ER harbor membrane property sensors that provide feedback to the lipid metabolic network to preserve their characteristic lipid composition when exposed to stress or metabolic insults (Radanović *et al*., 2018; Levental *et al*., 2020). These mechanisms, combined with the lipid remodeling and filter function of the Golgi complex, enable cells to keep the unique lipid mixtures and membrane properties of their secretory organelles within an appropriate range.

Sterols and sphingolipids are prime examples of bulk membrane lipids that are unevenly distributed between secretory organelles (van Meer, Voelker and Feigenson, 2008; Holthuis and Menon, 2014). Sterols are rare in the ER but abundant in the trans-Golgi and PM. Like sterols, sphingolipids are concentrated in the PM, while their levels are low in the ER. Sphingomyelin (SM) is the most abundant sphingolipid in mammalian cells. The bulk of SM is synthesized in the lumen of the *trans*-Golgi from ceramides supplied by the ER and delivered by vesicular traffic to the PM, where it accumulates in the exoplasmic leaflet (Hanada *et al*., 2003). SM is the preferred binding partner of cholesterol (Slotte, 2013), and approximately one-third of the total cholesterol pool in the PM is sequestered by SM (Das *et al*., 2014; Endapally *et al*., 2019). Besides influencing cellular cholesterol homeostasis, SM along with cholesterol contributes to an enhanced packing density and thickening of the lipid bilayer of the trans-Golgi and PM. This, in turn, modulates protein sorting by hydrophobic mismatching of membrane spans (Munro, 1995; Quiroga *et al*., 2013). Thus, SM produced in the lumen of the Golgi and at the outer leaflet of the PM provides a thermodynamic trap for cholesterol synthesized in the ER, contributing to the formation of a SM/sterol gradient along the secretory pathway. In addition to the SM gradient along the secretory pathway, is its asymmetric disposition across the bilayers of the *trans*-Golgi, the PM, and late endosomal organelles. SM displays a strict asymmetric distribution with more than 90% of PM SM in its inner leaflet (Lorent *et al.,* 2020). Thus, two SM gradients exist in cells, one along the secretory pathway and the other across the bilayer of late secretory organelles. These nonrandom SM gradients are important for maintaining ER- and PM-specific lipid codes. While organellar lipid codes are thought to be fundamental for many physiological processes, there is paucity of experimental data to support this concept.

1.4. The sphingomyelin biosynthetic pathway

Given the central role that SM plays in the maintenance of organellar lipid codes, it is important to consider how its biosynthesis occurs. The first committed step in the *de novo* synthesis of sphingomyelin begins on the cytosolic surface of the ER with the condensation of the amino acid, L-serine, and an activated fatty acyl coenzyme A (CoA), palmitoyl-CoA yielding 3-ketodihydrosphingosine (**Fig. 4**). This condensation reaction is catalyzed by serine palmitoyl transferase. 3-ketodihydrosphingosine is rapidly reduced to dihydrosphingosine, which in turn is converted to dihydroceramide by the action of the sphingosine N-acyltransferase, dihydroceramide synthase. Dihydroceramide is then dehydrated by dihydroceramide desaturase (DES1) to produce ceramide, the precursor of all sphingolipids. Ceramide is exported out of the ER by vesicular and non-vesicular means for the formation of other sphingolipids including sphingomyelin (**Fig. 4**; Hannun and Obeid, 2018).

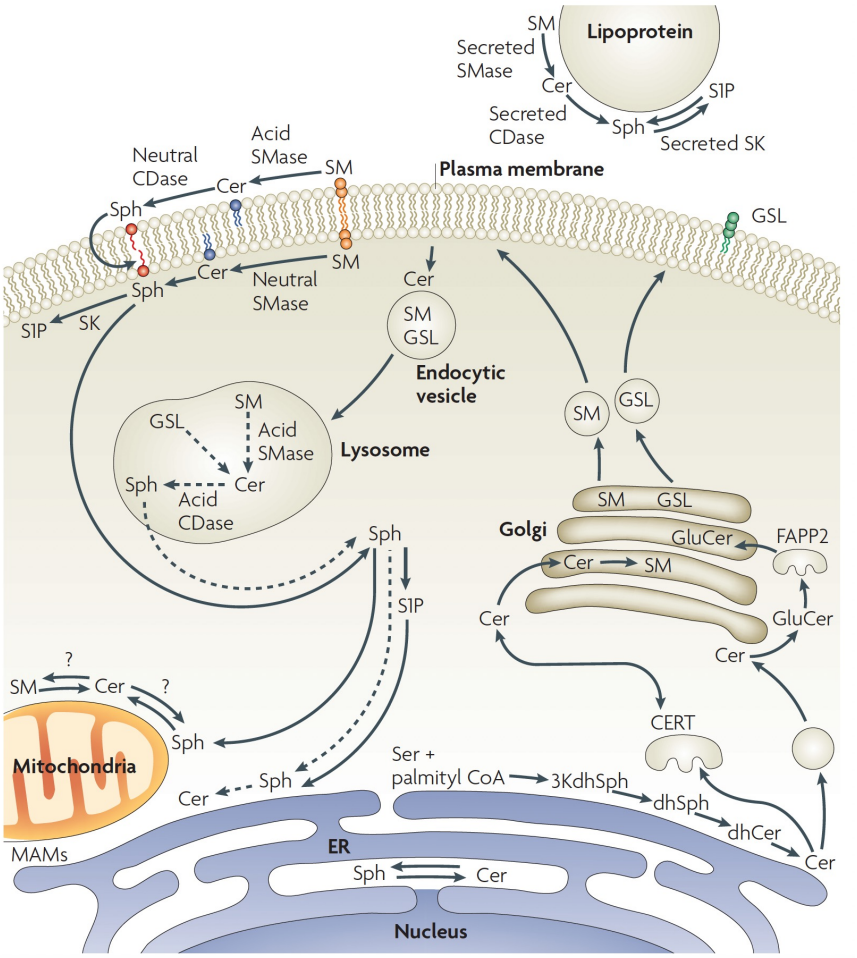

Figure 4. The sphingolipid metabolic network.
The *de novo* synthesis of all sphingolipids begins in the endoplasmic reticulum with the condensation of serine and activated palmitate to yield 3-ketodihydrosphingosine (3KdhSph) which is reduced to dihydrosphingosine (dhSph) and in turn converted to dihydroceramide (dhCer). Desaturation of dhCer by desaturases yields ceramide. Ceramide is transported to the Golgi by either the ceramide transfer protein (CERT) for sphingomyelin (SM) production or through the concerted action of vesicular transport machinery and FAPP2 for the synthesis of glucosylceramide (GlcCer), the precursor of complex glycosphingolipids (GSLs). SM and GSLs are delivered to the plasma membrane by vesicular transport. Sphingomyelin synthases (SMSs), SMS1 at the Golgi and SMS2 at the plasma membrane generate SM from ceramide (not shown). Acid sphingomyelinase (SMase) on the outer leaflet and neutral SMases on the inner leaflet of the plasma membrane convert SM to ceramide. SM and GlcCer are internalized through the endosomal pathway and reach the lysosomal compartment, where they are degraded by the actions of SMases and glucosidases. Salvage pathways of sphingolipid synthesis are depicted in dashed lines. CDase, ceramidase; Sph, sphingosine; S1P, sphingosine-1-phosphate; MAMs, mitochondria associated membranes. Figure adapted from Hannun and Obeid (2008).

SM biosynthesis in mammals is mediated by two enzymes, SM synthase 1 (SMS1) and SMS2. Both enzymes act as phosphatidylcholine (PC):ceramide phosphocholine transferase, which catalyzes the transfer of the phosphorylcholine head group from PC onto ceramide to generate SM and diacylglycerol (DAG) (Huitema *et al.*, 2004). SMS1 resides in the trans-Golgi, and its deficiency in mice causes mitochondrial dysfunction and defective

insulin secretion (Yano *et al*., 2011, 2013). SMS2 resides both in the trans-Golgi and at the PM. Its deficiency ameliorates diet-induced obesity and insulin resistance (Li *et al*., 2011; Mitsutake *et al.,* 2011; Sugimoto *et al.,* 2016; Kim *et al*., 2018). Removal of SMS1 or SMS2 has only a minor impact on ceramide, DAG and SM pools in tissues or cells, and the mechanisms underlying the phenotypes observed in SMS1 and SMS2 knockout mice are not well understood. Besides SMS1 and SMS2, mammalian cells contain an ER-resident and SMS-related protein (SMSr), which displays phospholipase C activity and synthesizes trace amounts of the SM analog ceramide phosphoethanolamine (Vacaru *et al.*, 2009; Murakami and Sakane, 2021). The physiological role of SMSr remains to be established.

The topology and location of both SMS1 and SMS2 are key for the maintenance of nonrandom SM distributions. Firstly, both enzymes have their active sites on the luminal or extracytosolic leaflet of the Golgi and PM respectively, contributing to the asymmetric transbilayer distribution of SM. Secondly, both enzymes are strategically located in late secretory organelles facilitating the formation of a SM concentration gradient along the secretory pathway and in endosomal recycling compartments (Huitema *et al.,* 2004; Tafesse *et al.,* 2007).

1.5. Biological implications of sphingomyelin asymmetry

Why cells keep a strict SM asymmetry in late secretory organelles is not completely understood. An asymmetric distribution of SM has been shown to be relevant for the repair of damaged organelles. Recent studies uncovered that SM becomes rapidly exposed to the cytosol upon injury to endomembrane or the PM by pathogenic bacteria, toxins, or a laser (Ellison *et al.,* 2020; Niekamp *et al.,* 2022). The rapid scrambling of SM in response to damage is calcium-dependent and mediated at the PM by the calcium-activated TMEM16F scramblase (Zhang *et al.,* 2020; Niekamp *et al.,* 2022). Subsequent conversion of SM to ceramides by neutral SMases on the cytosolic surface of injured lysosomes promotes their repair, presumably by driving an inverse budding of the damaged membrane area in a process akin to ESCRT-mediated formation of intraluminal vesicles. Remarkably, the SM-dependent repair of these membrane lesions precedes and functions independently of the ESCRT-dependent membrane repair machinery. Blocking the turnover of cytosolic SM renders cells more sensitive to lysosome-damaging toxins but promoting SM turnover by neutral sphingomyelinase-2 (nSMase2) promotes the repair of injured lysosomes (Niekamp *et al.,* 2022). These findings collectively suggest that the strict SM asymmetry that marks late secretory and endosomal organelles reflects a fundamental role for cytosolically-exposed SM in safeguarding the functional integrity of these organelles. Thus, defects in the organization of the SM biosynthetic pathway may have far-reaching patho-physiological consequences.

1.6. Mutations in sphingomyelin synthase SMS2 cause osteoporosis

Osteoporosis with calvarial doughnut lesions (OP-CDL: OMIM #126550) is an autosomal dominant skeletal disorder characterized by low bone mineral density, multiple fractures starting in childhood, sclerotic doughnut-shaped lesions in the spine and skull, and bouts of facial nerve palsy (**Fig. 5**). Whole-genome sequencing of 17 affected individuals identified heterozygous mutations in *SGMS2*, a gene highly expressed in bone tissues and coding for

SMS2, as the underlying cause of the disease (**Fig. 5**; Pekkinen *et al.,* 2019). While the nonsense variant (p.R50X) was predicted to yield a truncated and catalytically dead enzyme, the missense variants (p.I62S, p.M64R) cause retention of functional SMS2 in the ER (Pekinnen *et al.,* 2019). Patients with the p.R50X variant presented with moderately severe bone fragility and multiple sclerotic skull lesions reminiscent to osteogenesis imperfecta. How p.R50X mutation contributes to OP-CDL remains to be investigated. On the other hand, patients with the p.I62S or p.M64R mutation showed more severe phenotype with severe short stature, neonatal fractures and spondylometaphyseal dysplasia (Pekinnen *et al.,* 2019; Makitie *et al.,* 2021; Basalom *et al.,* 2021). Additionally, fibroblasts of patients carrying the p.I62S or p.M64R mutation displayed an enhanced capacity for *de novo* SM production (Pekkinen *et al.,* 2019). Another independent study indicates that SMS2 in mice osteoblasts regulates osteoclast differentiation by inducing an activator of nuclear factor κB (Yoshikawa *et al.,* 2019). Collectively, these studies demonstrate that SMS2 has bone regulatory properties. It appears that the underlying cause of OP-CDL in patients with heterozygous SMS2 mutations is not a reduced cellular capacity to produce SM but rather the consequence of producing SM in the wrong location. Conceivably, bulk production of SM in the ER mediated by pathogenic SMS2 variants p.I62S or p.M64R may disrupt the lipid code of early secretory organelles, in particular, in bone cells where the enzyme is highly expressed. Addressing this may provide crucial insights into the molecular basis of OP-CDL.

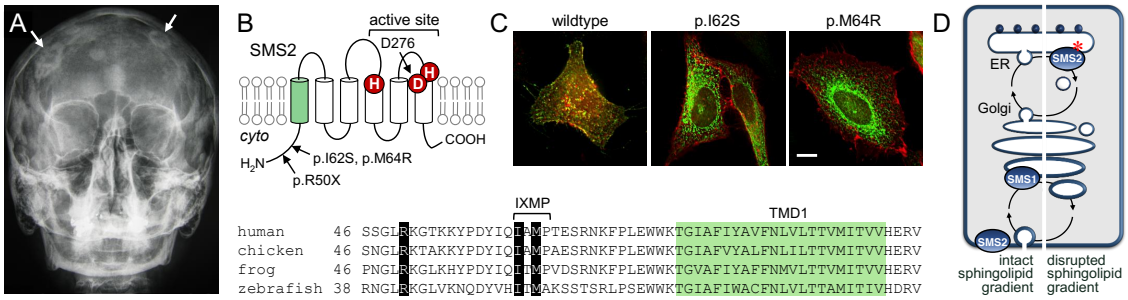

Figure 5. Osteoporosis and skeletal dysplasia caused by pathogenic variants of SMS2. (**a**) Skull radiograph of a patient with SMS2 p.R50X mutation showing extensive sclerotic lesions (arrows). (**b**) Membrane topology of SMS2 and sequence alignment of the region immediately upstream of transmembrane domain 1 (TMD1) in vertebrate SMS2 homologs. Active site residues and positions of 3 residues substituted in pathogenic SMS2 variants defective in ER export are indicated. (**c**) Immunofluorescence microscopy of HeLa cells co-expressing Flag-tagged SMS2, SMS2(I62S) or SMS2(M64R) (*green*) and mCherry-tagged PM marker (*red*). Scale bar, 10 μm. (**d**) Putative impact of a pathogenic SMS2 variant, marked with an asterisk, on the sphingolipid/cholesterol gradient along the secretory pathway. Panels a-c are adapted from Pekkinen et al. (2019).

1.7. Monitoring subcellular lipid distributions

Organellar lipidomics

Sensitive and reliable methods must be employed for the detection and quantification of lipids in whole cells and subcellular compartments. A rapidly evolving methodology is mass spectrometry (MS)-based lipidomics (Han and Gross, 2003). Advances in MS-based lipidomics has led to the uncovering of an enormous diversity of lipid species in mammalian

membranes that differ in their headgroups, acyl chains and backbones (Han and Gross, 2005; Shevchenko and Simmons, 2010). MS-based lipidomics can be coupled to liquid chromatography (LC) in which lipids are separated by LC prior to infusion into a mass spectrometer. While LC-MS is suitable for studying smaller groups of lipid classes, a more robust method of lipidomics is shotgun lipidomics which allows for a rapid, high-throughput global analysis of cellular lipidome from the direct infusion of total lipid extracts of biological samples (Yang and Han, 2016). This permits simultaneous analysis of a large group of lipid classes. Shotgun lipidomics has been used to study a variety of biological phenomena including, changes in glycerophospholipids in Huntington disease model (Vodicka *et al.,* 2015), lipidome changes in lung cancer (Marien *et al.,* 2016; Eggers *et al.,* 2020), changes to lipidome of leukemia cells induced by cationic amphiphilic drugs (Nielsen *et al.,* 2020), analysis of the Yeast lipidome (Wang *et al.,* 2020), homeoviscous adaptation as a response to dietary changes (Levental *et al.,* 2020) and PM asymmetry (Lorent *et al.,* 2020). The combination of organellar purifications with MS-based lipidomics is a powerful tool to map organellar lipidomes and annotate lipids in their native location (Hornig-Do *et al.*, 2009). By using organelle-specific membrane proteins as bait, whole organelles can be immunopurified using high affinity magnetic immunocapture. Although MS has the potential to give qualitative and quantitative information about lipid species, it cannot give direct information about the specific transbilayer orientation of lipids.

Imaging lipids in cells

To better understand the physiological role of endogenous lipids, methods must be developed that allow visualization of the precise localization and topology of lipids at the sub-micron level. One way to visualize lipids is the use of lipid analogs which are intrinsically fluorescent (cholestatrienol, dehydorergosterol), or lipid analogs with fluorescent (NBD, BODIPY) or non-florescent tags (spin-label; Kishimoto *et al.*, 2016; Kinoshito *et al.,* 2017). These tools have proven useful to investigate the intracellular organization and dynamics of sterols and sphingolipids. Alternatively, clickable lipid analogs with relatively small alkyne or azide groups at the terminal end of their acyl chains have been used to follow the metabolism of sphingolipids in live cells (Fink and Seibel, 2018; Izqueirdo and Delgado, 2018). These groups can be conjugated to a fluorophore by click-chemistry to allow visualization of the lipid. However, a major disadvantage is that these tags can alter the biophysical properties of the lipids. Recent discovery of lipid binding proteins (LBPs) has enabled direct visualization of lipids without the use of modified lipids. LBPs are mostly non-lytic versions of pore-forming toxins that directly label endogenous lipids. SM-binding proteins have been developed that enable detailed visualization of SM in the cytosolic leaflet and luminal leaflet of subcellular membranes.

Lysenin and Equinatoxin-based SM reporters

Lysenin is a 33-kDa pore-forming toxin derived from the earthworm *Eisenia fetida* that specifically binds SM with a stoichiometry of 5-6 SM molecules to 1 lysenin molecule. Although the crystal structure of lysenin predicts the presence of two phosphocholine binding sites, a combination of TLC and ELISA assays revealed that lysenin binds SM but not another phosphocholine-containing lipid, PC (Yamaji *et al.,* 1998; Ishitsuka *et al.,* 2004; De Colibus *et al.,* 2012). It has also been shown that lysenin does not bind S1P,

sphingosine, ceramides or glycerophospholipids but readily binds dihydroSM implying that the double bond at the position C4 of sphingosine in the SM backbone is not critical for its SM binding ability (Yamaji *et al.,* 1998; Kinoshita *et al.,* 2013). At physiological temperatures, lysenin oligomerizes and leads to membrane reorganization (Yamaji-Hasegawa *et al.*, 2003). An *N*-terminal truncation of lysenin (NT-lysenin) has been shown to be nontoxic and nonoligomerizable (Kiyokawa, 2005). Fluorophore-bound NT-lysenin has been used to monitor SM in model membranes (Makino *et al.*, 2015), during cell division (Abe *et al.,* 2012) and more recently to show breakage in SM asymmetry as an early event in the pathology of a gram-negative bacteria (Ellison *et al.,* 2020).

Equinatoxin II (Eqt) is a 20-kDa pore-forming toxin derived from the sea anemone, *Actinia equina* (Anderluh *et al.,* 1996; Rojko *et al.,* 2016). It binds SM but not PC, ceramide and glycolipids (Bakrac *et al.,* 2008; Makino *et al.,* 2015). Eqt preferentially binds to liposomes containing liquid ordered SM/Chol and not liquid disordered SM/DOPC in a mixture of both liposomes (Schon *et al.,* 2008). Using atomic force microscopy, it was shown that in liposomes containing SM/DOPC (1:1), Eqt did not bind to SM-rich domains but to DOPC-rich domains containing a small amount of SM. Furthermore, co-incubation of GUVs containing SM/DOPC/Chol with fluorescent lysenin and Eqt shows that both probes stain two distinct lipid domains (Makino *et al.,* 2015). Lysenin was found in SM-rich regions while Eqt was found in the surrounding liquid-disordered phase in which SM is dispersed in DOPC. This indicates that Eqt has a preference for dispersed SM as its labeling is not correlated with SM concentrations. This is contrary to lysenin which prefers clustered SM and whose labelling is qualitatively correlated with the amount of SM in the PM (Makino *et al.,* 2015).

Pore formation by Eqt begins with the binding of the protein to SM by its hydrophobic amino acid residues, an intramolecular conformational change in the protein followed by its oligomerization in the membrane. Introduction of a disulphide bridge in the double cysteine Eqt mutant (V8C, K69C) prevents the intramolecular conformational change and thus the protein's hemolytic activity without perturbing its SM binding activity under oxidized conditions (Kristan *et al.,* 2004; Rojko *et al.,* 2013). Eqt V22W mutant inhibits the transbilayer insertion of the pore-forming helix, stabilizes the protein in a membrane-bound state while retaining SM recognition (Guiterrez-Aguirre *et al.,* 2004; Tanaka *et al.,* 2015). By targeting hydrophobic amino acid residues which are responsible for the initial binding of Eqt to membranes independent of SM, a Y108I mutation was found that increases the specificity of Eqt for SM (**Fig. 6a and b**; Deng *et al.,* 2016). Conversely, a Y113I mutation abolished all membrane binding activity. Purified Eqt (V22W, Y108I) stained the cell surface, and this staining was abolished by sphingomyelinase treatment (**Fig. 6c;** Deng *et al.,* 2016). Eqt (V22W, Y108I) hereafter referred to as EqtSM binds to membranes with a minimum of 10 mol% SM and Eqt (V22W, Y113I) hereafter referred to as EqtSol is a soluble version of the protein having all its membrane binding activity ablated. To visualize Eqt proteins in the secretory pathway, a human growth hormone (hGH) signal sequence was fused to its N-terminus and an oxGFP to its C terminus. These probes have been used to observe the forward trafficking of a specific set of SM containing vesicles from the *trans*-Golgi in HeLa cells (Deng *et al.,* 2016). Expressing Eqt probes lacking the hGH signal

sequence ($EqtSM_{cyto}$ and $EqtSol_{cyto}$) in HeLa cells has proven valuable in unravelling a role for cytosolically-exposed SM in the repair of damaged membranes. Expressing $EqtSM_{cyto}$ in HeLa cells leads to a diffused cytosolic distribution in line with a strict asymmetry of SM. However, desecration of the membrane by toxins or pathogens leads to recruitment of $EqtSM_{cyto}$ to these damage sites, indicative of breakage in SM asymmetry (Niekamp *et al.,* 2022).

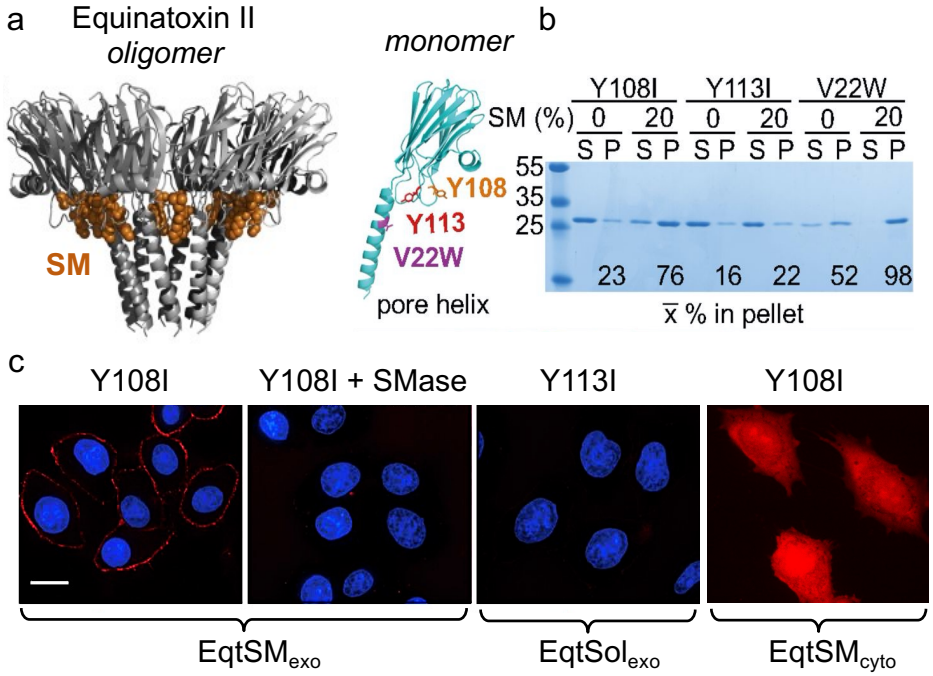

Figure 6. Equinatoxin is a sphingomyelin biosensor.
(**a**) Left: the oligomeric structure of an actinoporin, Fragecatoxin C is shown with its protomers labelled in grey and SM molecules presented as orange spheres. Right: a monomer with engineered residues is rendered. Residue V22 (*purple*) on the N-terminal helix which is critical for pore formation was changed to tryptophan. An additional mutation Y108I (*orange*) was found to potentiate SM binding yielding EqtSM. A mutation that abolishes SM binding Y113I (*red*) was introduced to yield EqtSol. (**b**) The indicated Eqt mutants were incubated with liposomes containing 20% SM or phosphatidylcholine (and 20% cholesterol), and the liposomes were collected by centrifugation. Bound pellet (P) and unbound supernatant (S) fractions were visualized by Coomassie blue staining and quantified. The mean values of three independent experiments are shown. The Y108 and Y113 mutants also include the V22W mutation. Note that Eqt (V22W, Y108I) binds avidly to liposomes containing 20 mol% SM. (**c**) Recombinant FLAG-tagged EqtSM or EqtSol was incubated with HeLa cells that had been incubated with SMase or mock-treated. Cells were then washed, fixed, and incubated with anti-FLAG and labeled secondary antibodies. Note that SMase treatment abolished Eqt binding. Epitope-tagged Eqt ($EqtSM_{cyto}$) were expressed in HeLa cells. The diffused cytosolic staining observed is consistent with a strict SM asymmetry across organellar membranes. Panel A was adapted from Rojko et al. (2016) and Deng et al., (2016). Panels b and c were adapted from Deng et al. (2016).

Perfingolysin O-based cholesterol reporters

Over the last two decades, cholesterol binding proteins have been developed to directly probe the organization of PM cholesterol and to distinguish cholesterol in the cytosolic and luminal leaflets of membranes. Perfingolysin O *θ*-toxin (PFO) is derived from the anaerobic bacteria, *Clostridium perfringens* (Rossjohn *et al.,* 1997). This toxin performs its lytic activity by binding to cholesterol in the exofacial leaflet of the PM and subsequently forming a pore

due to dimerization and oligomerization (Dang *et al.,* 2005; Hotze *et al.,* 2012). PFO comprises of 4 domains. Whilst domains 1-3 are essential for pore formation, domain four is largely responsible for the binding of the hydroxyl group of cholesterol (Dang *et al.,* 2005; Hueck *et al.,* 2007; Sato *et al.,* 2013). Domain 4 (D4) is a 13 KDa protein representing the smallest portion of PFO that has been shown to sufficiently bind cholesterol without cytotoxicity (Ramachandran *et al.,* 2002; Hueck *et al.,* 2007). D4 accomplishes its association with cholesterol via its short hydrophobic loops, making little or no contact with adjacent protein monomers, thus, a limited interaction with the bilayer is sufficient for cholesterol binding. (Ramachandran *et al.,* 2002; Johnson and Hueck, 2014). Purified mCherry or GFP-tagged D4 has been used to visualize and quantify exoplasmic cholesterol in the PM of living cells (Carquin *et al.,* 2015, Maekawa and Fairn, 2015). Additionally, D4 has been utilized to visualize cholesterol in the cytosolic leaflets of membranes by expression of mCherry tagged D4 in the cytosol of cells (Koponen *et al.,* 2020; Maekawa *et al.,* 2016) and by microinjection of D4 variants (Liu *et al.,* 2017). Combining exofacial D4 labelling with its cytosolic labelling is useful in distinguishing transbilayer distribution of cholesterol at the PM (Abe *et al.,* 2012; Liu *et al.,* 2017).

However, the accessibility of D4 for cholesterol depends on the concentration of cholesterol in the exofacial and cytosolic leaflets (Endapally *et al.,* 2019; Maekawa, 2017). For example, cytosolically expressed D4 localizes to the PM of HeLa and MA-10 cells but not CHO cells. (Abe *et al.,* 2012; Venugopal *et al.,* 2016). Interestingly, increasing the concentration of cholesterol in the PM of CHO cells by exogenously added cholesterol increased D4 binding suggesting that the binding of D4 reaches a threshold and that this is not uniform across mammalian cells (Maekawa and Fairn, 2015). D4 has been shown to bind to model membranes containing more than 30-35 mol% of cholesterol (Ishitsuka *et al.,* 2011). Thus, the ability of D4 to bind to membranes might be influenced by glycerophospholipid or sphingolipid composition and the concentration of cholesterol in the membrane (Das *et al*., 2013; Endapally *et al.,* 2019). A point mutation, D434S in domain 4 has been found to decrease the threshold of PFO for cholesterol binding. D4H (D434S) binds to liposomes with 20 mol% (Maekawa and Fairn, 2015). mCherry-tagged D4H localizes to the inner leaflet of the PM when expressed in Raw, HeLa, Madin-Darby canine kidney cells as well as CHO cells suggesting that increased affinity of D4H to cholesterol enables improved recognition of cholesterol in the cytosolic leaflet of the PM (Cho *et al.,* 2016; Maekawa and Fairn, 2015; Maekawa *et al.,* 2016).

2. SCOPE

Sphingomyelin (SM) is a major component of mammalian cell membranes. Its bulk production in the *trans*-Golgi provides a thermodynamic trap for cholesterol synthesized in the ER to promote the formation of a SM/sterol concentration gradient along the secretory pathway. This gradient marks a fundamental transition in physical membrane properties that helps specify organelle identity and function. Consequently, cells should avoid lipid mixing between early and late secretory organelles as this would undermine the functional organization of the secretory pathway. However, this fundamental concept in cell biology awaits experimental validation. Recent work identified heterozygous mutations in the gene coding for SMS2 as the underlying cause of OP-CDL, an autosomal and dominant genetic disorder resulting in osteoporosis and skeletal dysplasia. While two mutations, p.I62S and p.M64R, result in retention of a functional SMS2 enzyme in the ER, a third mutation, p.R50X, is thought to disrupt expression of a catalytically active enzyme. How these mutations lead to the development of osteoporosis is not known. The central aim of this thesis is to explore the consequences of pathogenic SMS2 variants on the lipid landscapes and membrane properties of organelles along the secretory pathway. To this end, experimental work focused on pursuing the following key objectives:

1) To establish a collection of CRISPR/Cas9 and lentiviral-transduced cell lines in which expression of pathogenic SMS2 variants p.I62S, p.M64R, and p.R50X are under control of a doxycycline-inducible promoter;

2) To directly test the ability of pathogenic SMS2 variants to mediate SM production;

3) To determine the impact of pathogenic SMS2 variants on the unique lipid mixtures and transbilayer lipid arrangements in early and late secretory compartments using organellar lipidomics and lipid reporters;

4) To investigate how cells cope with a major assault on the ER lipid code;

5) To validate results obtained with genetically-engineered cells in cell lines derived from patients diagnosed with OP-CDL.

3. MATERIALS AND METHODS

3.1. Buffers and solutions

Table 1. List of buffers

Blocking buffer 5 % non-fat milk in PBST
Bacterial lysis buffer 20 mM Na_2HPO_4/NaH_2PO_4, pH 7.4, 500 mM NaCl, and 25 mM imidazole
Fixation solution 4 % paraformaldehyde, 1 µM $CaCl_2$ and 0.1 M $MgCl_2$ (pH 7.4)
Homogenization buffer 15 mM KCl, 5 mM NaCl, 20 mM HEPES/KOH pH 7.2, 10% glycerol, 1 µg/ml aprotinin, 1 µg/ml leupeptin, 1 µg/ml pepstatin, 5 µg/ml antipain, 157 µg/ml benzamidine
5 X Laemmli Buffer 50 % glycerol, 10 % SDS, 10 % ß-mercaptoethanol, 300 mM Tris-HCl pH 6.8 and 0.025 % bromophenol blue.
PBS 137 mM NaCl, 2.7 mM KCl, 10 mM Na_2HPO_4 pH 7.4, 1.8 mM KH_2PO_4
PBST 137 mM NaCl, 2.7 mM KCl, 10 mM Na_2HPO_4 pH 7.4, 1.8 mM KH_2PO_4, 0.1 % Tween 20
Permeabilization buffer 137 mM NaCl, 2.7 mM KCl, 10 mM Na_2HPO_4 pH 7.4, 1.8 mM KH_2PO_4, 0.1 % Triton-X100 and 1 % BSA (*w/v*)
Protease Inhibitor Cocktail (1000 X) 1 µg/ml aprotinin, 1 µg/ml leupeptin,1 µg/ml pepstatin, 157 µg/ml benzamidine and 5 µg/ml antipain
SDS-PAGE running buffer 250 mM, Tris, 2 M Glycine, 1 % SDS
SuMa buffer 10 mM HEPES, 0.21 M Mannitol, 0.070 M Sucrose, pH 7.5
SuMa4 buffer 10 mM HEPES, 0.21 M Mannitol, 0.070 M Sucrose, pH 7.5, 0.5 mM DTT, 0.5 % fatty acid free BSA (*w/v*), 25 units/ml Benzonase and 1x cOmplete™ Mini, EDTA-free Protease Inhibitor Cocktail
SuMa2 buffer 10 mM HEPES, 0.21 M Mannitol, 0.070 M Sucrose, pH 7.5, 0.5 mM DTT, 0.5 % fatty acid free BSA (*w/v*)
SuMa$^+$ buffer 10 mM HEPES, 0.21 M Mannitol, 0.070 M Sucrose, pH 7.5, 0.5 mM DTT
TGM Buffer 192 mM glycine, 25 mM Tris pH 8.3, 20 % methanol (*v/v*)
Triton lysis buffer 1% Triton X-100, 150 mM NaCl, 20 mM Tris pH 7.5, 1 mM EDTA, 1 µg/ml aprotinin, 1 µg/ml leupeptin, 1 µg/ml pepstatin, 5 µg/ml antipain and 1 mM benzamidine.
Quenching solution 50 mM NH_4Cl in PBS

3.2. Chemical reagents and antibodies

All chemicals were purchased from AppliChem (Germany), BioRad (USA), Carl Roth (Germany), Enzo Life Sciences (USA), Merck (USA), Sigma Aldrich (USA) and Thermo Fischer Scientific (USA). Dulbecco's modified Eagle's medium (DMEM; 4.5 g/l glucose), fetal calf serum (FCS), and trypsin (0.05 %)/EDTA (0.02 %) were obtained from PAN Biotech (Germany). Opti-MEM reduced serum medium without phenol red was from Thermo Fisher Scientific (USA). LLOME was from Bachem, 4000725 and Brefeldin A was from Thermo Fisher Scientific, 00-4506. Puromycin and methyl-β-cyclodextrin (mβCD) were from Sigma Aldrich (P8833, C4555). Doxycycline (Sigma Aldrich, D891) was used at a concentration of 1 µg/ml for all experiments. G418 was from Pan Biotech (P06-16210P). LD540 dye was a kind gift from Christoph Thiele (University of Bonn, Germany) and was described previously (Spandl *et al*., 2009). NR12A and NR-ER_{Cl} kindly provided by Andrey Klymchenko (University of Strasbourg, France) were described previously (DanylChuk *et al.,* 2021). Clickable sphingosine (2S,3R,4E)-2-amino-4-octadecen-17-yne-1,3-diol was prepared by Sergei Korneev (manuscript in preparation; University of Osnabrück, Germany). Oligonucleotides were ordered from Biolegio (The Netherlands). Buffers and antibodies used in this work are listed in **Table 1** and **Table 2** respectively.

3.3. DNA constructs

pcDNA3.1(+) encoding N-terminal FLAG-tagged SMS2, $SMS2^{I62S}$ and $SMS2^{M64R}$ were described previously (Pekinnen *et al*., 2019). Open reading frame (ORF) of FLAG-tagged SMSr-$SMS2_{11-77}$ was synthetically prepared (IDT, Belgium) and inserted into pcDNA3.1(+) using BamHI and NotI restriction sites. Single mutations were subsequently generated by site directed mutagenesis. To prepare C-terminal tagged SMS2-HA constructs, primers were designed to add 1 x HA tag to c-terminus of FLAG-SMS2 using pcDNA3.1-FLAG-SMS2 as template. To prepare lentiviral expression constructs, first ORF of FLAG-tagged SMS2 was PCR amplified using pcDNA3.1-SMS2 as template (Pekinnen *et al.*, 2019). FLAG-SMS2 or FLAG-SMS2-HA was inserted into pENTR™11 (Invitrogen, A10467) using the BamHI and NotI restriction sites. Single and double mutations were generated from pENTR™11-SMS2 constructs by site directed mutagenesis. Next SMS2 inserts were transferred into lentiviral expression vector pInducer20 by Gateway cloning (Addgene, 44012) according to the manufacturer's instructions. Primers used for introduction of single and double mutations and primers used for other cloning steps are listed in **Table 4**. Expression constructs encoding 3xFLAG-tagged-pET28a-Eqt-SM, GFP-tagged $EqtSM_{SS}$ (pN1-$EqtSM_{SS}$-oxGFP) and $EqtSol_{SS}$ (pN1- $EqtSol_{SS}$-oxGFP) have been previously described (Deng et al., 2016). Expression constructs encoding GFP-tagged $EqtSM_{cyto}$ (pN1-$EqtSM_{cyto}$-oxGFP), $EqtSOL_{cyto}$ (pN1-$EqtSOL_{cyto}$-oxGFP) and mkate-tagged $EqtSM_{cyto}$ (pN1-$EqtSM_{cyto}$-mkate) have been previously described (Niekamp *et al.,* 2022). Mammalian expression construct encoding mCherry tagged VAP-A has been previously described (Jain *et al.*, 2020). GFP tagged Sec16L (pEGFP-C1-Sec16L) was from the lab of Benjamin Glick (Bhattacharyya and Glick 2007). Expression construct encoding D4H-mCherry (pN1-D4H-mcherry) sterol reporter, a generous gift from Gregory Fairn (University of Toronto, Canada) was described previously (Maekawa and Fairn, 2015). All plasmids used in this work are listen in **Table 3**.

3.4. Mammalian cell culture and transfection

Human cervical carcinoma HeLa (ATCC CCL-2), Human osteosarcoma epithelial cells U2OS (ATCC HTB-96), Human Embryonic Kidney 293 transformed with the simian virus 40 large T antigen HEK293T (ATCC CRL-3216) and patient-derived skin fibroblasts cells (Pekinnen *et al.*, 2019) were cultured in high glucose Dulbecco's modified Eagle's medium (DMEM) containing 10 % FBS. Cells were transfected with DNA constructs using Lipofectamine 3000 (Thermo Fisher Scientific, L3000001) according to the manufacturer's instructions.

3.5. Generation of HeLa ΔSMS1/2 cell line

To generate SMS1 and SMS2 double knockout in HeLa cells (HeLa ΔSMS1/2), we used the CRISPR/Cas9 system (Ma, Zhang and Huang, 2014). CRISPR/Cas9 plasmids with a mix of three different gRNA per gene and the corresponding HDR plasmids commercially available from Santa Cruz (sc-403382 and sc-405416) were used. SgRNA sequences are listed in **Table 5**. HeLa cells transfected with SMS2 constructs were grown in medium containing 2 µg/ml puromycin 48h post-transfection. After 1-2 weeks, single, drug-resistant colonies were picked, expanded, and analyzed for SMS2 expression by immunoblot analysis. A SMS1/2 double knockout cell line (clone #11) was generated by transfecting ΔSMS2 clone #25 with SMS1 constructs following ejection of the puromycin selectable marker using Cre vector (Santa Cruz, sc-418923) according to the manufacturer's instructions. Successful knock out of SMS1 was confirmed by metabolic labelling with 4 µM of clickable sphingosine (2S, 3R, 4E)-2-amino-octadec-4-en-17-yne-1,3-diol (clickSph).

3.6. Generation of lentiviral transduced cell lines

HeLa ΔSMS1/2 cells stably expressing doxycycline-inducible versions of *N*-terminal FLAG-tagged SMS2, SMS2^{D276A}, SMS2^{I62S}, SMS2$^{I62S/D276A}$, SMS2^{M64R}, SMS2$^{M64R/D276A}$ were generated by lentiviral transduction of HeLa ΔSMS1/2. Low passage HEK293T cells were co-transfected with pInducer20-FLAG-SMS2 doxycycline-inducible expression constructs and packaging vectors psPAX2 (Addgene, 12260) and pMD2.G (Addgene, 12259). Culture medium was changed 6 h post-transfection. After 48 h, the lentivirus-containing medium was harvested, passed through a 0.45 µm filter, mixed 1:1 with DMEM containing 8 µg/ml polybrene (Sigma-Aldrich; TR-1003) and used to infect HeLa ΔSMS1/2 cells. 24 hours post-infection, growth medium was replaced with DMEM containing 1 mg/ml G418 and selective medium was changed daily. After 5 days, positively transduced cells were analyzed for doxycycline-dependent expression of FLAG-SMS2 variants by immunoblot analysis, immunofluorescence microscopy and metabolic labeling with clickSph as described below. HeLa ΔSMS1/2 cells stably expressing inducible versions of *N*-terminal HA-tagged SMS2, SMS2^{D276A}, SMS2^{M64A}, SMS2^{R50X}, SMS2$^{R50X/D276A}$, SMS2$^{R50X/M64A}$ were generated and analyzed using the same approach.

3.7. Metabolic labelling and TLC analysis

Cells were cultivated with 4 µM clickable sphingosine in Opti-MEM reduced serum medium without phenol red (Gibco, 11058) for 24 h. Next, cells were washed with PBS, harvested, and subjected to Bligh and Dyer lipid extraction method (Bligh and Dyer, 1959). Dried lipid

films were click reacted in a 40 µl reaction mix containing 0.45 mM fluorogenic dye 3-azido-7-hydroxycoumarin (Jena Bioscience, CLK-FA047), 1.4 mM Cu(I)tetra(acetonitrile) tetrafluoroborate and 66 % EtOH:$CHCl_3$:CH_3CN (66:19:16, v:v:v). Reaction mixtures were incubated 4 h at 40 °C followed by 12 h at 12 °C. Click reaction products were applied at 120 nl/s to NANO-ADAMANT HP-TLC plates (Macherey-Nagel, Germany) with a CAMAG Linomat 5 TLC sampler (CAMAG, Switzerland). The TLC plate was developed in $CHCl_3$:MeOH:H_2O:AcOH (65:25:4:1, v:v:v:v) using a CAMAG ADC2 automatic TLC developer (CAMAG, Switzerland). The coumarin-derivatized lipids were analyzed using a ChemiDoc XRS+ with UV-transillumination and Image Lab Software (BioRad, USA).

3.8. Immunostaining and fixed cell imaging

Fluorescence images of fixed cells were taken with either a DeltaVision Elite Imaging System (GE Health Sciences, USA) or Leica DM5500B microscope (Leica, Germany) as indicated. DeltaVision Elite imaging system (GE healthcare) on an inverted olympus IX-71 microscope with 60X oil objective was used with the following fluorochromes: DAPI (λex=390 nm and λem=435 nm), FITC (λex=475 nm and λem=523 nm), TRITC (λex=542 nm and λem=545 nm), and Cy5 (λex=632 nm and λem=676 nm). Leica microscope with 63 X oil objective or 40 X oil objective was used with the following fluorochromes: DAPI (λex=360 nm and λem=460 nm) GFP (λex=395 nm and λem=509 nm) and FM-64 (λex=550 nm and λem=570 nm). For fixed cell imaging, cells on coverslips were fixed in 4 % PFA for 15 min. After quenching in 50 mM ammonium chloride, cells were permeabilized with permeabilization buffer [PBS containing 0.3 % (v/v) Triton-X100 and 1 % (w/v) BSA] for 15 min. Next, cells were sequentially immunostained with primary and secondary antibodies for 2 hr and 1 hr respectively. In between antibody incubation, cells were washed 3 times with permeabilization buffer. Nuclei were counterstained with DAPI. Coverslips were mounted onto glass slides using ProLong Gold Antifade Reagent (Thermo Fisher Scientific, USA). For localization experiments with $EqtSM_{cyto}$ positive structures, in all cases, HeLa ΔSMS1/2 cells stably transduced with doxycycline-inducible FLAG-tagged $SMS2^{M64R}$ were transfected with $EqtSM_{cyto}$-GFP, except for TGN46 where cells were transfected with expression construct encoding mKate-tagged $EqtSM_{cyto}$ and in the case of Sec16L, where cells were co-transfected with mKate-tagged $EqtSM_{cyto}$ and GFP-tagged Sec16L.

3.9. Live cell imaging

Live cell images were obtained with Zeiss Cell Observer Spinning Disc Confocal Microscope equipped with a TempModule S1 temperature control unit, a Yokogawa Spinning Disc CSU-X1a 5000 Unit, a Evolve EMCDD camera (Photonics, Tucson), a motorized xyz-stage PZ-2000 XYZ (Applied Scientific Instrumentation) and an Alpha Plan-Apochromat x 63 (NA 1.46) oil immersion objective. The following filter combinations were used: blue emission with BP 445/50, green emission with BP 525/50, orange emission BP 605/70. All images were acquired using Zeiss Zen 2012 acquisition software. For hypotonic swelling assay, U2OS cells seeded in a µ-Slide 8 well glass bottom chamber (Ibidi; 80827) were co-transfected with FLAG-tagged $SMS2^{M64R}$ or $SMS2^{M64R/D276A}$, mCherry-tagged VAPA and luminal GFP-tagged $EqtSM_{SS}$ or $EqtSol_{SS}$. 16h post-transfection, cells were imaged in 100 % Opti-MEM and subsequently after 5 min incubation in hypotonic medium (1% Opti-MEM in H_2O) at 37 °C. Patient-derived skin fibroblasts co-transfected with

mCherry-tagged VAPA and luminal GFP-tagged $EqtSM_{SS}$ or $EqtSol_{SS}$ were treated and imaged similarly as described for U2OS cells. For intracellular cholesterol localization experiments, cells transfected with D4H-mcherry were incubated for 16 h in growth medium containing 70 µg/ml 10 KDa dextran conjugated with Alexa Fluor 647 (Thermo Fisher Scientific, D22914). Next, growth medium was replaced with Opti-MEM 2 h prior to imaging. Images were deconvoluted using Huygens deconvolution (SVI, The Netherlands) and processed using Fiji software (NIH, USA).

For Nile red staining experiments, cells were washed once with PBS and incubated in 0.2 µM dye in Opti-MEM for 10 min at room temperature for NR12A or 30 min at 37 °C for $NR\text{-}ER_{Cl}$. Cells were subsequently washed 3 times with PBS and imaged in Opti-MEM. Ratiometric confocal imaging was performed on a Zeiss LSM 880 with AiryScan module using a 63X 1.4 NA oil immersion objective. Excitation was provided by a 532 nm laser, while fluorescence was detected at two spectral ranges 500−600 (I500−600) and 600−700 nm (I600−700). The ratiometric images were generated using special macros under ImageJ that divides the intensity of the I500−600 channel by that of the I600−700 channel.

3.8. Cell lysis and immunoblotting

24 h post-transfection and doxycycline induction, cells were harvested and lysed in lysis buffer (1 % TritonX-100, 1 mM EDTA pH 8.0, 150 mM NaCl, 20 mM Tris pH 7.5, and protease inhibitor cocktail (PIC; 1 µg/ml aprotinin, 1 µg/ml leupeptin, 1 µg/ml pepstatin, 5 µg/ml antipain, 157 µg/ml benzamidine). Nuclei were removed by centrifugation at 600 x g for 10 min at 4 °C. Post nuclear supernatants were collected and stored at -80 °C until use. Protein samples were mixed with 2 X Laemmli sample buffer (10 % SDS, 50 % glycerol, 10 % β-mercaptoethanol, 0.025 % bromphenol blue and 0.3 M Tris HCl, pH 6.8) and then resolved on 12 % SDS-PAGE. After gel run, proteins were transferred onto nitrocellulose membrane (0.45 µm; GE Health Sciences USA), blocked with 5 % non-fat milk solution (blocking solution) for 40 min and washed with 0.05 % Tween in PBS (PBST). Next, membrane was incubated for 2 hr with primary antibody, washed three times with PBST and incubated with secondary antibody conjugated with HRP for 45 min. Membrane was further processed for protein detection using enhanced chemiluminescence substrate (ECL; Thermo Fisher Scientific, USA) and images were taken with ChemiDoc XRS+ System (Bio-Rad, USA) and processed with Image Lab Software (Bio-Rad, USA).

3.10. Cytotoxicity assay

Cells were seeded in 96-well plate (Greiner Bio-One; 655101) at 10, 000 cells per well in DMEM supplemented with 10 % FBS at 24 h after starting the treatment. After 24 h, the medium was replaced with Opti-MEM containing 1 µg/ml doxycycline, and 24 h later mβCD was added at the indicated concentration. After 1 h, PrestoBlue HS (Thermo Fisher Scientific; P50200) was added to the well to a final concentration of 10 % (v/v) and incubated for 3.5 h at 37 ºC. Next, absorbance at 570 nm was measured with 600 nm as reference wavelength using an Infinite 200 Pro M-Plex plate reader (Tecan Lifesciences). Measurements were average of quadriplicates. To calculate relative percentage of survival, the measured value for each well (x) was subtracted by the minimum measured value (min)

and divided by the subtrahend of the average measured value of untreated cells (untreated) and the minimum measured value (min); ((x-min)/(untreated-min) *100).

3.11. Equinatoxin purification and cell labelling

FLAG tagged Equinatoxin-encoding *N*-terminal His tag pET28a expression construct was transformed in E. coli BL21 (DE3). Transformants were grown at 37 °C to early exponential phase in LB medium containing 100 µg/ml ampicillin prior to addition of 0.4 mM isopropyl β-D-1-thiogalactopyranoside. Cells were harvested 5 h after induction, then mechanically lysed in buffer consisting of 20 mM Na_2HPO4/NaH_2PO4, pH 7.4, 500 mM NaCl, and 25 mM imidazole supplemented with PIC by microtip sonication. Cleared cell extracts were applied to a HisTrap column using an AKTA Prime protein purification system (GE Healthcare, Life Sciences), and bound protein were eluted with a linear imidazole gradient. HeLa cells were incubated with 1 µM purified equinatoxin protein at room temperature for 2 min, washed with PBS, fixed and immunostained against anti-FLAG at 4 °C for 10 min and Cy2-conjugated anti-rabbit antibody at room temperature for 30 min. For flow cytometry, 500, 000 cells previously treated with doxycycline for 24 hours were taken in suspension and incubated with 1 µM Eqt-FLAG at room temperature for 2 min. Next, cells were incubated with anti-FLAG antibody for 10 min at 4 °C, washed three times with 1 % BSA in PBS, fixed in 4 % PFA for 15 min and incubated with Cy2 anti rabbit for 45 min. Cells were analyzed using a SH800 Cell Sorter (Sony Biotechnology).

3.12. Organellar purification and shot-gun MS-lipidomics

Affinity purification. 10 million cells were seeded in 15 cm dishes and cultured for 24 h in Opti-MEM reduced serum medium containing 1 µg/ml doxycycline. For ER purifications, cells were washed once in ice-cold PBS. For PM purification, cells were washed three times with ice-cold PBS and then incubated for 30 min at 4 °C in PBS containing 1 mg/ml EZ-Link-sulfo-NHS-LC-LC-Biotin (Thermo Fisher Scientific, 21338). Next, cells were washed three times with ice-cold PBS. Biotin-treated and untreated cells were scraped in ice-cold PBS, centrifuged once at 500 x g, and then twice at 1,000 x g for 5 min, 4 °C. All steps from here were performed on ice or at 4 °C. Cell pellets were re-suspended in ice-cold 10 ml SuMa buffer [10 mM Hepes, 0.21 M mannitol, 0.070 M Sucrose, pH 7.5]. After the third centrifugation step, cells were resuspended in 1 ml SuMa4 buffer [SuMa buffer supplemented with 0.5 mM DTT, 0.5 % fatty acid-free BSA (Sigma Aldrich, A3803), 25 units/ml Benzonase (Sigma Aldrich, E1014) and 1x cOmplete™ Mini, EDTA-free Protease Inhibitor Cocktail (Roche Diagnostics, 04693159001) and lysed by passages through a Balch homogenizer 20 times. The cell lysates were subsequently centrifuged at 1,500 x g for 10 min and again for 15 min to prepare the light membrane fractions (LMFs).

For the ER purification, LMFs were incubated for 45 min with rabbit anti-calnexin polyclonal antibody (Abcam, ab22595) and subsequently for 1 hr with anti-rabbit IgG MicroBeads (Miltenyi Biotec, 130-048-602), and for the PM purification, only with Streptavidin MicroBeads (Miltenyi Biotec, 130-048-102). The LMFs were then loaded onto MS Columns (Miltenyi Biotec, 130-042-201) mounted on a magnetic stand (Miltenyi Biotec, 130-042-109) and pre-equilibrated in SuMa4 buffer. The columns were washed three times with 500 µl

SuMa4 buffer and twice with 500 µl SuMa2 buffer (SuMa4 without Benzonase and PIC). Thereafter, columns were removed from the magnetic stand and elution was performed with 600 µl SuMa2 buffer. Eluate samples were equally divided for western blotting and lipidomics. All samples were centrifuged at 21,100 x g for 20 min and supernatants were discarded. Pellets were resuspended in 200 µl SuMa+ buffer (SuMa2 without BSA) and the centrifugation was repeated. Lipidomics samples were stored at -80 °C until analysis and western blot samples were dissolved in 2x Laemmli sample buffer containing 100 mM DTT and stored at -20 °C until processing.

Lipid extraction. Lipid extraction was performed as previously described (Nielsen et al., 2020) with some modifications. Briefly, samples in 200 µl 155 mM ammonium bicarbonate were mixed with 24 µl internal lipid standard mix (Nielsen et al., 2020) and 976 µl chloroform:methanol 2:1 (*v/v*). The samples were shaken in a thermomixer at 2,000 rpm and 4 °C for 15 min and centrifuged for 2 min at 2,000 x g and 4 °C. Then, the lower phase containing lipids was washed twice with 100 µl methanol and 50 µl 155 mM ammonium bicarbonate. Lower phase was then transferred to new tubes and dried in a vacuum centrifuge for 75 min, and the dried lipids were resuspended in 100 µl chloroform:methanol 1:2 (*v:v*).

Mass spectrometry. Shotgun lipidomics was performed as previously described (Nielsen et al., 2020). Lipid extracts (10 µl) were loaded in a 96 well plate and mixed with either 12.9 µl positive ionization solvent (13.3 mM ammonium acetate in propan-2-ol) or 10 µl negative ionization solvent (0.2 % (*v/v*) triethyl amine in chloroform:methanol 1:5 (*v/v*)). The samples were analyzed in the negative and positive ionization modes using Q Exactive Hybrid Quadrupole-Orbitrap mass spectrometer (Thermo Fisher Scientific, Waltham, MA) coupled to TriVersa NanoMate (Advion Biosciences, Ithaca, NY, USA). Data are reported as mol% of total lipids measured.

3.13. LC-MS/MS Lipidomics

For the LC-MS/MS analysis, cells were incubated for 24 h in Opti-MEM reduced serum medium in the absence or presence of 1µg/ml doxycycline. Then, cells were harvested in homogenization buffer (15 mM KCl, 5 mM NaCl, 20 mM HEPES/KOH pH 7.2, 10% glycerol, 1 µg/ml aprotinin, 1 µg/ml leupeptin, 1 µg/ml pepstatin, 5 µg/ml antipain, 157 µg/ml benzamidine) using a sonifier BRANSON 250. The protein in crude homogenates was determined by Bradford protein assay (BioRad, USA) and 50 µg of protein was used for a subsequent chloroform/methanol extraction. To normalize lipid concentration of lipids in the samples, homogenates were prior to the extraction spiked with lipid standards ceramide (Cer 18:1/17:0) and sphingomyelin (SM 18:1/17:0). Dried lipid extracts were dissolved in a 50:50 mixture of mobile phase A (60:40 water/acetonitrile, including 10 mM ammonium formate and 0.1 % formic acid) and mobile phase B (88:10:2 2-propanol/acetonitrile/H_20, including 2 mM ammonium formate and 0.02 % formic acid). HPLC analysis was performed on a C30 reverse-phase column (Thermo Acclaim C30, 2.1 × 250 mm, 3 µm, operated at 50° C; Thermo Fisher Scientific) connected to an HP 1100 series HPLC system (Agilent) and a QExactive*PLUS* Orbitrap mass spectrometer (Thermo Fisher Scientific) equipped with a heated electrospray ionization (HESI) probe. MS analysis was performed as

described previously (Eising, Thiele and Fröhlich, 2019). Briefly, elution was performed with a gradient of 45 min; during the first 3 min, elution started with 40 % of phase B and increased to 100 % in a linear gradient over 23 min. 100 % of B was maintained for 3 min. Afterwards, solvent B was decreased to 40 % and maintained for another 15 min for column re-equilibration. MS spectra of lipids were acquired in full-scan/data-dependent MS2 mode. The maximum injection time for full scans was 100 ms, with a target value of 3,000,000 at a resolution of 70,000 at m/z 200 and a mass range of 200–2000 m/z in both positive and negative mode. The 10 most intense ions from the survey scan were selected and fragmented with HCD with a normalized collision energy of 30. Target values for MS/MS were set at 100,000 with a maximum injection time of 50 ms at a resolution of 17,500 at m/z of 200. Peaks were analyzed using the Lipid Search algorithm (MKI, Tokyo, Japan). Peaks were defined through raw files, product ion and precursor ion accurate masses. Candidate molecular species were identified by database (>1,000,000 entries) search of positive ($+H^+$; $+NH_4^+$) or negative ion adducts ($-H^-$; $+COOH^-$). Mass tolerance was set to 5 ppm for the precursor mass. Samples were aligned within a time window and results combined in a single report. From the intensities of lipid standards and lipid classes used, data are reported as mol% of total phospholipids measured.

4. RESULTS

4.1. The IXMP motif in SMS2 is part of an autonomous ER export signal

It was previously reported that heterozygous mutations in *SGMS2* are the underlying cause of OP-CDL (Pekkinen *et al.*, 2019). The most severe bone phenotypes were associated with the missense variants p.I62S and p.M64R, which cause retention of enzymatically active SMS2 in the ER. Ile62 and Met64 are part of a conserved sequence motif, IXMP, which is located 13-14 residues upstream of the first membrane span in both SMS2 and the Golgi-resident enzyme SMS1 (**Fig. 7a, b**). The absence of the IXMP motif in the ER-resident SMS family member SMSr, suggests that this motif may be part of an ER export signal (Vacaru et al., 2009). To test this idea, Flag-tagged SMS2 constructs were generated in which the Ile or Met residue of the motif was replaced with Ser or Arg, respectively. Following transfection of the constructs in HeLa cells, the subcellular distribution of the SMS2 variants was determined by immunofluorescence microscopy using anti-Flag and anti-calnexin antibodies. In agreement with previous findings (Pekkinen *et al.*, 2019), $SMS2^{I62S}$ and $SMS2^{M64R}$ were each retained in the ER, in contrast to wildtype SMS2, which localized to the Golgi and at the plasma membrane (**Fig. 7c**).

To test whether the IXMP motif in SMS2 can mediate ER export independently of other sorting information, a Flag-tagged chimera protein was generated comprising the ER-resident SMSr protein in which the region connecting the protein's *N*-terminal SAM domain to the first membrane span was swapped against the IXMP-containing region of SMS2, yielding SMSr-$SMS2_{11\text{-}77}$ (**Fig. 7a**). Contrary to SMSr, SMSr-$SMS2_{11\text{-}77}$ localized to the Golgi complex. However, SMSr-$SMS2_{11\text{-}77}$ variants in which Ile or Met in the IXMP motif was replaced with Ser or Arg, respectively, were retained in the ER (**Fig. 7d**). Collectively, these data indicate that the IXMP motif in SMS2 is part of an autonomous ER export signal. I next asked if the Ile62Ser and Met64Arg mutations would retain a wildtype SMS2 isoform in the ER. Cells expressing FLAG-tagged SMS2 mutants did not retain a V5-tagged wildtype version in the ER (**Fig. 8**). This suggests that pathogenic SMS2 variants do not have a dominant effect on the localization of wildtype isoform.

To investigate whether ER export of SMS1 also relies on its IXMP motif, a substitution of Ile118 for Ser or Met120 for Arg in the IXMP motif of Flag-tagged SMS1 was generated. This did not interfere with the delivery of the enzyme to the Golgi (**Fig. 9b**), indicating that this process involves additional ER export signals. Combining substitutions of key residues in the IXMP with removal of the enzyme's *N*-terminal SAM domain did not disrupt ER export either. To this end, a construct was generated in which a Flag-tagged chimera protein comprising the SMSr protein in which the region linking the *N*-terminal SAM domain to the first membrane span was swapped against the IXMP-containing linker region of SMS1, yielding SMSr-$SMS1_{81\text{-}139}$ (**Fig. 9a**). SMSr-$SMS1_{81\text{-}139}$ localized to the Golgi, also when Ile or Met in the IXMP motif was replaced with Ser or Arg, respectively (**Fig. 9b**). This indicates that the region between the SAM domain and the first membrane span of SMS1 contains information that mediates ER export independently of the IXMP motif.

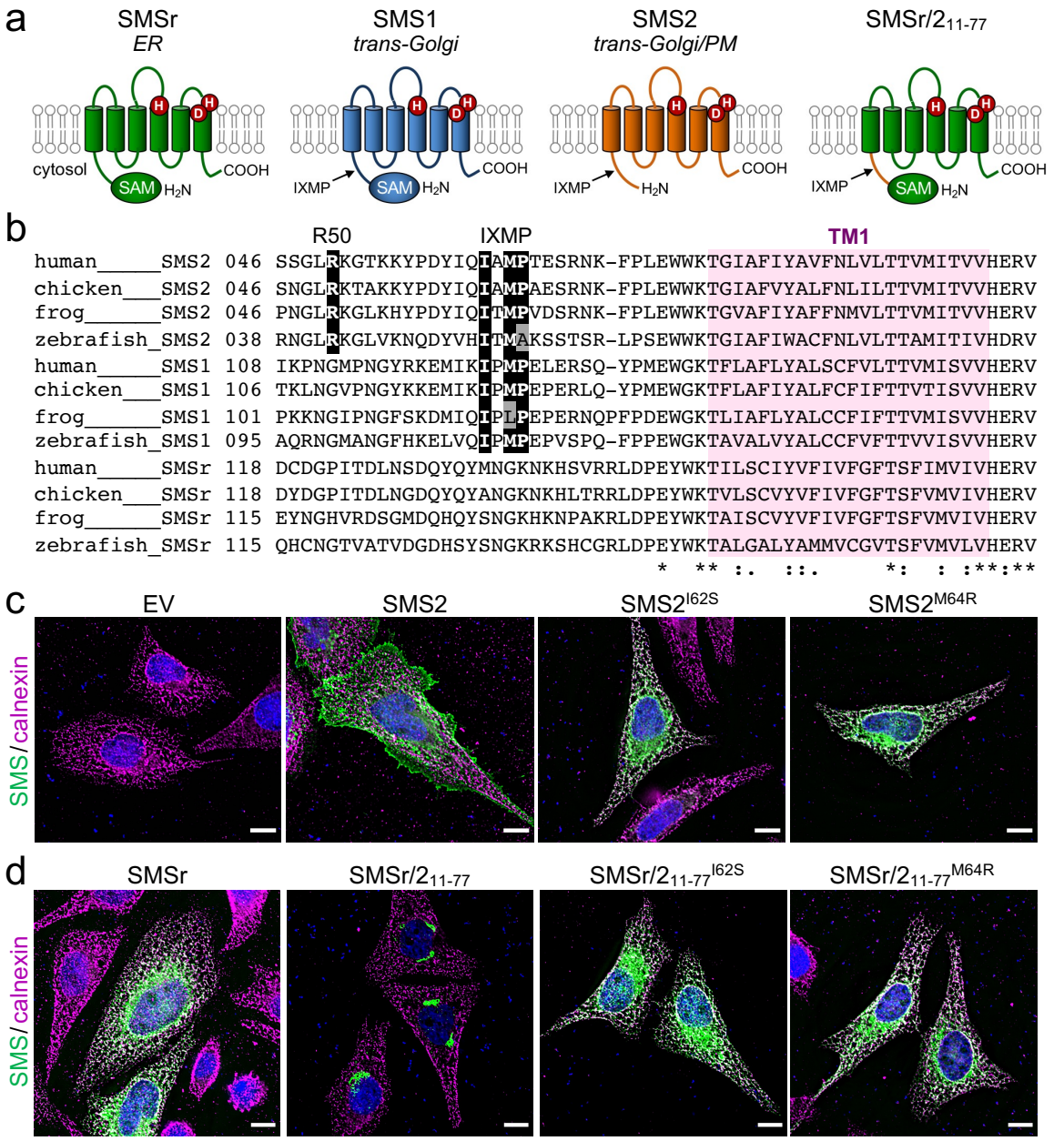

Fig. 7. SMS2 contains an autonomous ER export signal.
(**a**) Membrane topology of SMS family members and chimeric protein SMSr/$2_{11\text{-}77}$ in which the region linking the *N*-terminal SAM domain and first membrane span of SMSr was replaced with the *N*-terminal cytosolic tail of SMS2. Active site residues are marked in red. The position of a conserved IXMP sequence motif is marked by an arrow. (**b**) Sequence alignment of the region immediately upstream of the first membrane span (TM1) in vertebrate SMS family members. Note that human SMS2 residues Ile62 and Met64 are part of an IXMP sequence motif conserved in SMS1 and SMS2, but not SMSr, across different vertebrate species. (**c**) HeLa cells transfected with empty vector (EV) or Flag-tagged SMS2, $SMS2^{I62S}$ or $SMS2^{M64R}$ were fixed, immunostained with α-Flag (*green*) and α-calnexin (*magenta*) antibodies, counterstained with DAPI (*blue*) and imaged by DeltaVision microscopy. (**d**) HeLa cells transfected with Flag-tagged SMSr, SMSr/$2_{11\text{-}77}$, SMSr/$2_{11\text{-}77}^{I62S}$ or SMSr/$2_{11\text{-}77}^{M64R}$ were fixed, immunostained with α-Flag (*green*) and α-calnexin (*magenta*) antibodies, counterstained with DAPI (*blue*) and imaged by DeltaVision microscopy. Scale bars, 10 μm. Data in panels c and d were provided by Jan Parolek.

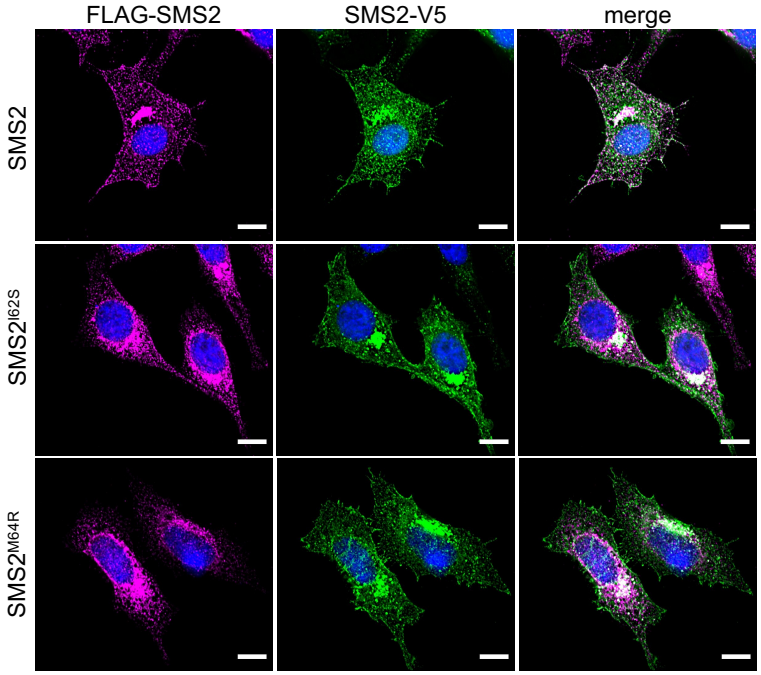

Fig. 8. Pathogenic SMS2 variants do not retain PM-resident SMS2
HeLa cells expressing Flag-tagged SMS2, SMS2^{I62S}, SMS2^{M64R} were transfected with V5-tagged SMS2 and grown for 16 h in the absence or presence of doxycycline, fixed, immunostained with V5 antibody (*magenta*), counterstained with DAPI (*blue*) and then imaged by DeltaVision microscopy. Scale bar, 10 μm.

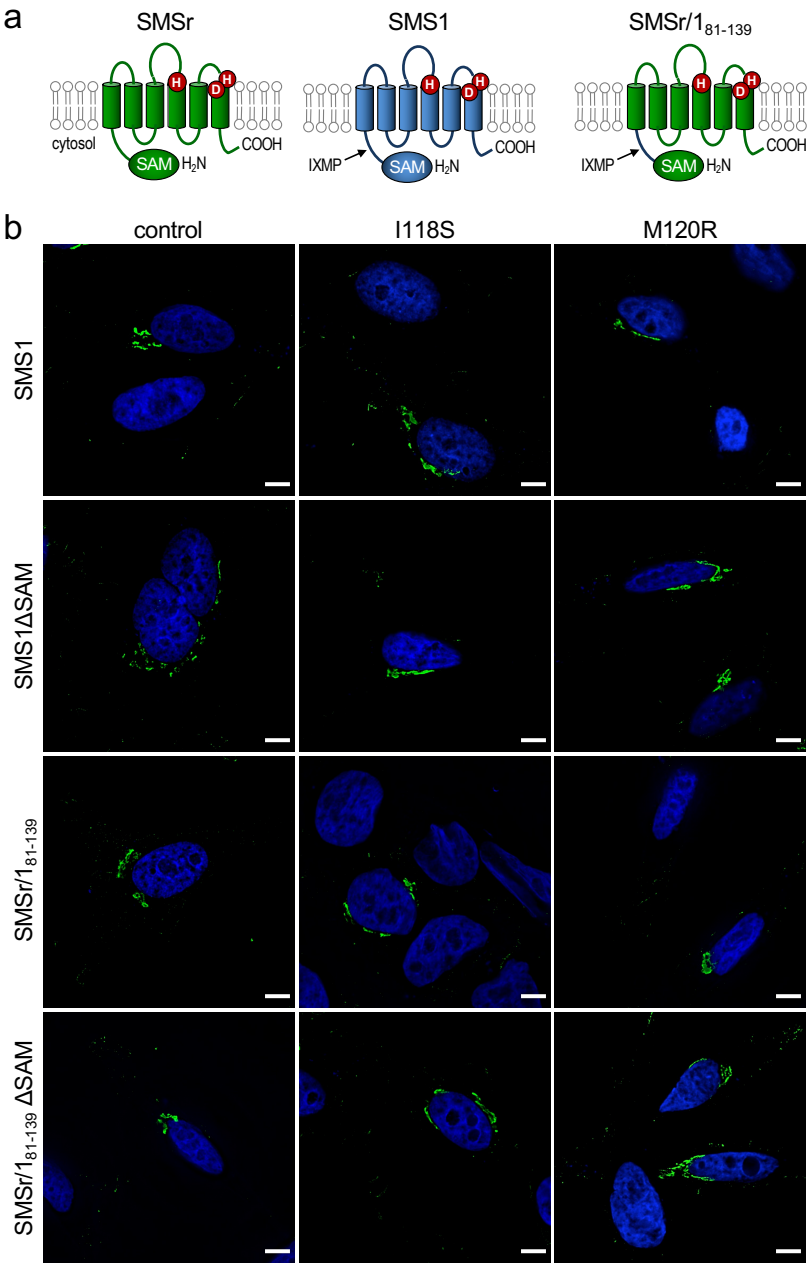

Fig. 9. The IXMP motif in SMS1 is dispensable for ER export.
(**a**) Membrane topology of SMSr, SMS1 and chimeric protein SMSr/$1_{81\text{-}139}$ in which the region linking the *N*-terminal SAM domain and first membrane span of SMSr was replaced with the corresponding, IXMP motif-containing region of SMS1. Active site residues are marked in red. (**b**) HeLa cells transfected with Flag-tagged SMS1, SMS1ΔSAM, SMSr/$1_{81\text{-}139}$ or SMSr/$1_{81\text{-}139}$ΔSAM containing an intact or mutated IXMP motif were fixed, immunostained with α-Flag antibody (*green*), counterstained with DAPI (*blue*) and imaged by DeltaVision microscopy. Scale bar, 10 μm. Data in panel b were provided by Jan Parolek.

4.2. Pathogenic SMS2 variants mediate bulk production of SM in the ER

To directly test the impact of pathogenic mutations on the biosynthetic capacity of SMS2, I generated a HeLa cell line lacking both SMS1 and SMS2 by CRISPR-Cas9 engineering (**Fig. 10a**). First, HeLa cells were transfected with CRISPR/Cas9 plasmids containing sgRNAs against SMS2. SMS2-KO clones were confirmed by immunoblotting (**Fig. 10b**).

SMS1/2 double knock out (ΔSMS1/2) clones were generated by transfection of SMS2-KO (clone number 25) with CRISPR/Cas9 plasmids containing sgRNAs against SMS1. Successful generation of ΔSMS1/2 HeLa cell line was confirmed by metabolic labelling of candidate clones with clickable sphingosine analogue (**Fig. 10c**). I next stably transduced ΔSMS1/2 cells with doxycycline-inducible lentiviral expression constructs encoding Flag-tagged SMS2, SMS2^{I62S}, SMS2^{M64R} or their enzyme dead isoforms SMS2^{D276A}, SMS2$^{I62S/D276A}$, and SMS2$^{M64R/D276A}$ respectively. Expression of recombinant protein was verified by immunoblot analysis and fluorescence microscopy of cells grown in the presence or absence of doxycycline for 16 h (**Fig. 11a and b; Fig. S1**). Next, control and doxycycline-treated cells were metabolically labelled with a clickable sphingosine analogue for 16 h, subjected to total lipid extraction, click reacted with the fluorogenic dye 3-azido-7-hydroxycoumarin and analyzed by TLC. This revealed that doxycycline-induced expression of SMS2^{I62S} and SMS2^{M64R} but not their enzyme-dead isoforms restored SM biosynthesis in ΔSMS1/2 cells to a similar level as in wildtype (**Fig. 11c**). This is in line with a previous study in which metabolic labelling experiments with ^{14}C-choline on patient-derived fibroblasts showed that heterozygous p.I62S and p.M64R mutations in SMS2 in each case causes a marked increase in the rate of *de novo* SM biosynthesis (Pekkinen *et al.*, 2019).

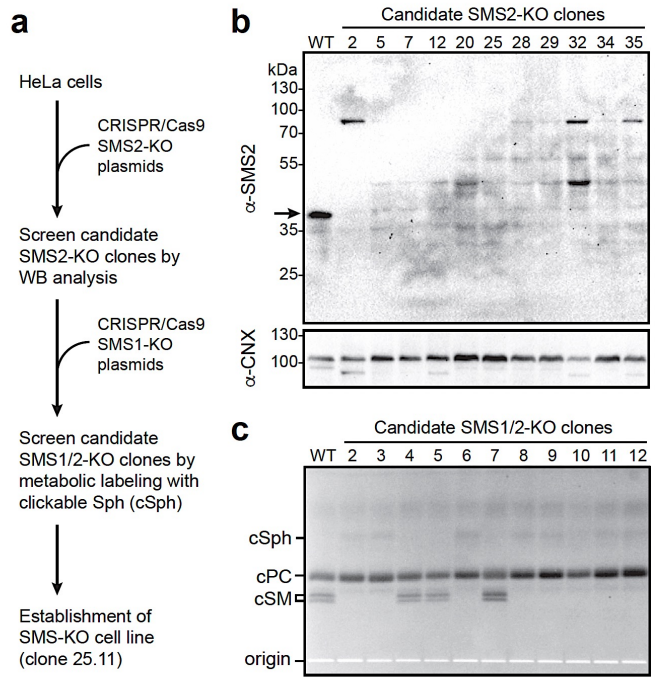

Fig. 10. Generation and characterization of ΔSMS1/2 cells.

(**a**) Schematic outline for generation of SMS1/2 double KO (ΔSMS1/2) in HeLa cells. (**b**) SMS2 removal in candidate SMS2-KO clones was verified by immunoblot analysis using antibodies against SMS2 and calnexin (CNX). Migration of immunoreactive SMS2 protein from wildtype cell extracts (WT) is marked by an arrow. (**c**) To verify complete disruption of SM biosynthesis, candidate ΔSMS1/2 clones were metabolically labeled with a clickable sphingosine analogue (4 μM, 16 h). Total lipids were extracted, click-reacted with 3-azido-7-hydroxycoumarin, separated by TLC, and analyzed by fluorescence detection. cSph, coumarin-labeled sphingosine; cPC, coumarin-labeled phosphatidylcholine; cSM, coumarin-labeled sphingomyelin.

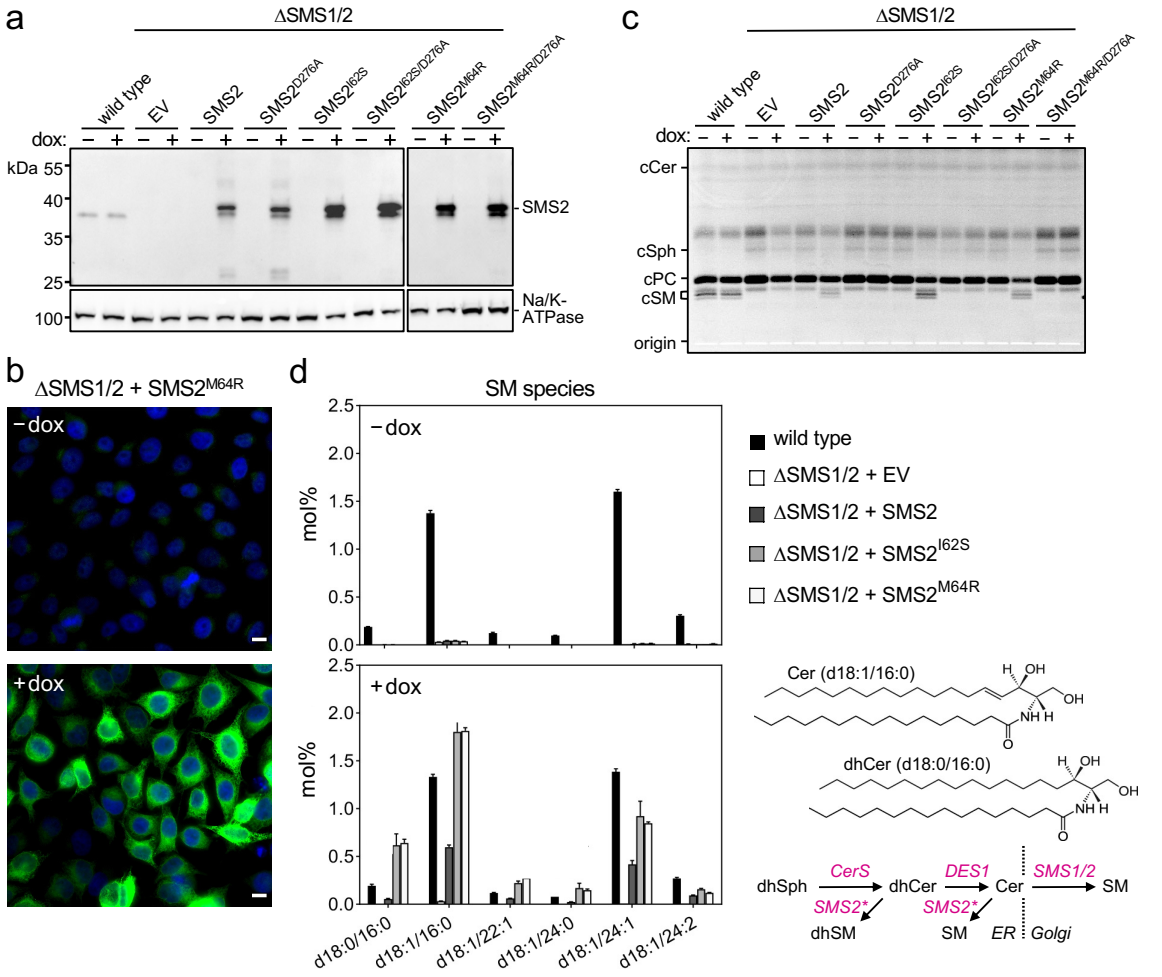

Fig. 11. Pathogenic SMS2 variants support bulk production of SM in the ER.
(**a**) HeLa ΔSMS1/2 cells stably transduced with doxycycline-inducible constructs encoding Flag-tagged SMS2, SMS2^{I62S}, SMS2^{M64R} or their enzyme-dead isoforms (D276A) were grown for 16 h in the absence or presence of doxycycline and then subjected to immunoblot analysis using α-SMS2 and α-Na/K-ATPase antibodies. Wildtype HeLa cells served as control. (**b**) ΔSMS1/2 cells stably transduced with doxycycline-inducible Flag-tagged SMS2^{M64R} were treated as in (a), fixed, immunostained with α-Flag antibody (*green*), counterstained with DAPI (*blue*) and imaged by conventional fluorescence microscopy. Scale bar, 10 μm. (**c**) Cells treated as in (a) were metabolically labelled with a clickable sphingosine analogue for 16 h, subjected to total lipid extraction, click reacted with the fluorogenic dye 3-azido-7-hydroxycoumarin and analyzed by TLC. (**d**) SM species in total lipid extracts of cells treated as in (a) were quantified by LC-MS/MS and expressed as mol% of total phospholipid analyzed. Note that the rise in dihydroSM (dhSM, d18:0/16:0) in ΔSMS1/2 cells expressing SMS2^{I62S} or SMS2^{M64R} (SMS2*) is likely due to competition between ER-resident ceramide desaturase (DES1) and SMS2* for dihydroceramide (dhCer, d18:0/16:0), which is synthesized *de novo* by ceramide synthase (CerS) from dihydrosphingosine (dhSph).

Quantitative mass spectrometry analyses of wildtype and ΔSMS1/2 cellular lipidomes revealed that removal of SMS1 and SMS2 wiped out the entire SM pool and caused a four-fold increase in glycosphingolipid (GSL) levels (**Fig. 11d**; **Fig. 12**), consistent with a competition between Golgi-resident SM and glucosylceramide (GlcCer) synthases for ceramide substrate. In ΔSMS1/2 cells transduced with pathogenic SMS2^{I62S} or SMS2^{M64R}, addition of doxycycline fully restored the SM pool.

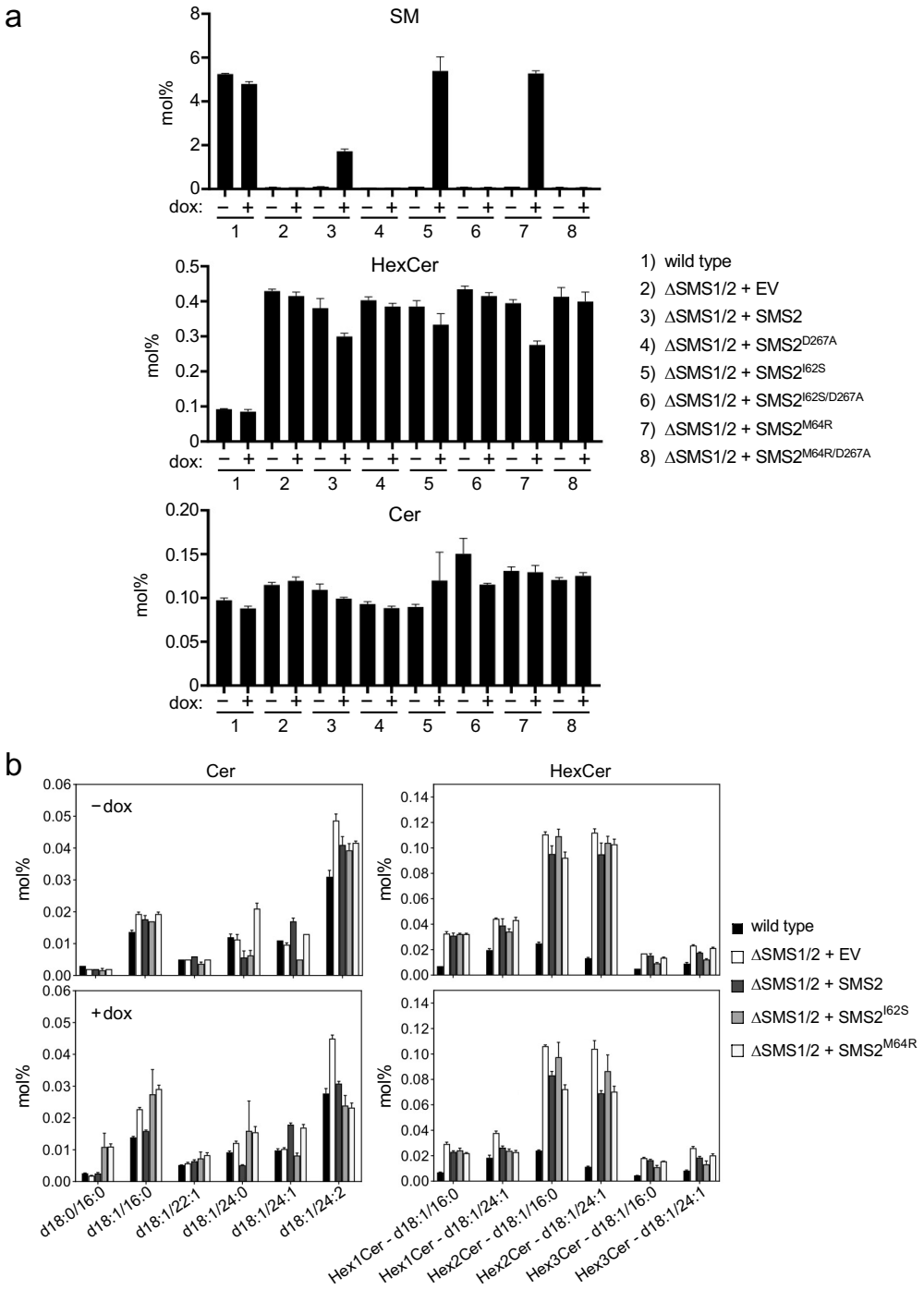

Fig. 12. Pathogenic SMS2 variants support bulk production of SM
(**a**) HeLa ΔSMS1/2 cells stably transduced with doxycycline-inducible Flag-tagged SMS2, SMS2^{I62S}, SMS2^{M64R} or their enzyme-dead isoforms (D276A) were grown for 16 h in the absence or presence of doxycycline and subjected to total lipid extraction. Cellular SM, glycosphingolipid (HexCer) and ceramide (Cer) levels were quantified by LC-MS/MS and expressed as mol% of total phospholipid analyzed. (**b**) Ceramide and HexCer species in total lipid extracts of cells treated as in (a) were quantified by LC-MS/MS and expressed as mol% of total phospholipid analyzed.

This was accompanied by a decrease in GSL levels. Doxycycline-induced expression of SMS2 only partially restored the SM pool, perhaps because SMS2, unlike its pathogenic isoforms, has no direct access to ER-derived ceramides. Moreover, ΔSMS1/2 cells expressing $SMS2^{I62S}$ or $SMS2^{M64R}$ contained 3- to 4-fold higher levels of dihydroceramide (Cer d18:0/16:0) and dihydroceramide-based SM (SM d18:0/16:0) than wildtype or SMS2-expressing ΔSMS1/2 cells (**Fig. 11d; Fig. 12**), suggesting that ER-resident $SMS2^{I62S}$ and $SMS2^{M64R}$ compete with ceramide desaturase DES1 for dihydroceramide substrate synthesized in the ER (**Fig. 11d**). All together, these data indicate that pathogenic SMS2 variants support bulk production of SM in the ER.

4.3. Lipidome analysis of ER and PM isolated from cells expressing pathogenic SMS2 variants

SM and cholesterol form a concentration gradient along the secretory pathway, with the highest levels in the plasma membrane (PM) and the lowest levels in the ER (van Meer, Voelker and Feigenson, 2008; Holthuis and Menon, 2014). The mechanism by which SM and cholesterol are moved up their concentration gradient into the PM is incompletely understood. However, preferential interactions of ER-derived cholesterol with SM synthesized in the *trans*-Golgi and their co-depletion from the highly curved COPI vesicles that mediate retrograde membrane trafficking could play a role (Brügger *et al.*, 2000; Slotte, 2013). I therefore asked whether pathogenic SMS2 variants that mediate bulk production of SM in the ER interfere with the ability of cells to generate a SM/cholesterol gradient along the secretory pathway. To address this, I set out to determine the lipid composition of ER and PM purified from wildtype or ΔSMS1/2 HeLa cells expressing SMS2 or its pathogenic isoform, $SMS2^{M64R}$. For purification of the ER, cells were lysed and a post-nuclear supernatant was incubated with an antibody against the ER-resident protein calnexin (**Fig. 13a**). This was followed by incubation with secondary antibody-conjugated paramagnetic microbeads. For PM isolation, the surface of intact cells was treated with a non-membrane permeant biotinylation reagent before cell lysis (**Fig. 14a**). Next, a post-nuclear supernatant was directly incubated with streptavidin-conjugated paramagnetic microbeads. The microbeads were then applied to columns packed with ferromagnetic spheres (μMACS columns) and the bound material was eluted after the columns were thoroughly washed.

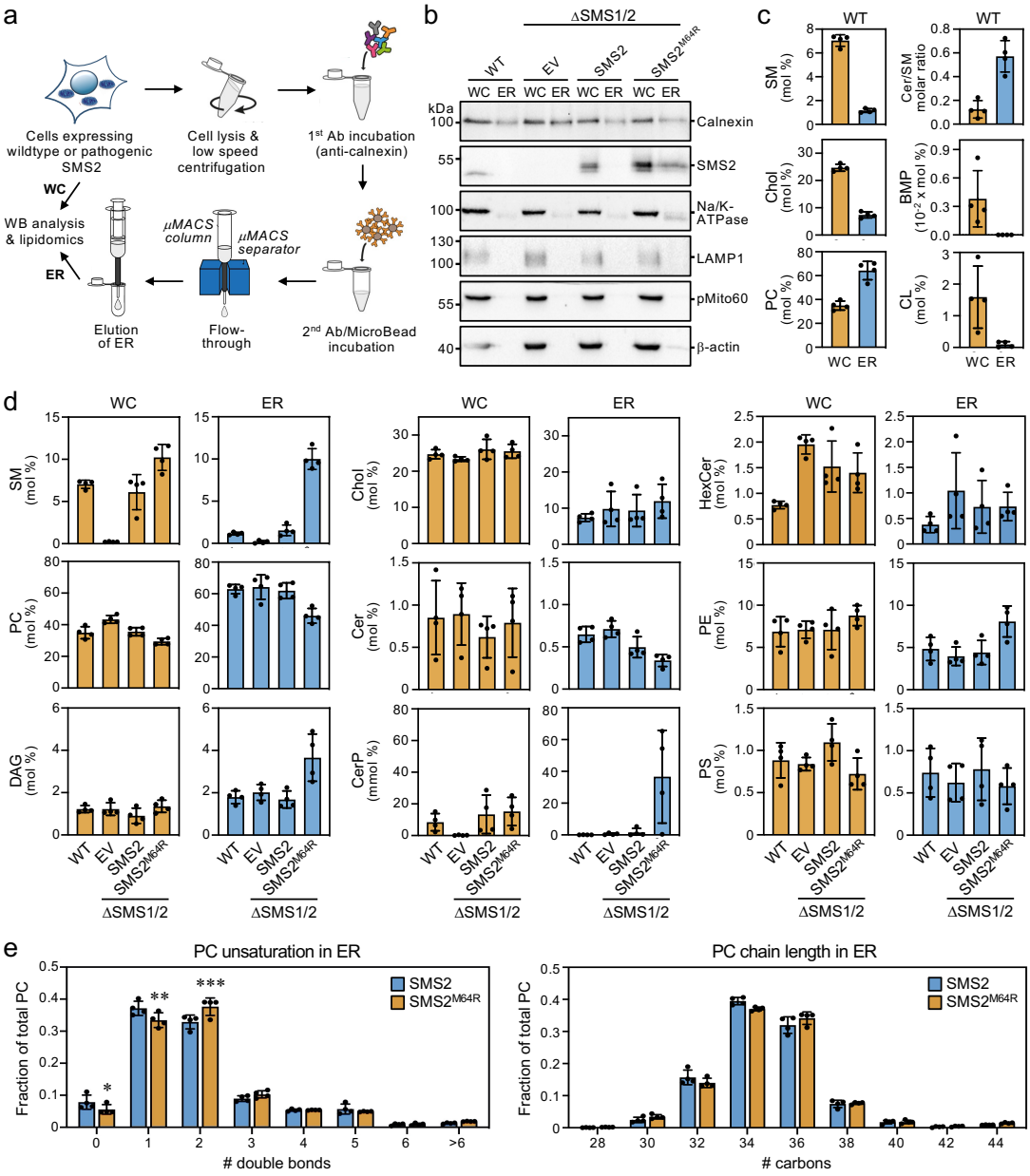

Fig. 13. Cells expressing pathogenic variant SMS2^{M64R} accumulate SM in the ER.
(**a**) Workflow for affinity purification of the ER from HeLa cells expressing wildtype or pathogenic SMS2 variants. (**b**) HeLa wildtype (WT) or ΔSMS1/2 cells stably transduced with empty vector (EV) or doxycycline-inducible SMS2 or SMS2^{M64R} were treated with doxycycline for 16 h, lysed and used to purify the ER as in (a). Whole cell lysates (WC) and purified ER were subjected to immunoblot analysis using antibodies against SMS2 and the organellar markers calnexin (ER), Na/K-ATPase (PM), LAMP1 (lysosomes), pMito60 (mitochondria) and β-actin (cytosol). (**c**) Lipid composition of whole cell lysates (WC) and ER purified from HeLa wildtype cells (WT) was determined by mass spectrometry-based shotgun lipidomics. Levels of the different lipid classes are expressed as mol% of total lipids identified. (**d**) Lipid composition of whole cell lysates (WC) and ER purified from cells treated as in (b) was determined by mass spectrometry-based shotgun lipidomics. Levels of the different lipid classes are expressed as mol% of total lipids identified. (**e**) Comparative analysis of PC unsaturation and chain length in ER purified from ΔSMS1/2 cells expressing SMS2 or SMS2^{M64R}. The graphs show total numbers of double bonds (left) or carbon atoms (right) in the two acyl chains. Data presented in panel (c) are included in panel (d). All data are average ±SD, $n = 4$. *$p < 0.05$, **$p < 0.01$, ***$p < 0.001$ by paired *t*-test.

I first assessed the purity of isolated ER and PM by immunoblot and lipidome analysis. As shown in **Fig. 13b**, ER eluates contained calnexin but were devoid of protein markers of the PM (Na/K-ATPase), lysosomes (LAMP1) and mitochondria (pMito60). As expected, ER eluates from cells expressing SMS2^{M64R} contained readily detectable levels of the protein. In contrast, no traces of SMS2 were found in ER eluates from cells expressing the wildtype protein. As there is no specific lipid marker for the ER, using a lipidomics approach to confirm that pull-down with anti-calnexin antibody indeed isolates the ER is not trivial. However, the ER is known to synthesize ceramides whereas SM is primarily produced in the *trans*-Golgi. In line with the immunoblot data, ER eluates from wildtype cells displayed a 5-fold higher ceramide/SM ratio than total cell lysates. Moreover, ER eluates were largely devoid of lipids that are normally concentrated in lysosomes (BMP), mitochondria (cardiolipin, CL) or PM (SM, cholesterol; **Fig. 13c**). Collectively, these results indicate that pull-down with anti-calnexin antibody enables a rapid isolation of the ER. Immunoblot analysis of the PM eluates revealed that they contain Na/K-ATPase but lack protein markers of the ER (calnexin), lysosomes (LAMP1), and mitochondria (pMito60; **Fig. 14b**). As expected, PM eluates from cells expressing wildtype SMS2 contained readily detectable amounts of the protein. On the other hand, PM eluates from ΔSMS1/2 cells expressing the pathogenic variant SMS2^{M64R} were devoid of this protein. Moreover, lipidome analysis of PM eluates revealed significantly elevated levels of lipids that are typically concentrated in the PM (i.e. SM, cholesterol, PS) and a 5-fold reduction in the ceramide/SM ratio relative to total cell lysates (**Fig. 14c**). Lipids primarily associated with lysosomes and mitochondria (BMP/PG, CL) were largely absent. From this I conclude that the pull-down approaches described above enable a meaningful analysis of ER and PM lipidomes from cells expressing wildtype or pathogenic SMS2.

4.4. Cells expressing pathogenic variant SMS2^{M64R} accumulate SM in the ER

Having established protocols for the rapid isolation of ER and PM, I next determined the lipid composition of these organelles in wildtype and ΔSMS1/2 cells expressing either SMS2 or SMS2^{M64R}. The ER of ΔSMS1/2 cells expressing SMS2 had a lipid composition similar to that of the ER of wildtype cells. In comparison, the ER of SMS2^{M64R}-expressing cells contained 5-fold higher SM levels, i.e. ~10 mol% instead of ~2 mol% of total phospholipid (**Fig. 13d**). This increase in ER-bound SM was accompanied by a two-fold rise in DAG levels and a significant drop in the amount of PC and ceramide, consistent with the presence of a catalytically active SM synthase in the ER. Interestingly, expression of SMS2^{M64R} also led to a significant, nearly two-fold increase in ER-associated PE levels. In contrast, ER levels of cholesterol and other bulk lipids were largely unaffected. However, I noticed that expression of SMS2^{M64R} enhanced unsaturation of bulk phospholipid in the ER, as indicated by a significant rise in di-unsaturated PC at the expense of saturated and mono-unsaturated PC species (**Fig. 13e**). PC chain length, on the other hand, was not affected. Unexpectedly, SMS2^{M64R} expression also caused a sharp increase in ER-bound ceramide-1-phosphate (Cer1P). Moreover, cellular Cer1P levels were essentially abolished in SM synthase-deficient cells, indicating that production of Cer1P is tightly coupled to SM biosynthesis.

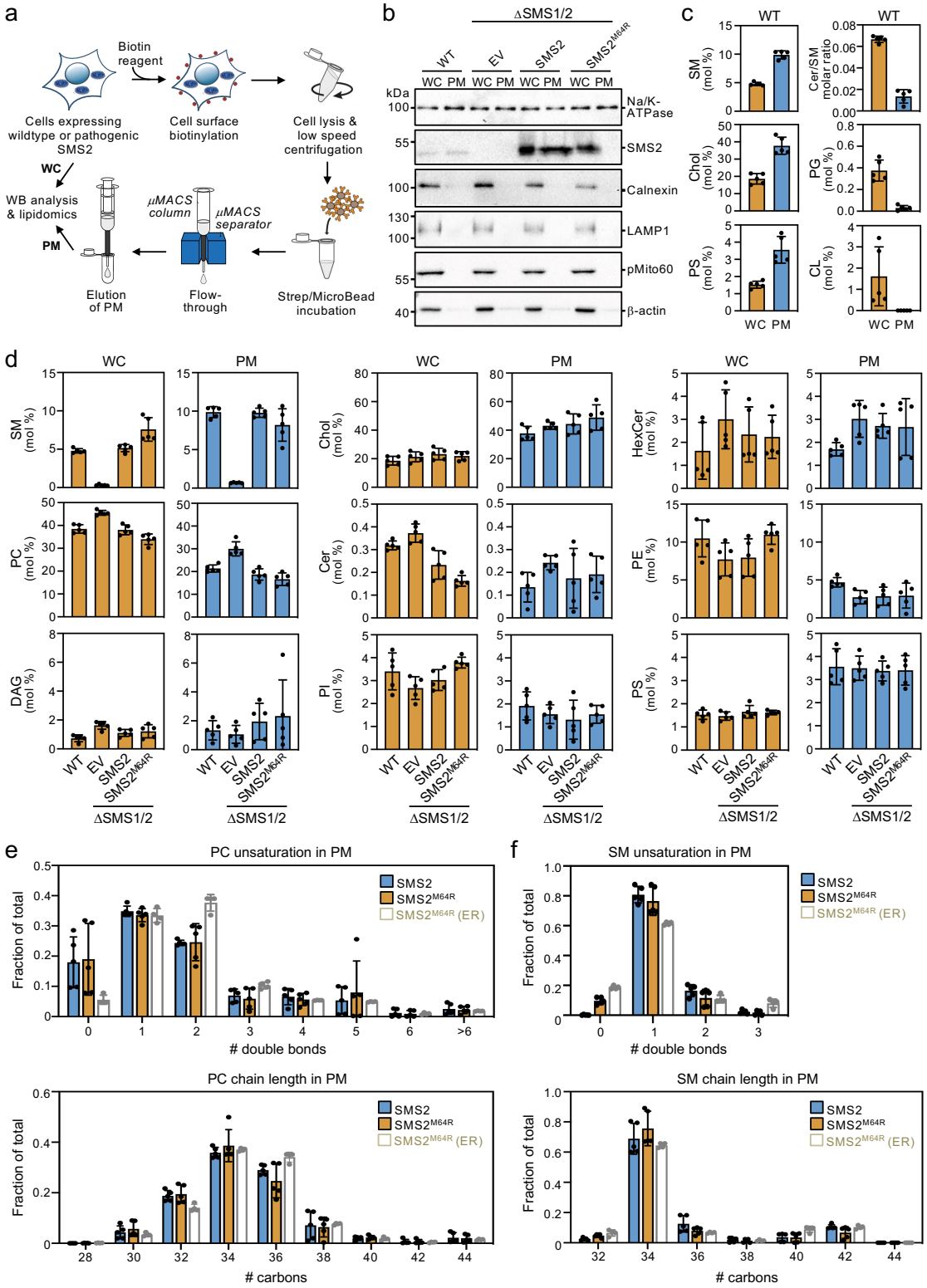

Fig. 14. Lipid composition of the PM of cells expressing wildtype or pathogenic SMS2 variant. (**a**) Workflow for affinity purification of the PM from HeLa cells expressing wildtype or pathogenic SMS2 variants. (**b**) HeLa wildtype (WT) or ΔSMS1/2 cells stably transduced with empty vector (EV) or doxycycline-inducible SMS2 or SMS2^{M64R} were treated with doxycycline for 16 h, lysed and used to purify the PM as in (a). Whole cell lysates (WC) and purified PM were subjected to immunoblot analysis using antibodies against SMS2 and the organellar markers Na/K-ATPase (PM), calnexin (ER), LAMP1 (lysosomes), pMito60 (mitochondria) and β-actin (cytosol). (**c**) Lipid composition of

whole cell lysates (WC) and PM purified from HeLa wildtype cells (WT) was determined by mass spectrometry-based shotgun lipidomics. Levels of the different lipid classes are expressed as mol% of total lipids identified. (**d**) Lipid composition of whole cell lysates (WC) and PM purified from cells treated as in (b) was determined by mass spectrometry-based shotgun lipidomics. Levels of the different lipid classes are expressed as mol% of total lipids identified. (**e**) Comparative analysis of PC unsaturation and chain length in PM purified from ΔSMS1/2 cells expressing SMS2 or $SMS2^{M64R}$. Values for PC unsaturation and chain length in ER purified from ΔSMS1/2 cells expressing $SMS2^{M64R}$ are included as reference. (**f**) Comparative analysis of SM unsaturation and chain length in PM purified from ΔSMS1/2 cells expressing SMS2 or $SMS2^{M64R}$. Values for SM unsaturation and chain length in ER purified from ΔSMS1/2 cells expressing $SMS2^{M64R}$ are included as reference. Data presented in panel (c) are included in panel (d). All data are average ±SD, *n* = 5 (except for ER, *n* = 4).

The PM of ΔSMS1/2 cells expressing SMS2 had a SM content similar to that of wildtype cells (~10 mol%). In comparison, the PM of ΔSMS1/2 cells expressing $SMS2^{M64R}$ had a slightly reduced SM content (~8 mol%) even though the total SM content of these cells was considerably higher (**Fig. 14d**). PM-associated levels of cholesterol and other bulk lipids did not show any obvious differences among the various cell lines, except for an increase in PC and lack of SM in SMS-deficient cells. The PM of all four cell lines contained significantly elevated levels of saturated PC species in comparison to the ER (**Fig. 14e**; data not shown). Moreover, the PM of ΔSMS1/2 cells expressing $SMS2^{M64R}$ contained significantly elevated levels of dihydroSM (**Fig. 14f**), consistent with the ER residency of this enzyme (**Fig. 11d**). Collectively, these data indicate that pathogenic SMS2 variants disrupt the SM gradient along the secretory pathway and cause profound changes in the lipid profile of the ER.

To confirm that cells expressing pathogenic SMS2 variants accumulate SM in the ER, I next used an engineered version of equinatoxin II (Eqt) as a non-toxic reporter of SM. To enable detection of SM inside the secretory pathway, the reporter was equipped with the *N*-terminal signal sequence of human growth hormone (hGH) and tagged at its *C*-terminus with oxGFP, yielding $EqtSM_{SS}$ (Deng et al., 2016). A luminal Eqt mutant defective in SM binding, $EqtSol_{SS}$, served as control. When expressed in human osteosarcoma U2OS cells, both $EqtSM_{SS}$ and $EqtSol_{SS}$ showed a reticular distribution that overlapped extensively with the ER marker protein VAP-A (**Fig. 15a**). However, upon co-expression with $SMS2^{M64R}$, $EqtSM_{SS}$ but not $EqtSol_{SS}$ displayed a distinct punctate distribution that coincided with the ER network. $EqtSM_{SS}$-containing puncta were not observed upon co-expression with the enzyme-dead variant $SMS2^{M64R/D276A}$, indicating that their formation strictly relies on SM production in the ER (**Fig. 15a**). To verify that the $EqtSM_{SS}$-containing puncta mark ER-resident pools of SM, I next subjected U2OS cells co-expressing $EqtSM_{SS}$ and $SMS2^{M64R}$ to hypotonic swelling as described previously (King *et al.*, 2020). After incubation for 5 min in hypotonic medium, the ER's fine tubular network transformed into numerous micrometer-sized vesicles. In $SMS2^{M64R}$-expressing cells, the membranes of these ER-derived vesicles were extensively labelled with $EqtSM_{SS}$ (**Fig. 15b**). In contrast, in hypotonic cells co-expressing $EqtSM_{SS}$ with $SMS2^{M64R/D276A}$ or $EqtSol_{SS}$ with $SMS2^{M64R}$, the reporter was found exclusively in the lumen of ER-derived vesicles, indicating that Eqt staining of the ER membrane critically relies on both catalytically active $SMS2^{M64R}$ and a SM-binding competent reporter. In agreement with the ER lipidome analyses, these results demonstrate that cells expressing $SMS2^{M64R}$ accumulate bulk amounts of SM in the ER. Moreover, my finding that hypotonic swelling of $SMS2^{M64R}$-expressing cells transforms the ER-associated

punctate distribution of EqtSM$_{SS}$ to a more uniform labeling of the ER bilayer suggests that alterations in membrane curvature and/or lipid packing affect the lateral organization of Eqt-SM assemblies.

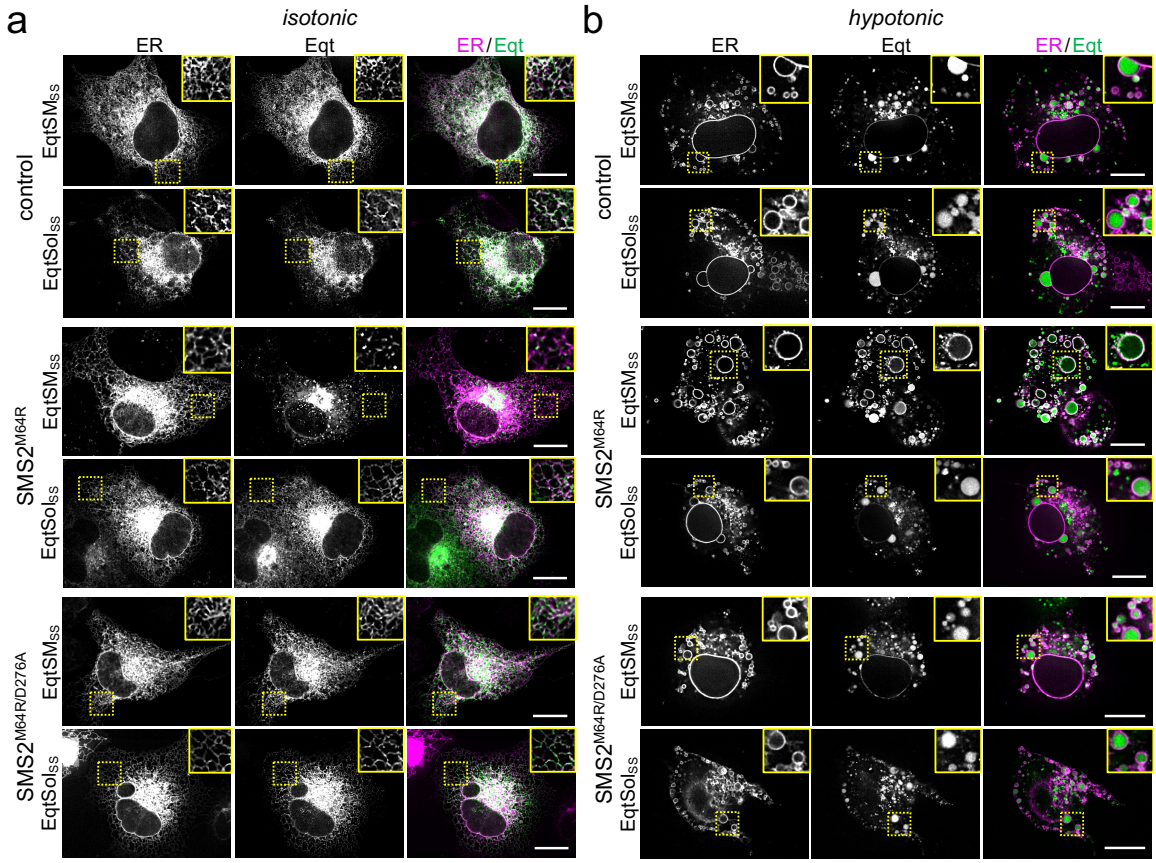

Fig. 15. Luminal SM reporter EqtSM$_{SS}$ enables visualization of an ER-resident SM pool in SMS2^{M64R}-expressing cells.
(**a**) Human osteosarcoma U2OS cells co-transfected with Flag-tagged SMS2^{M64R} or SMS2$^{M64R/D276A}$, mCherry-tagged VAP-A (ER, *magenta*) and luminal GFP-tagged SM reporter EqtSM$_{SS}$ or its SM binding-defective derivative, EqtSol$_{SS}$ (Eqt, *green*). After 16 h, cells were incubated in an isotonic medium (100% Opti-MEM) for 5 min and imaged by spinning disc confocal microscopy. (**b**) Cells treated as in (a) were incubated in hypotonic medium (1% Opti-MEM) for 5 min and then imaged by spinning disc confocal microscopy. Scale bars, 10 µm.

4.5. Pathogenic SMS2 variants affect SM asymmetry and lipid order on the cell surface

SM produced in the lumen of the *trans*-Golgi is thought to retain an asymmetric distribution across the bilayers of late secretory and endolysosomal organelles, with the bulk of SM residing in the luminal or exoplasmic leaflet. In line with this concept, EqtSM readily binds the surface of intact HeLa cells when added externally but fails to interact with any membrane-bound organelle when expressed as cytosolic protein (Deng *et al.*, 2016; **Figs. 16a** and **17a**). To enable detection of SM exposed to the cytosol of organellar membranes, I used GFP-tagged Eqt lacking the hGH signal sequence as cytosolic SM reporter (EqtSM$_{cyto}$) and the binding defective reporter (EqtSol$_{cyto}$) as control. To test the ability of

cytosolic SM reporter to faithfully report on cytosolic-facing SM, I treated wildtype and ΔSMS1/2 cells expressing GFP-tagged EqtSM$_{cyto}$ with a lysosome-damaging drug L-Leucyl-L-Leucine methyl ester (LLOME). EqtSM$_{cyto}$ but not the SM binding-defective EqtSol$_{cyto}$ was readily recruited to lysosomal membranes upon lysosomal damage in wildtype cells but not in SM deficient ΔSMS1/2 cells indicating that the mobilization of EqtSM$_{cyto}$ depends on cytosolic-facing SM (**Fig.16 a and b**).

To perform its central task in membrane biogenesis, the ER harbors constitutively active scramblases that enable a rapid equilibration of newly synthesized phospholipids across its bilayer (Pomorski and Menon, 2016). Therefore, I next asked whether SM produced by pathogenic SMS2 variants in the ER lumen has access to the cytosolic leaflet. As expected, EqtSM$_{cyto}$ in wildtype or ΔSMS1/2 cells expressing SMS2 displayed a diffuse cytosolic distribution. In contrast, expression of the pathogenic variant SMS2^{I62S} or SMS2^{M64R} in each case led EqtSM$_{cyto}$ to accumulate in numerous discrete puncta that were spread throughout the cytosol (**Fig. 17a**; **Fig. S2**). Importantly, formation of Eqt-positive puncta required expression of a catalytically active pathogenic variant and was not observed when using SM binding-defective cytosolic reporter EqtSol$_{cyto}$ (**Fig. S3**). These results indicate that pathogenic SMS2 variants break transbilayer SM asymmetry, presumably because ER-resident scramblases enable SM produced by these variants to readily equilibrate across the ER bilayer.

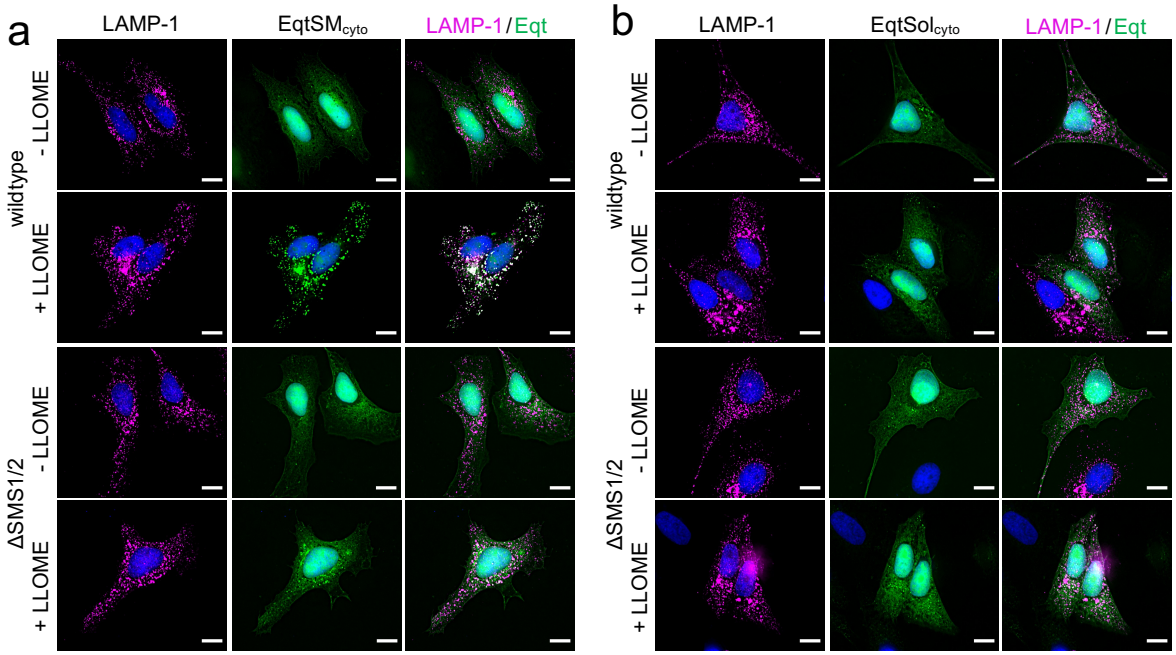

Fig. 16. EqtSM$_{cyto}$ reports SM exposed on damaged lysosomes.
(**a**) HeLa wildtype (WT) or ΔSMS1/2 cells were transfected with cytosolic GFP-tagged SM reporter EqtSMcyto (*green*). Cells were treated with 1 mM LLOME for 10 minutes, fixed, immunostained with α-LAMP-1 antibody (*magenta*), counterstained with DAPI (*blue*) and imaged by DeltaVision microscopy. Scale bars, 10 μm. (**b**) Cells as in (a) were transfected with cytosolic GFP-tagged SM binding-defective EqtSolcyto (*green*). Next, cells were treated with 1 mM LLOME for 10 minutes, fixed, immunostained with α-LAMP-1 antibody (*magenta*), counterstained with DAPI (*blue*) and imaged by DeltaVision microscopy. Scale bars, 10 μm.

Remarkably, the EqtSM$_{cyto}$-positive puncta formed in SMS2^{I62S} or SMS2^{M64R}-expressing cells were largely segregated from a wide array of organellar markers, including VAP-A (ER), Sec16L (ER exit sites), ERGIC-53 (*cis*-Golgi), GM130 (*medial*-Golgi), TGN64 (*trans*-Golgi), EEA1 (early endosomes), LAMP1 (lysosomes) and LD540 (lipid droplets; **Fig. 17b**).

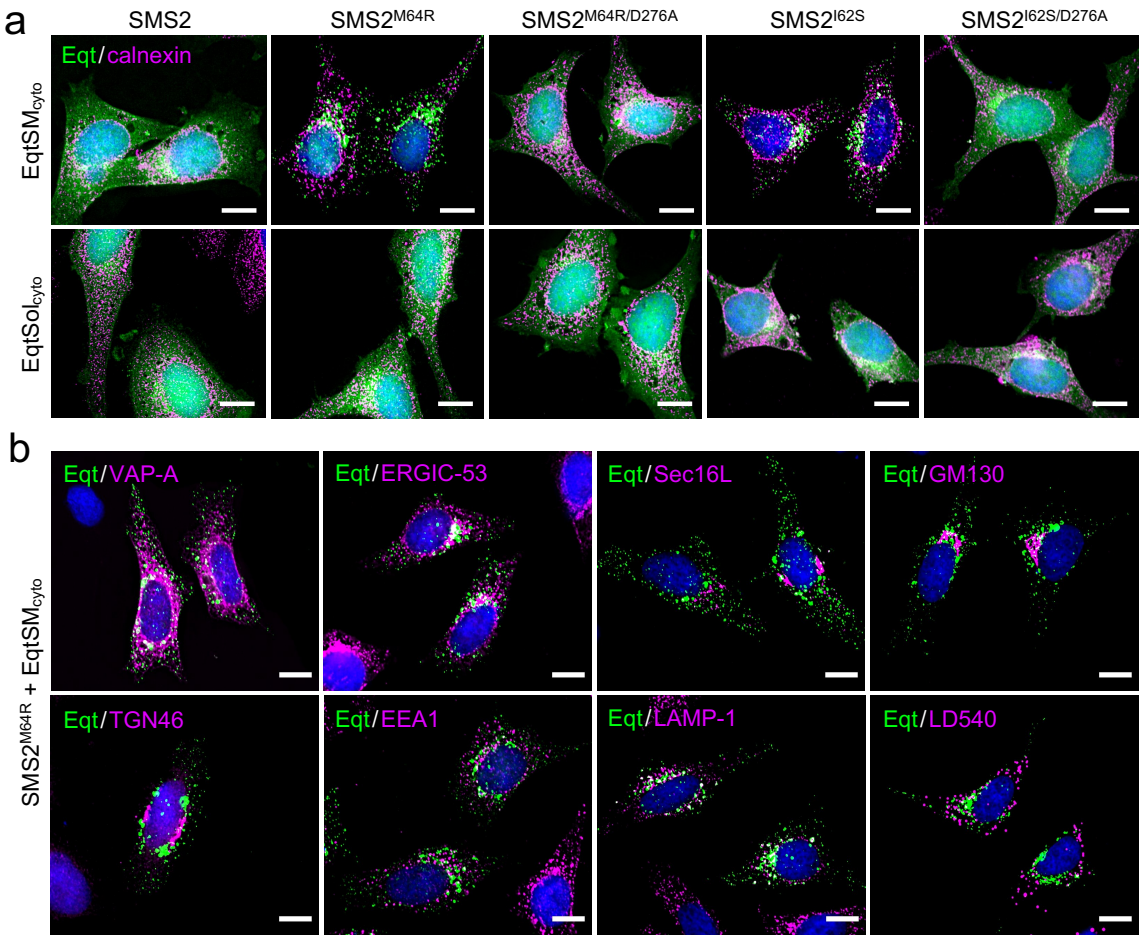

Fig. 17. Pathogenic SMS2 variants disrupt transbilayer SM asymmetry.
(**a**) HeLa ΔSMS1/2 cells stably transduced with doxycycline-inducible Flag-tagged SMS2, SMS2^{M64R}, SMS2^{I62S} or their enzyme-dead isoforms (D276A) were transfected with cytosolic GFP-tagged SM reporter EqtSM$_{cyto}$ or its SM binding-defective derivative, EqtSol$_{cyto}$ (Eqt, *green*). Next, cells were treated with doxycycline for 16 h, fixed, immunostained with α-calnexin antibodies (*magenta*), counterstained with DAPI (*blue*) and then imaged by DeltaVision microscopy. (**b**) HeLa ΔSMS1/2 cells stably transduced with doxycycline-inducible Flag-tagged SMS2^{M64R} were transfected with EqtSM$_{cyto}$ (*green*) and treated with doxycycline for 16 h. Next, cells were fixed, immunostained with antibodies against various organellar markers (*magenta*), counterstained with DAPI (*blue*) and imaged by DeltaVision microscopy. Organellar markers include Sec16L (ER exit sites), ERGIC-53 (*cis*-Golgi), GM130 (*medial*-Golgi), TGN46 (*trans*-Golgi), EEA1 (early endosomes) and LAMP1 (lysosomes). The ER was marked by co-transfection with mCherry-tagged VAP-A while lipid droplets were stained using the lipophilic dye LD540. Scale bars, 10 µm.

When cells expressing SMS2^{I62S} or SMS2^{M64R} were subjected to hypotonic swelling, EqtSM$_{cyto}$-positive puncta remained largely segregated from ER-derived microvesicles (data not shown). I cannot exclude that formation of Eqt-SM assemblies on the cytosolic surface of the ER drives a process whereby SM-rich vesicles are pinched off from the organelle, even though my efforts to capture such vesicles by correlative light-electron

microscopy were unsuccessful. Therefore, the precise nature of the $EqtSM_{cyto}$-positive puncta observed in cells expressing pathogenic variants remains to be established. The foregoing implies that in cells expressing pathogenic SMS2 variants, only part of the SM arriving at the PM would reside in the exoplasmic leaflet and that a considerable portion would be mislocalized to the cytosolic leaflet. To challenge the idea that only a portion of SM arrives at the exoplasmic leaflet of the PM, I next stained the surface of intact wildtype or ΔSMS1/2 HeLa cells expressing SMS2 or $SMS2^{M64R}$ with recombinant EqtSM. Cell surface labeling was visualized by fluorescence microscopy and quantitatively assessed by flow cytometry. As shown in **Fig. 18a**, wildtype cells could be readily stained with the SM reporter whereas ΔSMS1/2 cells were devoid of EqtSM staining. Expression of SMS2 but not enzyme dead $SMS2^{D276A}$ restored EqtSM staining of ΔSMS1/2 cells to a level approaching that in wildtype cells. In contrast, expression of $SMS2^{M64R}$ restored cell surface staining to only a minor degree (**Fig. 18a, b**) even though the PM-associated SM pool in these cells was very close to that in wildtype or SMS2-expressing ΔSMS1/2 cells (**Fig. 14d**). These data indicate that pathogenic SMS2 variants severely undermine the establishment of SM asymmetry at the PM.

Owing to its saturated nature and affinity for sterols, SM contributes significantly to the lipid order in cellular membranes. As pathogenic SMS2 variants enhance SM levels in the ER and affect the ability of cells to accumulate SM on their surface, I next used two Nile Red (NR)-based solvatochromic probes, NR12A and $NRER_{Cl}$, to selectively measure lipid order at these locations in cells expressing SMS2 or $SMS2^{M64R}$. The emission spectra of these probes are blue-shifted in tightly packed lipid bilayers, which is due to a reduced polarity in the nano-environment of the NR fluorophore. The relative extent of these spectral shifts can be quantified by ratiometric imaging. The presence of a charged ionic anchor that blocks passive flip-flop across membrane bilayers in NR12A makes this probe ideally suited to selectively quantify lipid order in the outer PM leaflet of living cells when added to the extracellular medium (Danylchuck *et al.*, 2019). On the other hand, the presence of a propyl chloride group in $NRER_{Cl}$ targets this probe to the ER (Danylchuck *et al.*, 2021). As expected, the lipid order reported by NR12A in the outer PM leaflet of ΔSMS1/2 cells was drastically reduced in comparison to that in wildtype cells (**Fig. 18c, d**). Expression of SMS2 partially restored lipid order. In contrast, expression of $SMS2^{M64R}$ failed to restore lipid order to any appreciable degree. Conversely, the lipid order reported by $NRER_{Cl}$ in the ER of cells expressing $SMS2^{M64R}$ was significantly increased in comparison to that in the ER of SMS2-expressing cells (**Fig. 18e, f**). Hence, the disruption of subcellular SM distributions caused by pathogenic SMS2 variants is accompanied by major imbalances in lipid order along the secretory pathway.

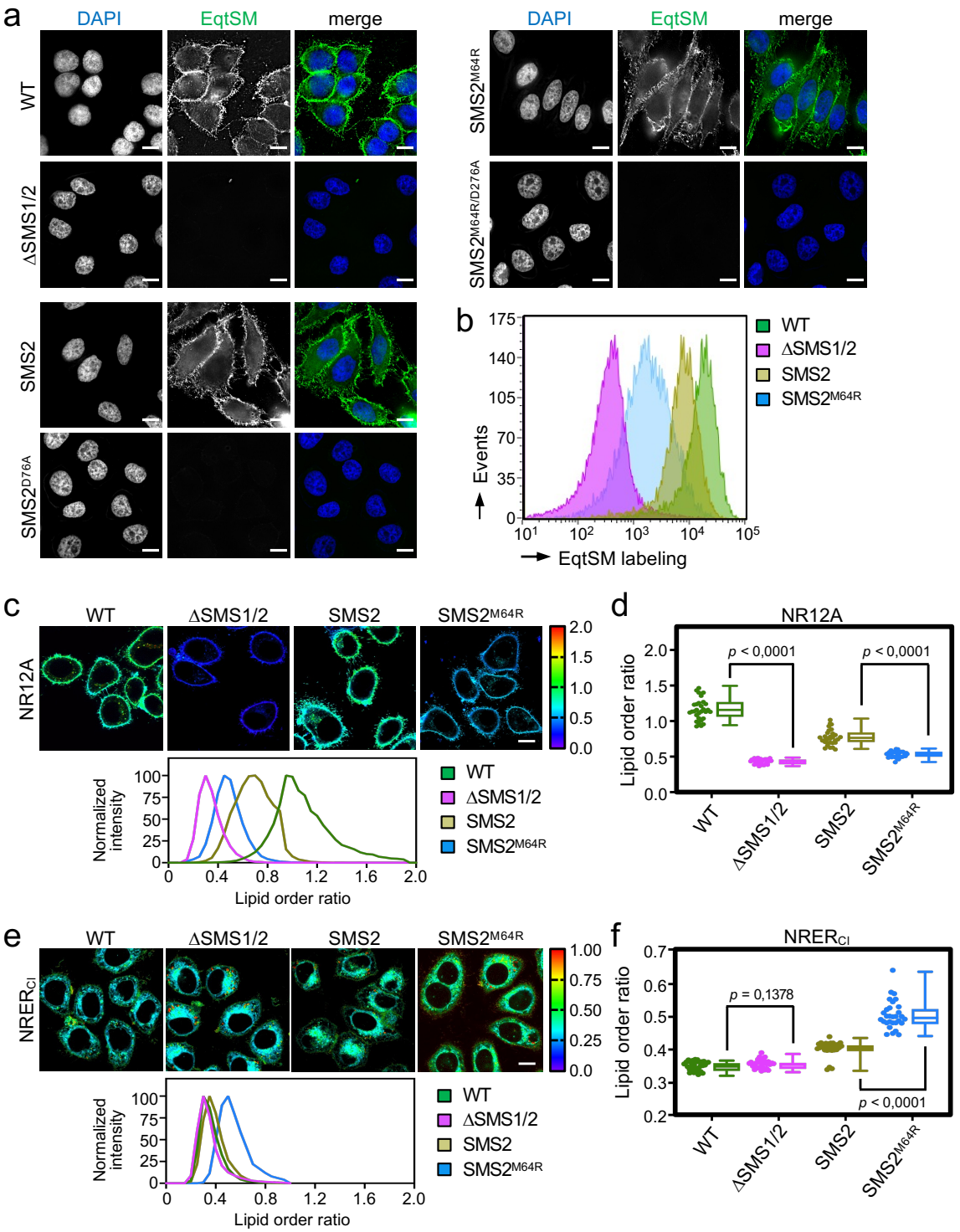

Fig. 18. Cells expressing pathogenic SMS2 variants fail to concentrate SM on their surface. (**a**) HeLa wildtype (WT) or ΔSMS1/2 cells stably transduced with SMS2, SMS2^{M64R} or their enzyme-dead isoforms (D276A) were treated with doxycycline for 16 h, stained with externally added recombinant FLAG-tagged EqtSM (*green*), fixed, immunostained against α-FLAG, counterstained with DAPI (*blue*) and imaged by DeltaVision microscopy. (**b**) Cells treated as in (a) were analyzed by flow cytometry to quantitatively assess EqtSM labeling of their surface. (**c**) HeLa wildtype (WT) or ΔSMS1/2 cells stably transduced with SMS2 or SMS2^{M64R} were treated with doxycycline for 16 h, stained with 0.2 μM NR12A for 10 min and analyzed by ratiometric fluorescence microscopy to probe the lipid order in the outer PM leaflet. Warmer colors reflect a higher lipid order. (**d**) Quantitative

assessment of changes in the lipid order in the outer PM leaflet of cells treated as in (c). Thirty cells were analyzed per condition, *n* = 2. (**e**) HeLa wildtype (WT) or ΔSMS1/2 cells stably transduced with SMS2 or SMS2^{M64R} were treated with doxycycline for 16 h, stained with 0.2 μM $NRER_{Cl}$ for 30 min and analyzed by ratiometric fluorescence microscopy to probe the lipid order in the ER membrane. Warmer colors reflect a higher lipid order. (**f**) Quantitative assessment of changes in the lipid order in the ER membrane of cells treated as in (e). Thirty cells were analyzed per condition, *n* = 2. Statistical analysis was by unpaired *t*-test. Scale bars, 10 μm. Ratiometric analyses were performed together with Bingshati Sarkar.

4.6. Pathogenic SMS2 variants perturb subcellular sterol pools

As the preferred cholesterol interaction partner, SM has been widely implicated in the subcellular organization of cholesterol (Slotte, 2013; Das *et al*., 2014). Therefore, it was somewhat surprising that the marked accumulation of SM in the ER of SMS2^{M64R}-expressing cells had no detectable impact on ER-bound cholesterol levels (**Fig. 13d**) or the cellular pool of cholesteryl-esters (data not shown). To further examine whether pathogenic SMS2 variants influence the cholesterol distribution in cells, I next used a mCherry-tagged D4H sterol reporter derived from the perfringolysin O *θ*-toxin of *Clostridium perfringens*. This reporter specifically recognizes cholesterol when present at >20 mol% in membranes and mainly decorates the inner leaflet of the PM at steady state when expressed as cytosolic protein. Part of the reason for the high detection threshold is that the reporter detects free cholesterol in the membrane but not cholesterol in complex with SM (Das *et al.*, 2014). Moreover, a previous study showed that plasmalemmal PS is essential for retaining D4H-accessible cholesterol in the inner PM leaflet (Maekawa and Fairn, 2015). Accordingly, I found that cytosolic D4H-mCherry primarily stained the PM in wildtype HeLa cells. In contrast, the probe displayed a more diffuse cytosolic distribution in ΔSMS1/2 cells (**Fig. S4a**). Expression of SMS2 in ΔSMS1/2 cells restored PM staining, indicating that PM-associated SM is critical for controlling the reporter-accessible cholesterol pool in the PM (**Fig. 19a**). Strikingly, in ΔSMS1/2 cells expressing pathogenic variant SMS2^{M64R} or SMS2^{I62S}, D4H-mCherry primarily accumulated in intracellular vesicles that co-localized extensively with dextran-positive endolysosomal compartments (**Fig. 19b**). While it remains to be established how this shift in D4H-mCherry distribution is accomplished, it is conceivable that an expanding pool of SM in the inner PM leaflet of cells expressing pathogenic SMS2 variants renders a coexisting cholesterol pool inaccessible to the reporter.

Since cholesterol has a stronger affinity for SM than for PS or other phospholipid classes, altering the SM concentration affects the behavior of cholesterol in artificial and biological membranes (Slotte, 2013). For instance, when exposed to the cholesterol-absorbing agent methyl-b-cyclodextrin (mβCD), SM-depleted cells readily lose PM-associated cholesterol and consequently their viability more rapidly than wildtype cells (Fukasawa *et al*., 2000; Hanada *et al*., 2003). As additional approach to determine the impact of pathogenic SMS2 variants on cholesterol organization in the PM, I next probed ΔSMS1/2 cells expressing wildtype or pathogenic SMS2 variants for their sensitivity toward mβCD. As expected, ΔSMS1/2 cells displayed a substantially reduced tolerance for mβCD in comparison to wildtype cells (**Fig. 19c**). Expression of SMS2 restored mβCD tolerance of ΔSMS1/2 cells to that of wildtype cells. In contrast, expression of SMS2^{M64R} or SMS2^{I62S} in each case failed to render ΔSMS1/2 cells resistant toward mβCD. These results provide complementary

support for the notion that pathogenic SMS2 variants significantly affect cholesterol organization in the PM.

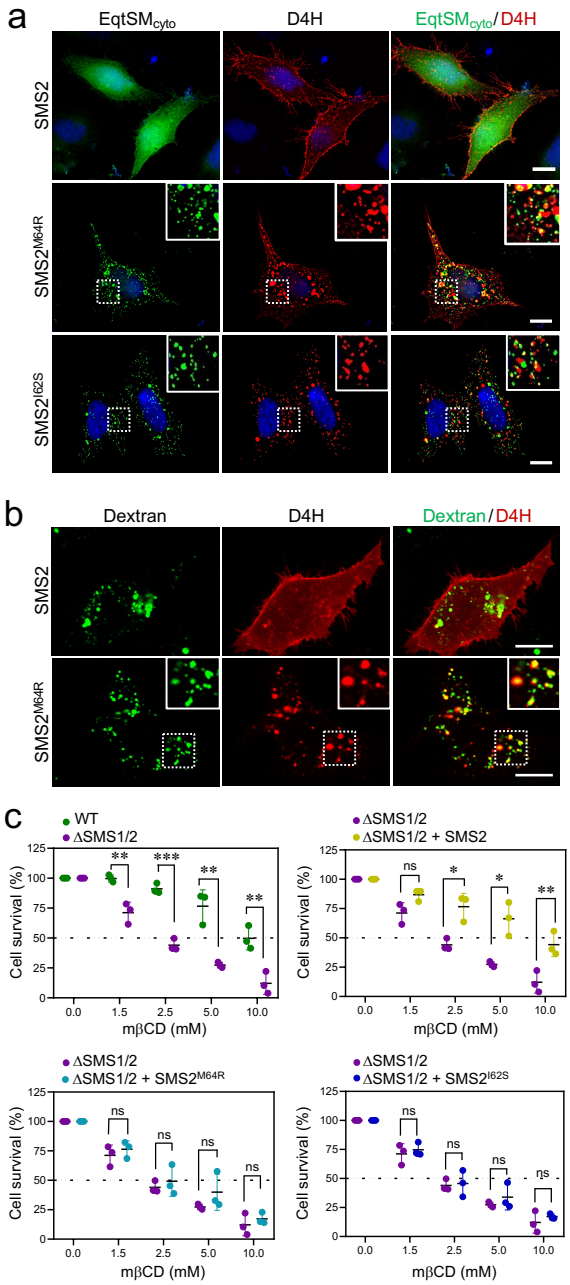

Fig. 19. Pathogenic SMS2 variants perturb subcellular cholesterol pools.
(**a**) HeLa ΔSMS1/2 cells stably transduced with FLAG-tagged SMS2, SMS2^{M64R} or SMS2^{I62S} were co-transfected with GFP-tagged EqtSM$_{cyto}$ (*green*) and mCherry-tagged cytosolic sterol reporter D4H (*red*). Next, cells were treated with doxycycline for 16 h, fixed, counterstained with DAPI (*blue*), and visualized by DeltaVision microscopy. (**b**) HeLa ΔSMS1/2 cells stably transduced with FLAG-tagged SMS2 or SMS2^{M64R} were transfected with mCherry-tagged D4H (*red*), labeled with fluorescein-conjugated dextran (*green*) in the presence of doxycycline for 16 h and then imaged by spinning disc confocal microscopy. (**c**) HeLa wildtype (WT) or ΔSMS1/2 cells stably transduced with SMS2, SMS2^{M64R} or SMS2^{I62S} were treated with doxycycline for 16 h. Next, cells were exposed to the indicated concentration of methyl-β-cyclodextrin (mβCD) for 1 h and cell viability was assessed using Prestoblue reagent. All data shown are average of 4 technical replicates from n = 3 biological replicates. *p < 0.05, **p < 0.01, ***p < 0.001 by paired t test. Scale bars, 10 μm.

4.7. Patient-derived fibroblasts display aberrant SM and sterol distribution

I next asked whether the aberrant subcellular SM and cholesterol distributions observed upon heterologous expression of pathogenic SMS2 variants also occur in cells of patients that carry the corresponding heterozygous pathogenic mutations in their genome. To address this, skin fibroblasts derived from patients with the missense variant p.I62S or p.M64R and healthy controls were co-transfected with the luminal SM reporter $EqtSM_{SS}$ and mCherry-tagged VAP-A as ER marker. Next, the fibroblasts were subjected to hypotonic swelling as described above and imaged by fluorescence microscopy. Strikingly, in patient-derived fibroblasts, the membranes of ER-derived vesicles were extensively labelled with $EqtSM_{SS}$ (**Fig. 20a**). In contrast, in fibroblasts of healthy controls, $EqtSM_{SS}$ was found exclusively in the lumen of ER-derived vesicles. Moreover, labeling of the ER membrane in patient-derived fibroblasts was abolished when using SM binding-defective $EqtSol_{SS}$ as reporter. This indicates that the ER in patient-derived fibroblasts contains substantially elevated SM levels, hence analogous to the ER in HeLa cells upon heterologous expression of pathogenic SMS2 variants (**Figs. 13, 15**). In addition, I found that the cytosolic SM reporter $EqtSM_{cyto}$ accumulated in numerous puncta when expressed in patient-derived fibroblasts whereas its expression in fibroblasts from healthy controls resulted in a diffuse cytosolic distribution (**Fig. 20b**). Formation of Eqt-positive puncta in the patient-derived fibroblasts did not occur when using the SM binding-defective reporter, $EqtSol_{cyto}$. Additionally, I probed the lipid order of the ER and PM of fibroblasts using organellar targeted Nile red dyes. The lipid order in the PM outer leaflet of p.I62S and p.M64R cells as measured by NR12A was markedly reduced (**Fig. 20c**) while the lipid order in the ER as measured by $NRER_{Cl}$ was significantly increased compared to the ER of fibroblasts from healthy patients (**Fig. 20d**). Thus, besides accumulating SM in the ER, patient-derived fibroblasts display a disrupted SM asymmetry and major imbalances in lipid order along the secretory pathway. Moreover, the aberrant SM distribution in patient-derived fibroblasts was accompanied by an altered cholesterol organization. While the cytosolic cholesterol reporter D4H-mCherry primarily stained the PM of fibroblasts from healthy controls, in patient-derived fibroblasts a substantial portion of the reporter was shifted to intracellular vesicles (**Fig. 21**). From this I conclude that pathogenic SMS2 variants p.I62S and p.M64R, which underly a spectrum of severe skeletal conditions, significantly perturb the distribution of SM and cholesterol, and lipid order along the secretory pathway.

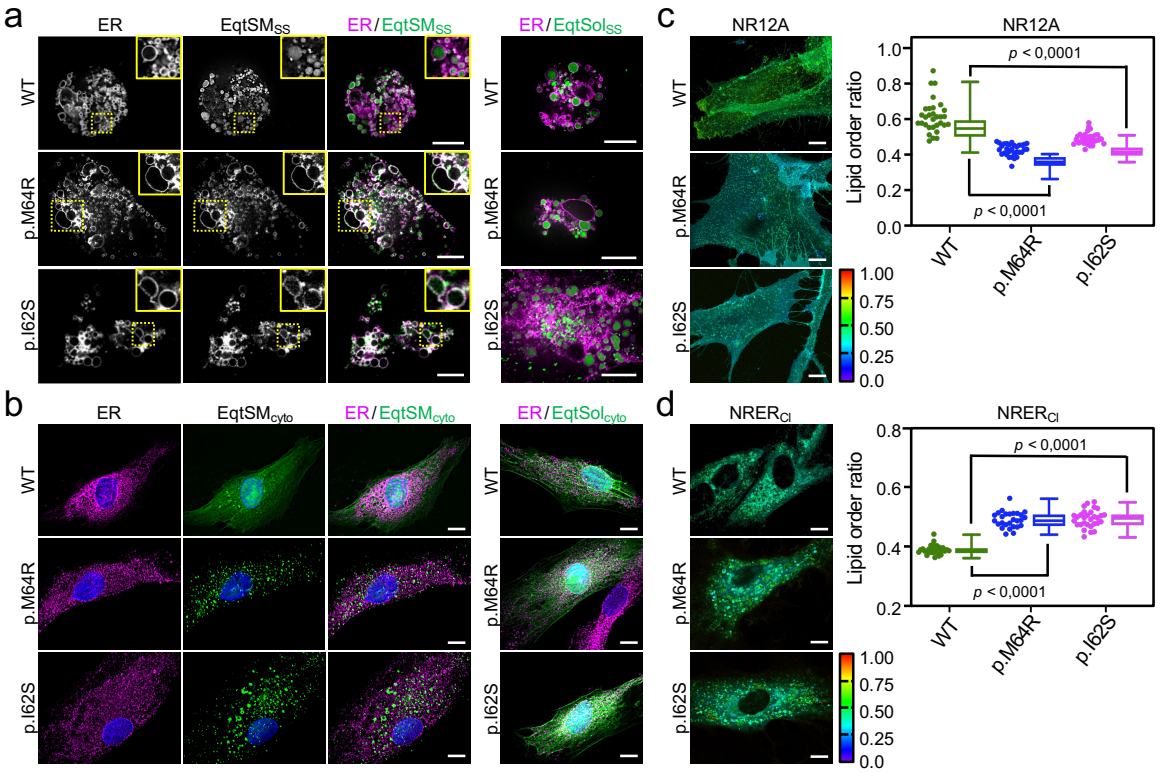

Fig. 20. Patient-derived fibroblasts disrupt SM asymmetry and lipid order.
(**a**) Control (WT) or patient-derived human skin fibroblasts carrying heterozygous missense variants c.185T>G (p.I62S) or c.191T>G (p.M64R) in *SGMS2* were co-transfected with mCherry-tagged VAP-A (ER, *magenta*) and GFP-tagged EqtSM$_{SS}$ (*green*). Co-transfections with GFP-tagged EqtSol$_{SS}$ served as control. After 16 h, cells were incubated in hypotonic medium (1% Opti-MEM) for 5 min and imaged by spinning disc confocal microscopy. (**b**) Fibroblasts as in (a) were transfected with GFP-tagged EqtSM$_{cyto}$. After 16 h, cells were fixed, immunostained with α-calnexin antibody (ER, *magenta*), counterstained with DAPI (*blue*) and imaged by DeltaVision microscopy. (**c**) Fibroblasts as in (b) were stained with 0.2 μM NR12A for 10 min and analyzed by ratiometric fluorescence microscopy to probe the lipid order in the outer PM leaflet. Warmer colors reflect a higher lipid order. Quantitative assessment of changes in the lipid order in the outer PM leaflet of cells. Thirty cells were analyzed per condition, $n = 2$. (**d**) Fibroblasts as in (b) were stained with 0.2 μM NRER$_{Cl}$ for 30 min and analyzed by ratiometric fluorescence microscopy to probe the lipid order in the ER membrane. Warmer colors reflect a higher lipid order. Quantitative assessment of changes in the lipid order in the outer PM leaflet of cells. Thirty cells were analyzed per condition, $n = 2$. Statistical analysis was by unpaired *t*-test. Scale bars, 10 μm. Ratiometric analyses were performed together with Bingshati Sarkar.

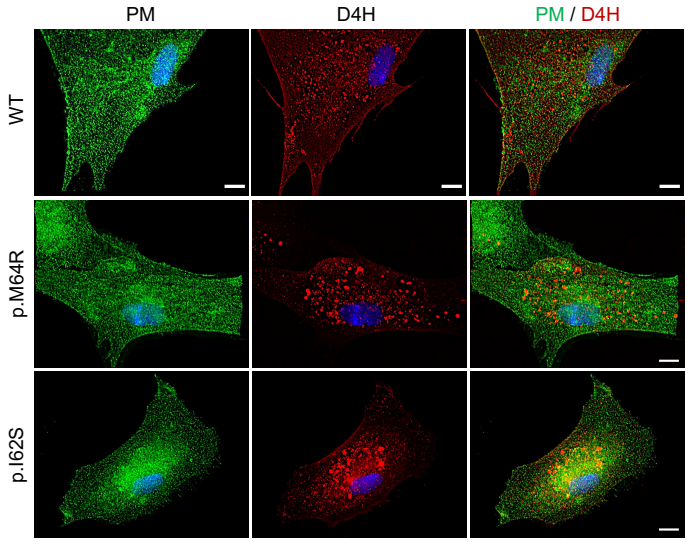

Fig. 21. Patient-derived fibroblasts display aberrant sterol distribution.
Control (WT) or patient-derived human skin fibroblasts carrying heterozygous missense variants c.185T>G (p.I62S) or c.191T>G (p.M64R) in *SGMS2* were transfected with mCherry-tagged D4H (*red*), fixed, immunostained with α-Na/K-ATPase antibody (PM, *green*) and imaged by Deltavision microscopy. Scale bars, 10 µm.

4.8. Pathogenic variant SMS2^{R50X} yields an active enzyme

Previous work reported that the nonsense SMS2 variant p.R50X is more common and is accompanied by milder phenotype in patients (Pekinnen *et al.,* 2019; Makitie *et al.,* 2021; Basalom *et al.,* 2021). It was predicted that the mutant encodes a truncated enzyme lacking the entire transmembrane helices of the enzyme. I reasoned that an alternative start methionine (Met64) may be utilized in the synthesis of the enzyme. To directly test this, I stably transduced HeLa SMS1/2 double knockout (ΔSMS1/2) cells with doxycycline-inducible lentiviral expression constructs encoding N-terminal HA-tagged SMS2, SMS2^{R50X}, or their enzyme dead isoforms SMS2^{D276A}, SMS2$^{R50X/D276A}$ respectively and mutations where Met64 was replaced with alanine- SMS2^{M64A} and a double mutant, SMS2$^{R50X/M64A}$. Next, cells were grown in the presence or absence of doxycycline for 16 h. Immunoblot analysis confirmed the doxycycline-inducible expression of recombinant protein and showed that SMS2^{R50X} produces an isoform of the protein that has a smaller size than wildtype SMS2 (**Fig. 22a**). SMS2^{R50X} was not detectable by an antibody that recognizes the first 80 amino acids of SMS2. No protein expression was observed in the double mutant SMS2$^{R50X/M64A}$ where Met64 was replaced with alanine. (**Fig. 22a**)**.** This validated that SMS2^{R50X} indeed utilizes Met64 as an alternative start codon to produce a truncated version of the protein lacking the first 63 amino acids. To examine the biosynthetic capacity of SMS2^{R50X} mutant, control and doxycycline-treated cells were metabolically labelled with a clickable sphingosine analogue for 16 h, subjected to total lipid extraction, click reacted with the fluorogenic dye 3-azido-7-hydroxycoumarin and analyzed by TLC. This revealed that doxycycline-induced expression of SMS2^{R50X}, not its enzyme-dead isoform SMS2$^{R50X/D276A}$ restored SM biosynthesis in ΔSMS1/2 (**Fig. 22b**). Quantitative mass spectrometry analyses of SMS2^{R50X}-expressing cells confirmed restoration of SM pool in ΔSMS1/2 cells albeit to lower levels than wildtype (**Fig. 22c; Fig. 23a**). This was accompanied by a decrease in

GSL levels to levels approaching WT levels. Altogether, this data indicates that SMS2^{R50X} encodes a truncated but catalytically active enzyme.

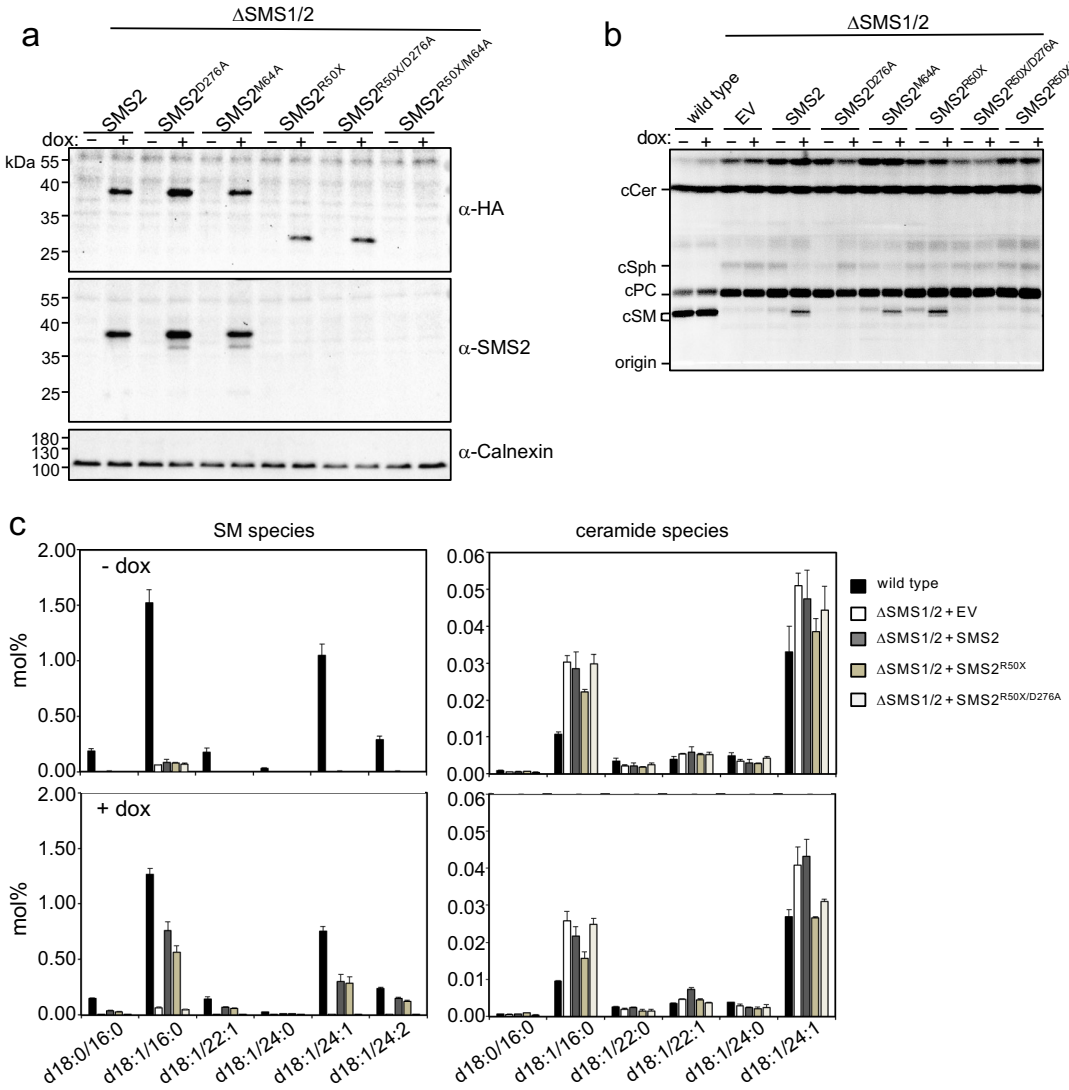

Fig. 22. Pathogenic SMS2^{R50X} yields a catalytically active enzyme.
(**a**) HeLa ΔSMS1/2 cells stably transduced with doxycycline-inducible N-terminal HA-tagged SMS2, SMS2^{R50X}, or their enzyme dead isoforms SMS2^{D276A}, SMS2$^{R50X/D276A}$ respectively and mutations where Met64 was replaced with Ala -SMS2^{M64A} and the double mutant, SMS2$^{R50X/M64A}$ were grown for 16 h in the absence or presence of doxycycline and then subjected to immunoblot analysis using α-HA, α-SMS2 and α-Calnexin antibodies. (**b**) Cells treated as in (a) were metabolically labelled with a clickable sphingosine analogue for 16 h, subjected to total lipid extraction, click reacted with the fluorogenic dye 3-azido-7-hydroxycoumarin and analyzed by TLC. Wildtype and ΔSMS1/2 served as controls. (**c**) HeLa SMS1/2 double KO (ΔSMS1/2) cells stably transduced with doxycycline-inducible N-terminal HA-tagged SMS2, SMS2^{R50X}, or the enzyme dead isoform, SMS2$^{R50X/D276A}$ were grown for 16 h in the absence or presence of doxycycline. SM and ceramide species in total lipid extracts of cells treated as in (a) were quantified by LC-MS/MS and expressed as mol% of total phospholipid analyzed.

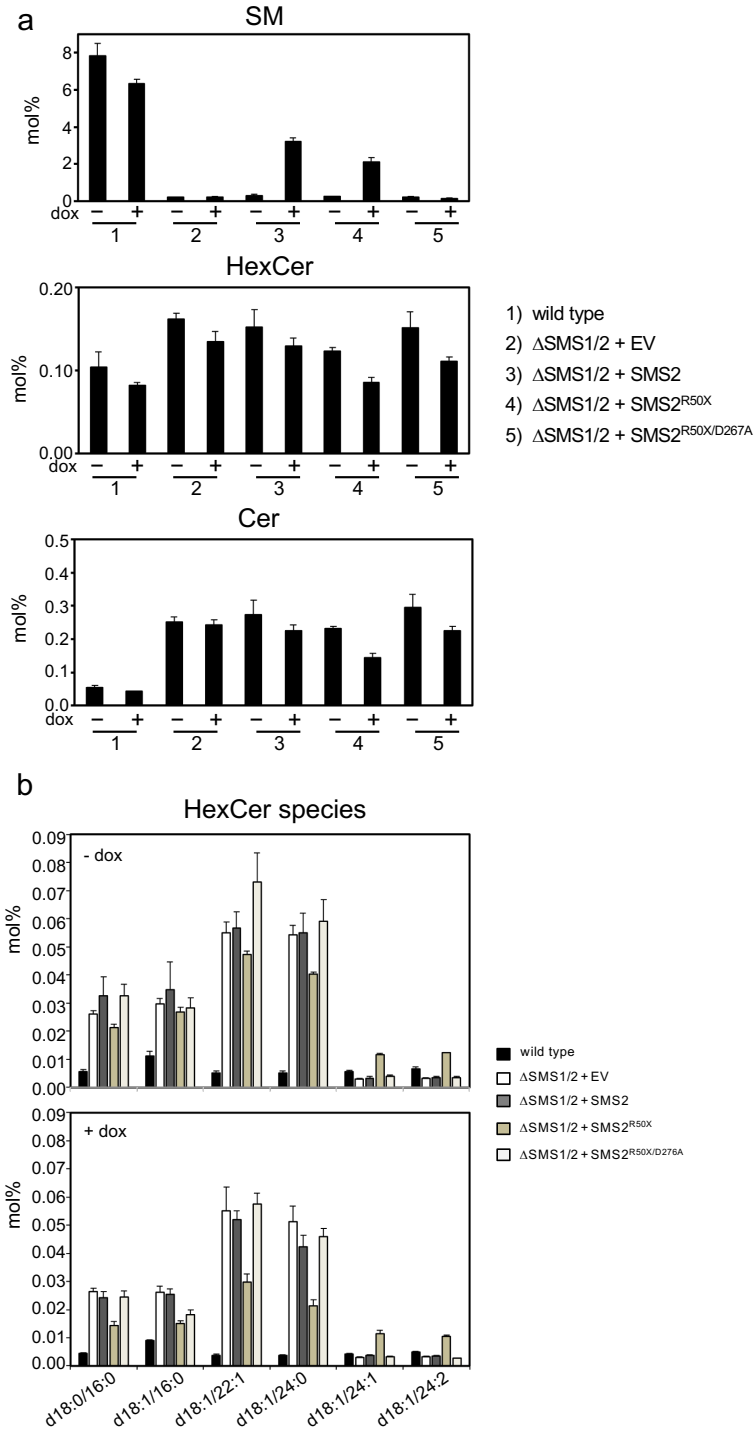

Fig. 23. Pathogenic SMS2^{R50X} supports SM production.
(**a**) HeLa ΔSMS1/2 cells stably transduced with doxycycline-inducible HA-tagged SMS2 or SMS2^{R50X}, or the enzyme dead isoform, SMS2$^{R50X/D276A}$ were grown for 16 h in the absence or presence of doxycycline and subjected to total lipid extraction. Cellular SM, glycosphingolipid (HexCer) and ceramide (Cer) levels were quantified by LC-MS/MS and expressed as mol% of total phospholipid analyzed. (**b**) HexCer species in total lipid extracts of cells treated as in (a) were quantified by LC-MS/MS and expressed as mol% of total phospholipid analyzed.

4.9. Pathogenic variant SMS2^{R50X} is mistargeted to the early Golgi

To determine the subcellular localization of SMS2^{R50X}, cells were grown in the presence or absence of doxycycline for 16 h, immunostained against anti-HA and anti-calnexin antibodies and examined by immunofluorescence microscopy. The results show that in contrast to wildtype SMS2, which is localized to the *trans*-Golgi/PM, SMS2^{R50X} localized solely to the Golgi apparatus indicating that the mutant is exported out of the ER but does not arrive at the PM (**Fig. 24a and b; Fig. S6**). To determine the exact Golgi compartment where SMS2^{R50X} is localized, I used the fungal metabolite, brefeldin A (BFA). By inhibiting the formation of COPI-vesicles, BFA redistributes *cis*-Golgi proteins but not *trans*-Golgi proteins to the ER (Reaves and Banting, 1992). Upon BFA treatment, wildtype SMS2 displayed a reticular distribution typical of proteins of the trans-Golgi/PM while SMS2^{R50X} displayed an ER staining pattern implying that the mutant is retained in early Golgi compartments (**Fig. 24c**). This could explain the relatively lower steady state SM level in SMS2^{R50X} expressing cells. Unlike the other pathogenic isoforms, SMS2^{R50X} has no direct access to ER-derived ceramides and must compete with GlcCer synthase for ceramides delivered to the early Golgi. Altogether, this data indicates that pathogenic SMS2^{R50X} supports bulk production of SM in the early Golgi compartment. As SM synthesized in the ER of cells expressing ER-resident SMS2 mutants, SMS2^{I62S} and SMS2^{M64R} gains exposure to the cytosol, I examined if the same applies to SM produced in the early Golgi by SMS2^{R50X} mutant. To test this, I expressed SM binding probe, EqtSM$_{cyto}$ in SMS2^{R50X} cells. I did not find recruitment of the probe to any specific membrane as the probe remained cytosolic (**Fig. S7**). I also did not observe any aberrant distribution of the sterol D4H probe in these cells (**Fig. S8**). One possibility could be that the perturbations to SM distribution caused by SMS2^{R50X} are more subtle and less pronounced than perturbations caused by other pathogenic SMS2 variants.

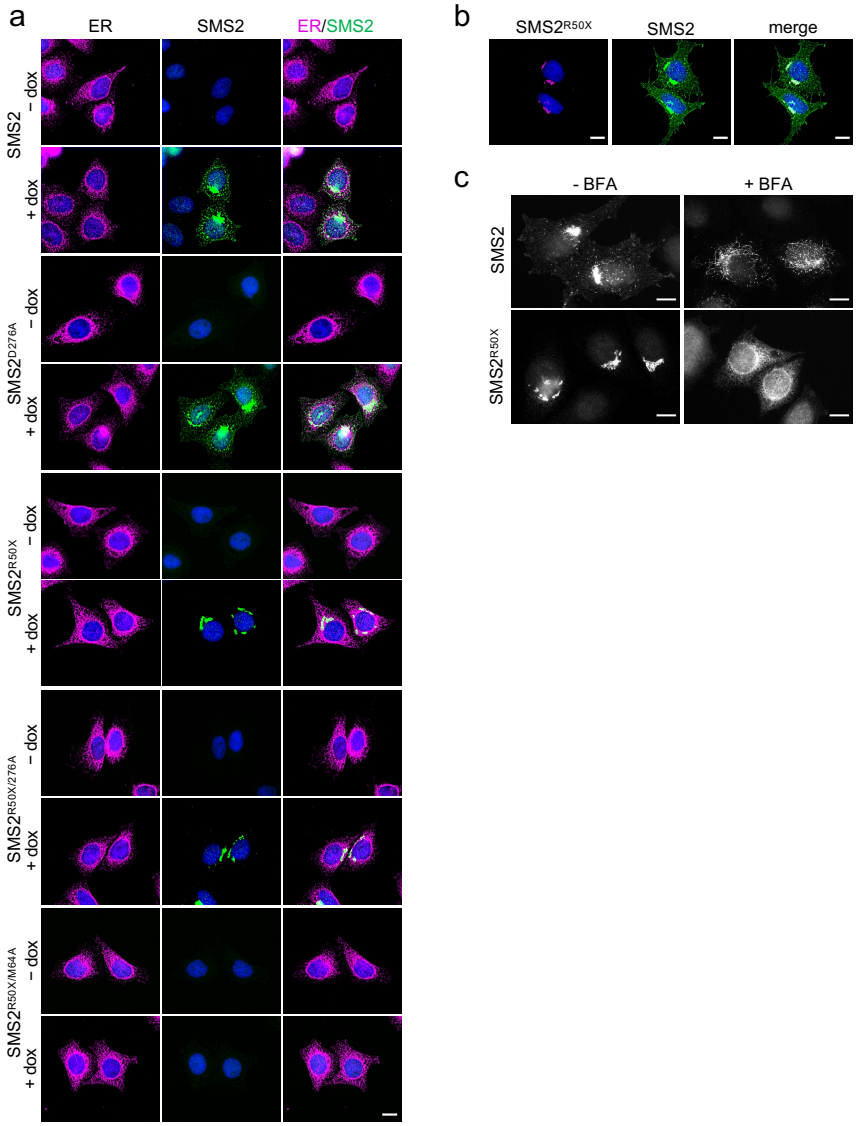

Fig. 24. Pathogenic SMS2^{R50X} is retained in the early Golgi.
(a) HeLa ΔSMS1/2 cells stably transduced with doxycycline-inducible HA-tagged SMS2 or SMS2^{R50X}, or their enzyme dead isoforms SMS2^{D276A}, SMS2$^{R50X/D276A}$ or a double mutant, SMS2$^{R50X/M64A}$ were grown for 16 h in the absence or presence of doxycycline, fixed and stained with α-HA (*green*) and α-Calnexin (*magenta*) antibodies, counterstained with DAPI (*blue*) and imaged by DeltaVision microscopy.(**b**) HeLa ΔSMS1/2 cells stably transduced with doxycycline-inducible HA-tagged SMS2 or SMS2^{R50X} were transfected with V5-tagged SMS2 and grown for 16 h in the presence of doxycycline. Next, cells were fixed and stained with α-HA (*magenta*) and α-V5 (*green*) antibodies, counterstained with DAPI (*blue*) and imaged by DeltaVision microscopy. (**c**) HeLa ΔSMS1/2 cells stably transduced with doxycycline-inducible HA-tagged SMS2 or SMS2^{R50X} were grown for 16 h in the presence of doxycycline. Cells were subsequently incubated in the absence or presence of 5 µg/ml BFA for 4 hours, fixed and stained with α-HA antibody and visualized by Leica fluorescence microscopy. Scale bars, 10 µm.

5. DISCUSSION

SM constitutes a dominant sphingolipid in mammalian cells that is specifically enriched in the exoplasmic leaflets of the PM, the *trans*-Golgi and endolysosomal organelles. While maintenance of these nonrandom SM distributions is thought to be of fundamental importance for a variety of physiological processes, experimental proof for this concept is scarce. Herein, I demonstrated that pathogenic SMS2 variants p.M64R and p.I62S identified in patients with a severe form of osteoporosis cause profound perturbations in the subcellular organization of SM and cholesterol. Both variants are unable to leave the ER owing to a defective autonomous ER export signal in their *N*-terminal cytosolic tail. Consequently, bulk production of SM is mistargeted to the ER, the site for de novo synthesis of the SM precursor ceramide. I found that cells expressing pathogenic SMS2 variants accumulate PM-like SM levels in the ER and fail to establish a strict SM asymmetry across the PM, presumably due to a constitutive SM scrambling in the ER. These aberrant SM distributions also occur in patient-derived fibroblasts and are accompanied by significant imbalances in cholesterol organization and lipid order along the secretory pathway. I also found that the less pathogenic but more common SMS2 variant p.R50X gives rise to a truncated active enzyme owing to the use of Met64 as alternative start codon. Interestingly, the truncated enzyme is mistargeted to an early Golgi compartment. Based on these findings, I postulate that pathogenic SMS2 variants undermine the capacity of osteogenic cells to uphold fundamental nonrandom lipid distributions that are critical for their bone-forming activity.

5.1. Pathogenic SMS2 variants undermine the ability of cells to uphold SM gradients

MS-based lipidomics is a valuable tool to map organellar lipidomes (Hornig-Do *et al.*, 2009; Yang and Han, 2016). In this study, I combined high affinity immunocapture with MS-based lipidomics to analyze the ER and PM lipidomes of cells expressing pathogenic SMS2 variants. As depicted in **Fig. 25**, cells expressing pathogenic SMS2 variants displayed a dramatic rise in SM levels. This was accompanied by a rise in DAG, increase in PE, decrease in PC and no significant change to cholesterol levels (**Fig. 25**). Details and implications of changes to the ER lipid profile are discussed in section **5.3**. Despite the rise in ER-bound SM levels, lipidomic analysis did not reveal any significant change to the PM lipidome of cells expressing pathogenic SMS2 variants. A major drawback of lipidomics is that it cannot directly report on transbilayer orientation of lipids. In this respect, non-lytic lipid binding proteins hold great potential for probing subcellular lipid localization and transbilayer lipid distribution (Makino *et al.,* 2017; Kobayashi *et al.*, 2021). By employing a non-lytic protein-based SM reporter, equinatoxin, I was able to detect remarkable disruptions to transbilayer SM asymmetry at the ER and at the PM as discussed below. These complimentary tools used in this study, present a powerful combination for studying subcellular lipid dynamics and organization.

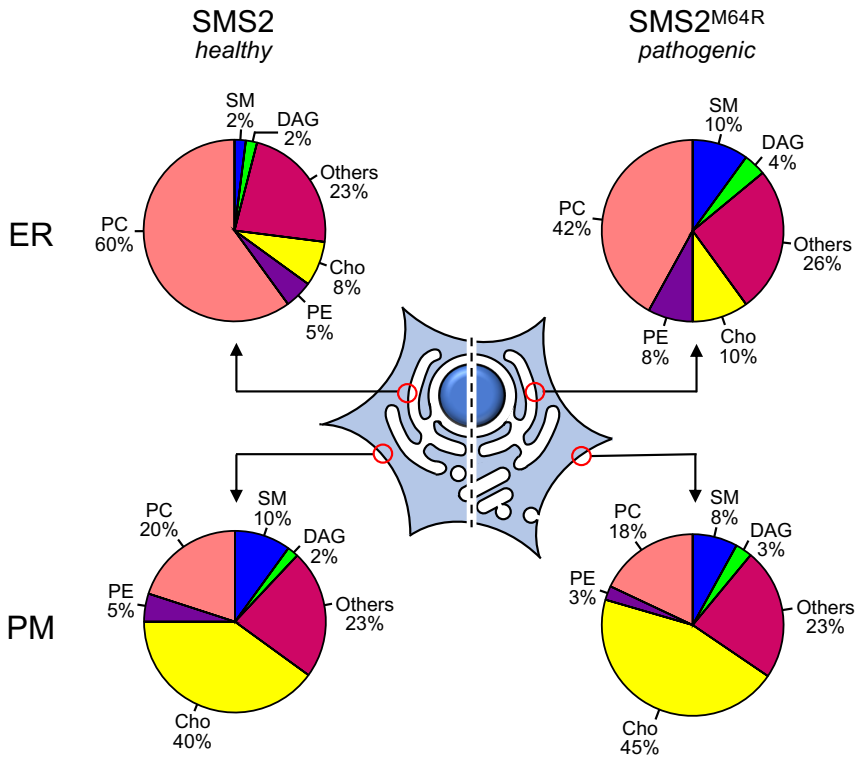

Fig. 25. Impact of pathogenic SMS2 variants on lipid composition of ER and PM
Lipid composition of ER and PM of cells expressing wildtype SMS2 and pathogenic SMS2 variants, $SMS2^{I62S}$ or $SMS2^{M64R}$ as determined in this work. Remarkably, the ER of pathogenic SMS2 expressing cells contains five-fold more SM and two-fold more DAG compared to wildtype. This is accompanied by a 2-fold increase in PE-containing lipids and a significant decrease in PC species. Unexpectedly, cholesterol levels in the ER of cells expressing pathogenic SMS2 are barely altered despite high SM content. Cellular adaptive changes in response to the rise in ER SM levels are reflected in the increase in desaturation of phospholipids (not shown, see section 5.3 of text). However, the PM lipidome of pathogenic SMS2 expressing cells only shows a slight reduction in SM content. Other bulk lipids do not show any marked changes.

Using a version of equinatoxin that allows detection of luminal SM (Deng *et al.*, 2016), I detected a SM pool on the luminal ER leaflet of cells expressing pathogenic SMS2 variants. However, as phospholipid biosynthesis in the ER is asymmetric, half of the newly synthesized phospholipids deposited in one ER leaflet must be readily moved to the opposite leaflet to ensure balanced growth of the bilayer. This cross-bilayer movement of phospholipids is not spontaneous but relies on ATP-independent, bidirectional, and constitutively active phospholipid scramblases (Pomorski and Menon, 2016). Indeed, recent studies reported distinct ER-resident proteins with phospholipid scramblase activity (Ghanbarpour *et al.*, 2021; Li *et al.*, 2021; Huang *et al.*, 2021). As a group, ER-resident scramblases display a relatively low specificity with phospholipids and sphingolipids like SM being translocated with similar kinetics (Buton *et al.*, 2002; Chalat *et al.*, 2002). I therefore anticipated that SM synthesized by pathogenic SMS2 variants in the luminal ER leaflet would readily equilibrate with the cytosolic leaflet. In agreement with this prediction, I observed that pathogenic SMS2 variants selectively induced mobilization of a cytosolic SM reporter in patient-derived fibroblasts or upon their heterologous expression in HeLa cells. Additionally, cells harboring a pathogenic SMS2 variant had comparable amounts of PM-bound SM as controls (**Fig. 25**) but displayed a significantly reduced SM reporter staining

of their surface. Consistent with a reduced exoplasmic SM pool, these cells also displayed a lower surface lipid packing and lost their viability more rapidly when exposed to a cholesterol-absorbing agent than controls. Consistent with an expanded cytoplasmic SM pool, expression of pathogenic SMS2 variants constrained accessibility of PM-associated cholesterol for a cytosolic sterol reporter that binds free cholesterol but not cholesterol sequestered by SM (Das *et al.*, 2014). From this I infer that pathogenic SMS2 variants in fact disrupt two types of cellular SM gradients: one running along the secretory pathway and the other one across the bilayer of secretory organelles (**Fig. 25**; **Fig. 26**). Disruption of the latter affects the equilibrium between active and SM-sequestered cholesterol pools on both sides of the PM (**Fig. 26**).

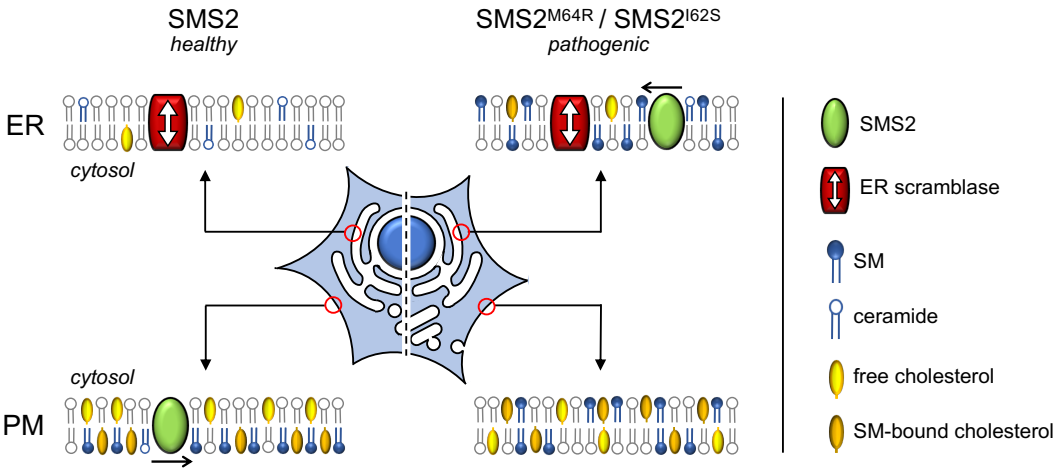

Fig. 26. Impact of pathogenic SMS2 variants on the transbilayer SM and cholesterol organization.
While the ER of normal cells contains only minute amounts of SM (~2%), the ER of cells expressing pathogenic SMS2 variants, SMS2^{I62S} or SMS2^{M64R} contains PM-like levels of SM. SM produced in the ER is equilibrated across the ER bilayer by phospholipid scramblases. This in turn contributes to SM scrambling across the PM bilayer giving rise to a pool of SM at the cytoplasmic leaflet of the PM that normally does not exist there. The cytoplasmic pool of SM sequesters cholesterol making it inaccessible for a sterol probe that binds free cholesterol.

5.2. Impact of disrupted SM gradients on cholesterol organization and lipid order

The bulk production of SM in the *trans*-Golgi is thought to create a thermodynamic trap for cholesterol synthesized in the ER. This arrangement promotes the formation of a cholesterol concentration gradient along the secretory pathway (Bigay and Antonny, 2012; Hothuis and Mennon, 2014). However, lipidomics data in this study clearly indicate that cells harboring a pathogenic SMS2 variant retain the ability to effectively concentrate cholesterol in the PM and keep their ER levels low in spite of a dissipated SM gradient (**Fig. 25**). This implies that cells are equipped with an effective mechanism to avoid a potentially toxic rise of cholesterol in ER bilayers with an abnormally high SM content.

A possible mechanism to clear excess cholesterol from the ER involves its esterification and storage in lipid droplets (Ikonen, 2008; Olzmann and Carvalho, 2019). However, expression of pathogenic SMS2 variants had no significant impact on the cellular pool of cholesteryl esters. An alternative mechanism for clearing excess ER cholesterol involves

the oxysterol binding protein OSBP, which can mediate net transfer of cholesterol from the ER to the *trans*-Golgi. OSBP-catalyzed transport of cholesterol against its concentration gradient is energized by the counter transport of phosphatidylinositol-4-phosphate (PI4P), a lipid that is continuously produced in the *trans*-Golgi and turned over in the ER (Mesmin *et al.*, 2013; Capasso *et al.*, 2017). Previous work showed that the cholesterol/PI4P exchange activity of OSBP makes a very significant contribution to the intracellular flows of cholesterol and is large enough to impact the general landscape of lipid order along membranes of the secretory pathway at the expense of a massive PI4P consumption (Mesmin *et al.*, 2017). Therefore, future studies addressing whether pathogenic SMS2 variants trigger an upregulation of the PI4P-consuming OSBP cycle to counteract thermodynamic trapping of cholesterol by an expanding SM pool in the ER may prove fruitful.

The PI4P-dependent countertransport mechanism originally proposed to energize net transfer of cholesterol from the ER to the *trans*-Golgi also appears to play a critical role in driving PS export from the ER and generating a PS concentration gradient along the secretory pathway (Chung *et al.*, 2015; Moser von Filseck *et al.*, 2015). Data in this study indicate that such a mechanism does not exist for SM and that the ER is ill-equipped to effectively remove bulk amounts of SM produced there. In the absence of any lipid transfer protein dedicated to mediate anterograde SM transport, the only mechanism available for SM to leave the ER is by vesicular transport. Previous work revealed that SM and cholesterol are significantly depleted from coated protein complex I (COPI)-coated vesicles compared with their donor Golgi cisternae (Brügger *et al*., 2000), a finding supporting the view that formation of the SM gradient along the secretory pathway critically relies on a mechanism that prevents Golgi-derived SM from gaining access to the retrograde moving COPI vesicles. Experiments with giant unilamellar vesicles (GUVs) containing ternary mixtures of PC, SM and cholesterol provided evidence for curvature-based lipid sorting, demonstrating that membrane tubes pulled from the giant vesicles are efficiently depleted of SM and cholesterol relative to vesicle membranes with essentially negligible curvature (Roux et al., 2015). The same principles may hamper an efficient coated protein complex II (COPII)-mediated export of SM from the ER, thus contributing to a compromised SM gradient along the secretory pathway of cells harboring pathogenic SMS2 variants.

SM alongside sterols are major determinants of membrane lipid order (Bigay and Antonny, 2012; Slotte, 2013). Their enrichment at the trans-Golgi and PM contributes to the thick and tightly packed nature of these membranes (Harayama and Reizmann, 2018). Given the important contribution of SM gradients to proper maintenance of lipid order along the secretory pathway, I anticipated that dissipation of SM gradients may impact the lipid order of early and late secretory organelles. To this end, I employed organelle-targeted reporters to probe lipid order at the ER and at the cell surface (Danylchuk *et al.*, 2021). I found that cells harboring pathogenic SMS2 variants displayed a marked rise in lipid order at the ER and a decrease in lipid order at the cell surface. This was not only true for engineered cell lines but also for patient-derived fibroblasts. From this I infer that dissipation of SM gradients causes disturbances to cholesterol organization and lipid order along the secretory pathway.

5.3. Cellular response to an assault on the ER lipid code

This study also yields interesting insights into how cells respond to a major assault on the lipid composition of the ER. Pathogenic SMS2 variants cause a dramatic rise in ER-bound SM, reaching levels normally found only in the PM. This was accompanied by two notable changes in the bulk phospholipid pool, namely a marked increase in phospholipid desaturation and a nearly two-fold expansion of ethanolamine-containing phospholipids at the expense of choline-containing ones. How these alterations in the ER phospholipid profile are implemented remains to be established. However, it is tempting to speculate that they serve to buffer the biophysical properties of the ER bilayer from SM-induced perturbations.

Owing to the low degree of unsaturation in both its long-chain base and *N*-linked acyl chain, SM forms a taller, narrower cylinder than PC, increasing its membrane packing density and affinity for cholesterol (Slotte, 2013). These features make SM ideally suited to support the barrier function of the PM, which relies on a tightly packed, defect-free bilayer. In contrast, the biogenic activities of the ER require a more loosely packed lipid bilayer (Bigay and Antonny, 2013; Nilsson *et al.*, 2001). Thus, an enhanced phospholipid desaturation and rise in cone-shaped, ethanolamine-containing phospholipids may be part of an adaptive cellular response to mitigate a SM-mediated rigidification of the ER bilayer. Despite these notable changes to phospholipid composition, the significant alteration to lipid order of the ER membrane suggests that the organelle struggles to cope with the remarkable rise in SM levels which may bear consequences for the organelle's central function in protein biogenesis and secretion.

Besides a significant impact on the bulk phospholipid composition of the ER, pathogenic SMS2 variants also caused a sharp rise in ER-bound Cer1P levels. Cer1P is produced by ceramide kinase CERK and functions as a key signaling lipid in the regulation of cell growth, survival and inflammation (Arana *et al.*, 2012; Yu et al., 2019; Presa *et al*., 2020). Besides stimulating the production of arachidonic acid and pro-inflammatory cytokines through direct activation of group VI cytosolic phospholipase A2a (Lamour *et al.*, 2009), Cer1P promotes cell survival at least in part by blocking enzymes involved in ceramide production including serine palmitoyl transferase and acid sphingomyelinase (Gómez-Muñoz *et al.*, 2004; Granado *et al*., 2009). My present findings indicate that Cer1P production is tightly coupled to SM biosynthesis. The prospect that CERK-mediated Cer1P formation also serves a role in the mechanism by which cells sense and respond to imbalances in the lipid composition of their secretory organelles deserves further consideration and should be addressed in future investigations.

5.4. Pathogenic SMS2^{R50X} yields an active enzyme mistargeted to the early Golgi

The most severe clinical manifestations of OP-CDL are associated with the missense variants p.I62S and p.M64R that block export of functional SMS2 from the ER. However, the nonsense variant p.R50X is more common, with patients presenting a milder phenotype (Pekinnen *et al.,* 2019; Basalom *et al.,* 2021; Makitie *et al.,* 2021). How this nonsense variant causes bone disease is not known. Pekinnen *et al*., reported that p.R50X encodes a truncated enzyme lacking the entire transmembrane helices including the active sites of the

enzyme (Pekinnen *et al.,* 2019). Here, I report that this mutation results in production of a truncated but active enzyme with Met64 serving as an alternative start methionine. While this mutation does not affect ER export, I show that the variant fails to reach the plasma membrane and instead accumulates in the *cis* or *medial* cisternae of the Golgi complex. Why this mutant remains in the early Golgi and does not arrive at the plasma membrane remains to be investigated. It is worthy of note that the early Golgi is not the *bona fide* subcellular localization of SMS2 nor SMS1 which localizes to the *trans*-Golgi/PM and *trans*-Golgi respectively (Huitema *et al.*, 2004; Tafesse *et al.*, 2007). Employing lipidomic analysis approach, I found that cells expressing SMS2^{R50X} support SM production albeit to a lower degree than wildtype or other pathogenic SMS2 variants. A plausible explanation is that the Golgi-resident mutant has no direct access to newly synthesised ceramide in the ER compared to ER-resident pathogenic mutants. SM produced in the *cis*-Golgi may contaminate ER pool of lipids leading to subsequent scrambling of SM across the ER bilayer which would be ultimately mirrored in late secretory organelles (**Fig. 27**). Although I did not observe mobilization of a cytosolic SM probe, this could be because the SM levels produced by this mutant are below the binding threshold of the probe used.

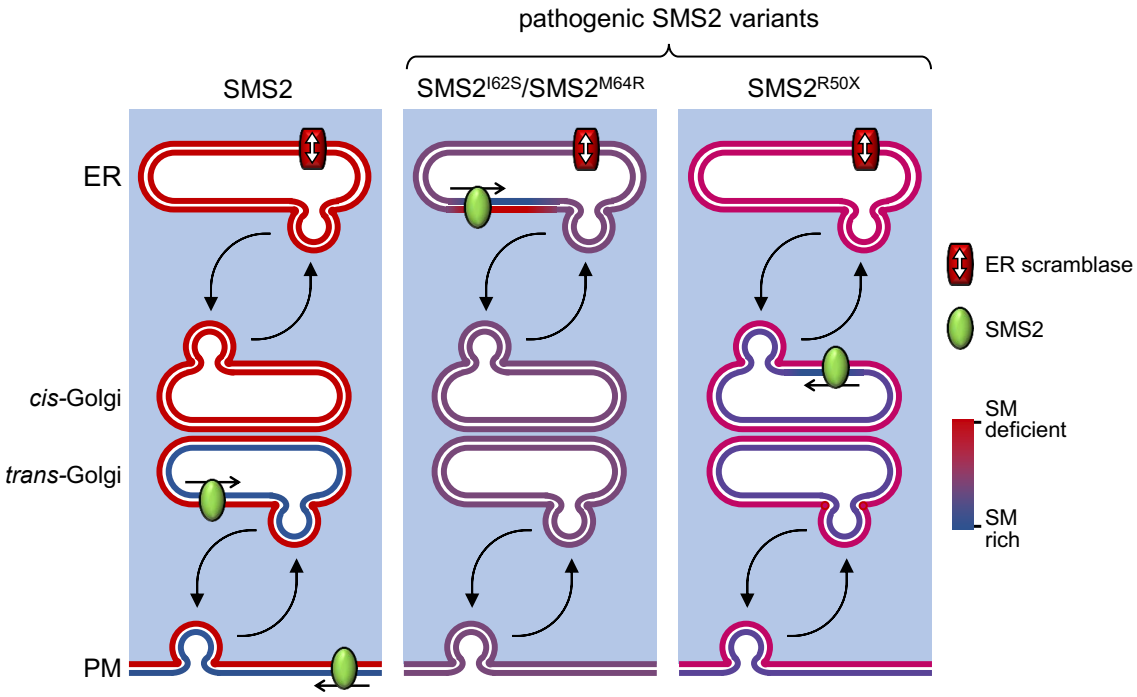

Fig. 27. Pathogenic SMS2 variants dissipate SM gradients along the secretory pathway
SM asymmetry is strictly maintained across the bilayer of late secretory organelles with the highest concentrations found in the exoplasmic leaflets of the *trans*-Golgi and plasma membrane (*left*). Pathogenic SMS2 variants, SMS2^{I62S}/SMS2^{M64R} are mistargeted to the ER and accumulate a pool of SM that is equilibrated across the organelle's bilayer presumably by phospholipid scramblases. This in turn is reflected in disruption of SM asymmetry along the secretory pathway (*middle*). I speculate that SM produced in the early-Golgi compartment by SMS2^{R50X} contaminates the ER bilayer leading to disruption of transbilayer SM asymmetry across the organelle's bilayer and consequently across the bilayer of secretory organelles (*right*).

SM produced at the *trans*-Golgi has been shown to trigger a negative feedback loop that is critical for maintaining post *trans*-Golgi sphingolipid content and counteracting alterations

to metabolic lipid fluctuations (Capasso *et al.*, 2017). CERT delivers ER-synthesized ceramide to the *trans*-Golgi for SM production, a process dependent on the consumption of *trans*-Golgi localized PI4P. The lipid-transfer protein OSBP mediates the transport of PI4P from the *trans*-Golgi to the ER for its dephosphorylation by Sac1 (Mesmin *et al.*, 2013). The dephosphorylation of PI4P has been shown to promote SM and GSL synthesis (Capasso *et al.*, 2017). This homeostatic regulation is important for the recruitment of factors involved in membrane deformation and membrane budding (Lenoir *et al.*, 2010; Cruz-Garcia *et al.*, 2013). By redirecting SM production to the *cis/medial*-Golgi, the site of SM production is uncoupled from that of PI4P, and this may render the afore-described homeostatic circuit dysfunctional and perturb important processes such as membrane budding.

5.5. Potential impact of disrupted SM gradients on osteogenesis

The finding that pathogenic SMS2 variants affect the subcellular organization of SM and cholesterol raises the question how this may contribute to the development of OP-CDL in affected patients. Addressing this question will obviously require experimental models beyond the engineered cell lines and patient-derived fibroblasts used in this study. In this respect, it is important to note that a quantitative analysis of SMS2 transcript levels in a murine tissue panel revealed the highest expression in cortical bone and vertebrae (Pekkinen *et al.*, 2019). I therefore anticipate that the impact of pathogenic SMS2 variants on the lipid composition of secretory organelles will be more severe in bone cells than in fibroblasts from the affected individuals. Bone formation involves the deposition of collagen fibrils into a matrix and its subsequent mineralization (Stephens, 2012; Murshed, 2018). Collagens are synthesized as pre-procollagen in the ER and exit the ER as pro-collagen. The exit of pro-collagen from the ER depends on the COPII coat which comprises the core components- Sar1, Sec23/24 and Sec13/31. Interestingly, pathogenic mutations of Sec23 and Sec24 which cause craniofacial and skeletal defects have been reported to selectively disrupt procollagen export from the ER but not secretion of other proteins (Boyadjiev *et al.*, 2006; Garbes *et al.*, 2015; Lu *et al.*, 2022). Moreover, loss of TANGO1, an ER-resident transmembrane protein required for packaging the bulky procollagen fibers into COPII vesicles, results in neonatal lethality due to insufficient bone mineralization (**Fig. 28;** Guillemyn *et al.*, 2021). It is conceivable that ER export of procollagen is particularly susceptible to the bilayer rigidifying effect of bulk SM production by pathogenic SMS2 variants (**Fig. 28**).

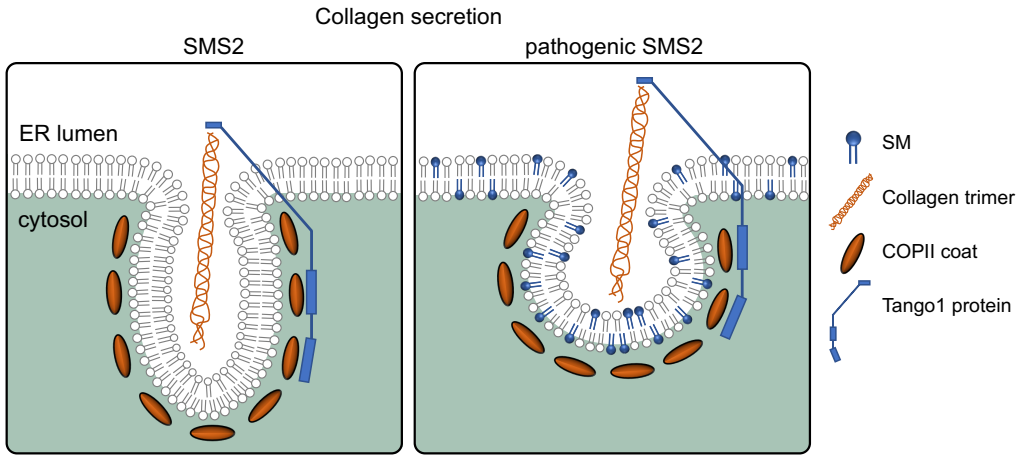

Fig. 28. Model of how pathogenic SMS2 mutants may impact collagen secretion.
The synthesis of collagen begins in the ER. Pro-collagen trimers exit the ER in large secretory cargos that involves the assembly of COPII coat proteins and accessory protein TANGO. Mutations in COPII components and TANGO have been implicated in impaired collagen secretion (see text). I postulate that the formation of these large cargos would be impaired by the rigidifying effect of SM on both leaflets of the ER bilayer. This, in turn, would prevent the proper export of collagen trimers from the ER.

However, an alternative scenario is that a disrupted SM asymmetry at the PM of osteogenic cells harboring a pathogenic SMS2 variant negatively affects bone mineralization. This process is initiated by the release of matrix vesicles that bud off from the apical membrane of osteoblasts and deposit their Ca^{2+} and phosphate-rich content where matrix mineralization is propagated (**Fig. 29**; Murshed 2018). Bone mineralization also critically relies on neutral SMase-2 (SMPD3), a membrane-bound enzyme that cleaves SM in the cytosolic leaflet of the PM to generate ceramide and phosphocholine (Aubin *et al*., 2005). Phosphocholine is thereafter cleaved by PHOSPHO1 to liberate free Pi. Increase in intravesicular Pi leads to its precipitation with Ca^{2+} to form hydroxyapatite. nSMase-2 deficiency leads to mineralization defects of skeletal tissues (Thouverey *et al.,* 2009; Alebrahim *et al.*, 2014; Khavandgar and Murshed, 2015). How nSMase-2 gains access to SM, which is normally concentrated in the exoplasmic leaflet, has remained unclear. However, it was recently demonstrated that minor lesions in PM integrity triggers a rapid SM scrambling that requires the Ca^{2+}-activated scramblase TMEM16F (Niekamp *et al.*, 2022). Intriguingly, TMEM16F is highly expressed in skeletal tissues and its loss leads to decreased mineral deposition (Ehlen *et al.*, 2013), suggesting that this process is critically dependent on a TMEM16F-mediated supply of exoplasmic SM to nSMase-2 for SM hydrolysis in the cytosolic leaflet. This arrangement may serve to ensure a continuous supply of phosphocholine as a source of phosphate required for normal bone mineralization (Pekkinen *et al.*, 2019). By disrupting SM asymmetry, pathogenic SMS2 variants may cause a premature exhaustion of the lipid-based phosphate store, thus interfering with normal bone mineralization (**Fig. 29**).

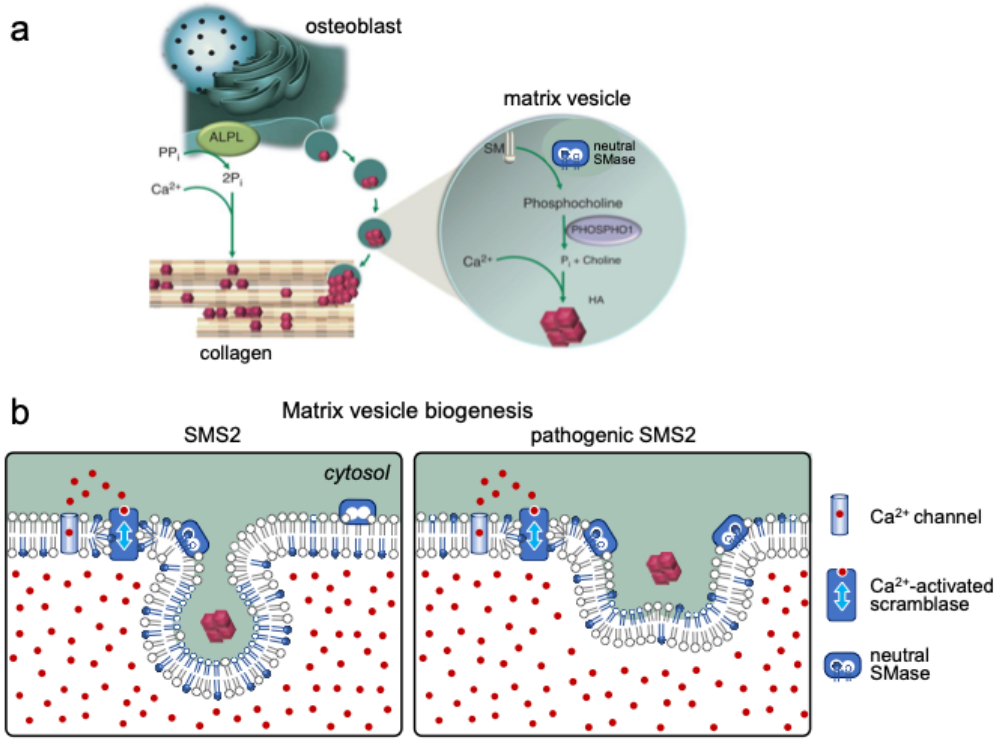

Fig. 29. Model of how pathogenic SMS2 mutants may impact matrix vesicle biogenesis. (**a**) Alkaline phosphatase (ALPL) is an enzyme present on osteoblast cell membrane. It facilitates bone mineralization by cleaving the mineralization inhibitor, inorganic pyrophosphate (PP_i) to yield Pi. An alternative mechanism is mediated by matrix vesicles. Matrix vesicles (MVs) are nanosized vesicles released by osteoblast cells at an initial point of calcification. Neutral sphingomyelinase (nSMase) present on MVs cleaves sphingomyelin (SM) to generate phosphocholine which in turn is cleaved by PHOSPHO1 to liberate free Pi. Increased intravesicular Pi is precipitated with Ca^{2+} to generate nascent hydroxyapatite (HA) crystals which are then deposited into collagen fibrils. (**b**) The SM-operated pathway of MV biogenesis is dependent on a Ca^{2+}-activated scramblase and nSMase. In normal cells, SM is concentrated on the exoplasmic leaflet of the plasma membrane. SM scrambled to the cytosolic leaflet by Ca^{2+}-activated scramblase is turned over by nSMase. In this way, the bulky phosphocholine headgroup of SM is cleaved to generate ceramide, a lipid with a smaller head group. Ceramides then self-aggregate thereby causing a local condensation of the cytosolic leaflet. This, in turn, fuels an inverse budding of the bilayer away from the cytosol and the eventual release of MVs. In cells expressing pathogenic SMS2 variants having a disrupted SM asymmetry, it is conceivable that cytosolically-exposed SM is constitutively turned-over to ceramide prematurely, inadvertently depleting the fuel that drives MV biogenesis. Panel a adapted from Murshed (2018).

Moreover, it is important to consider that ceramides formed during SM hydrolysis by nSMase-2 in the cytosolic leaflet of the PM may also serve a critical role (Burello *et al.*, 2020). Owing to their cone-shaped structure, ceramides released by SM turnover readily self-assemble into microdomains that possess a negative spontaneous curvature (Rogasevskaia and Coorssen 2006; Alonso and Goni, 2018). By causing a local condensation of the cytosolic leaflet, nSMase-mediated conversion of SM to ceramide may promote an inverse budding of the bilayer away from the cytosol (**Fig. 29**; Menck *et al.*, 2017; Niekamp *et al.*, 2022). I postulate that this process may play a crucial role in the biogenesis of matrix vesicles required for normal bone mineralization. According to this model, pathogenic SMS2 variants may interfere with matrix vesicle formation because dissipation of SM asymmetry across the PM would deplete the fuel that drives this process.

6. CONCLUSION AND OUTLOOK

CONCLUSION

The work presented herein indicates that bone critical SMS2 variants p.M64R and p.I62S exert their pathogenic effects by redirecting bulk SM production to the ER, thereby causing significant deviations in organellar lipid compositions and membrane properties along the secretory pathway. Also relevant in this respect is that a less severe but more common bone critical SMS2 variant, p.R50X, gives rise to a truncated, catalytically active enzyme that is mistargeted to the *cis/medial*-Golgi. Collectively, these findings highlight how cells respond to a major assault on the lipid composition of early secretory compartments and provide a valuable basis to resolve the pathogenic mechanism underlying OP-CDL.

OUTLOOK

Future studies should investigate how pathogenic SMS2 variants may impact osteogenesis. To this end, disease-relevant models bearing pathogenic SMS2 variants should be employed such as hiPSC-derived osteoblasts, osteosarcoma/osteoblasts cell lines or Zebrafish models. These models are advantageous in that they can be directly used to test the impact of pathogenic SMS2 variants on: i) collagen secretion using collagen binding dyes; ii) mineralization potential of cells in 3D co-cultures with osteocytes and osteoclasts; iii) the quantity and content of matrix vesicles formed by mineralizing cells.

Future experiments should also address the possible upregulation of ER cholesterol export machinery in cells expressing pathogenic SMS2 variants. By pharmacologically inhibiting ER cholesterol exporter, OSBP, one could investigate the dependence of cells expressing pathogenic SMS2 variants on an upregulated cholesterol export. Complimentarily, monitoring the subcellular localization of fluorescently-tagged OSBP in these cells could prove insightful. PI4P consumption rate could also be examined using PI4P specific probes. Another interesting finding from this study that merits exploration is the potential link between SM and Cer1P production. Monitoring the subcellular localization of fluorescently-tagged CERK or Cer1P transfer protein -CPTP, may provide insight into a likely reorganization of Cer1P metabolic network that is dependent on the subcellular dynamics of SM.

7. REFERENCES

Abe, M., Makino, A., Hullin-Matsuda, F., Kamijo, K., Ohno-Iwashita, Y., Hanada, K., Mizuno, H., Miyawaki, A., & Kobayashi, T. (2012). A role for sphingomyelin-rich lipid domains in the accumulation of phosphatidylinositol-4,5-bisphosphate to the cleavage furrow during cytokinesis. *Molecular and cellular biology*, *32*(8), 1396–1407.

Alebrahim, S., Khavandgar, Z., Marulanda, J., & Murshed, M. (2014). Inducible transient expression of Smpd3 prevents early lethality in fro/fro mice. *Genesis 52*(5), 408–416.

Alonso, A., & Goñi, F. M. (2018). The Physical Properties of Ceramides in Membranes. *Annual review of biophysics*, *47*, 633–654.

Anderluh, G., Pungercar, J., Strukelj, B., Macek, P., & Gubensek, F. (1996). Cloning, sequencing, and expression of equinatoxin II. *Biochemical and biophysical research communications*, *220*(2), 437–442.

Arana, L., Gangoiti, P., Ouro, A., Rivera, I. G., Ordoñez, M., Trueba, M., Lankalapalli, R. S., Bittman, R., & Gomez-Muñoz, A. (2012). Generation of reactive oxygen species (ROS) is a key factor for stimulation of macrophage proliferation by ceramide 1- phosphate. *Experimental cell research*, *318*(4), 350–360.

Bakrac, B., Gutiérrez-Aguirre, I., Podlesek, Z., Sonnen, A. F., Gilbert, R. J., Macek, P., Lakey, J. H., & Anderluh, G. (2008). Molecular determinants of sphingomyelin specificity of a eukaryotic pore-forming toxin. *The Journal of biological chemistry*, *283*(27), 18665–18677.

Basalom, S., Fiscaletti, M., Miranda, V., Huber, C., Couture, G., Drouin, R., Monceau, É., Wavrant, S., Dubé, J., Mäkitie, O., Cormier-Daire, V., & Campeau, P. M. (2021). Calvarial doughnut lesions with bone fragility in a French-Canadian family; case report and review of the literature. *Bone reports*, *15*, 101121.

Bell, R. M., Ballas, L. M., & Coleman, R. A. (1981). Lipid topogenesis. *Journal of lipid research*, *22*(3), 391–403.

Bengt F., & Ding X. (2009) The ins and outs of phospholipid asymmetry in the plasma membrane: roles in health and disease, *Critical Reviews in Biochemistry and Molecular Biology, 44*:5, 264-277.

Bhat, H. B., Kishimoto, T., Abe, M., Makino, A., Inaba, T., Murate, M., Dohmae, N., Kurahashi, A., Nishibori, K., Fujimori, F., Greimel, P., Ishitsuka, R., & Kobayashi, T. (2013). Binding of a pleurotolysin ortholog from Pleurotus eryngii to sphingomyelin and cholesterol-rich membrane domains. *Journal of lipid research*, *54*(10), 2933–2943.

Bhattacharyya, D., & Glick, B. S. (2007). Two mammalian Sec16 homologues have nonredundant functions in endoplasmic reticulum (ER) export and transitional ER organization. *Molecular biology of the cell*, *18*(3), 839–849.

Bigay, J., & Antonny, B. (2012). Curvature, lipid packing, and electrostatics of membrane organelles: defining cellular territories in determining specificity. *Developmental cell*, *23*(5), 886–895.

Björkbom, A., Róg, T., Kankaanpää, P., Lindroos, D., Kaszuba, K., Kurita, M., Yamaguchi, S., Yamamoto, T., Jaikishan, S., Paavolainen, L., Päivärinne, J., Nyholm, T. K., Katsumura, S., Vattulainen, I., & Slotte, J. P. (2011). N- and O-methylation of sphingomyelin markedly affects its membrane properties and interactions with cholesterol. *Biochimica et biophysica acta*, *1808*(4), 1179–1186.

Blaho, V. A., & Hla, T. (2014). An update on the biology of sphingosine 1-phosphate receptors. *Journal of lipid research*, *55*(8), 1596–1608.

Bligh, E. G., & Dyer, W. J. (1959). A rapid method of total lipid extraction and purification. *Canadian journal of biochemistry and physiology*, *37*(8), 911–917.

Boyadjiev, S. A., Fromme, J. C., Ben, J., Chong, S. S., Nauta, C., Hur, D. J., Zhang, G., Hamamoto, S., Schekman, R., Ravazzola, M., Orci, L., & Eyaid, W. (2006). Cranio-lenticulo-sutural dysplasia is caused by a SEC23A mutation leading to abnormal endoplasmic-reticulum-to-Golgi trafficking. *Nature genetics*, *38*(10), 1192–1197.

Brügger, B., Sandhoff, R., Wegehingel, S., Gorgas, K., Malsam, J., Helms, J. B., Lehmann, W. D., Nickel, W., & Wieland, F. T. (2000). Evidence for segregation of sphingomyelin and cholesterol during formation of COPI-coated vesicles. *The Journal of cell biology*, *151*(3), 507–518.

Burrello, J., Biemmi, V., Dei Cas, M., Amongero, M., Bolis, S., Lazzarini, E., Bollini, S., Vassalli, G., Paroni, R., & Barile, L. (2020). Sphingolipid composition of circulating extracellular vesicles after myocardial ischemia. *Scientific reports*, *10*(1), 16182.

Buton, X., Hervé, P., Kubelt, J., Tannert, A., Burger, K. N., Fellmann, P., Müller, P., Herrmann, A., Seigneuret, M., & Devaux, P. F. (2002). Transbilayer movement of monohexosylsphingolipids in endoplasmic reticulum and Golgi membranes. *Biochemistry*, *41*(43), 13106–13115.

Capasso, S., Sticco, L., Rizzo, R., Pirozzi, M., Russo, D., Dathan, N. A., Campelo, F., van Galen, J., Hölttä-Vuori, M., Turacchio, G., Hausser, A., Malhotra, V., Riezman, I., Riezman, H., Ikonen, E., Luberto, C., Parashuraman, S., Luini, A., & D'Angelo, G. (2017). Sphingolipid metabolic flow controls phosphoinositide turnover at the *trans*-Golgi network. *The EMBO journal*, *36*(12), 1736–1754.

Carquin, M., Conrard, L., Pollet, H., Van Der Smissen, P., Cominelli, A., Veiga-da-Cunha, M., Courtoy, P. J., & Tyteca, D. (2015). Cholesterol segregates into submicrometric domains at the living erythrocyte membrane: evidence and regulation. *Cellular and molecular life sciences: CMLS*, *72*(23), 4633–4651.

Chalat, M., Menon, I., Turan, Z., & Menon, A. K. (2012). Reconstitution of glucosylceramide flip-flop across endoplasmic reticulum: implications for mechanism of glycosphingolipid biosynthesis. *The Journal of biological chemistry*, *287*(19), 15523–15532.

Cho, K. J., van der Hoeven, D., Zhou, Y., Maekawa, M., Ma, X., Chen, W., Fairn, G. D., & Hancock, J. F. (2015). Inhibition of Acid Sphingomyelinase Depletes Cellular Phosphatidylserine and Mislocalizes K-Ras from the Plasma Membrane. *Molecular and cellular biology*, *36*(2), 363–374.

Chung, J., Torta, F., Masai, K., Lucast, L., Czapla, H., Tanner, L. B., Narayanaswamy, P., Wenk, M. R., Nakatsu, F., & De Camilli, P. (2015). PI4P/phosphatidylserine countertransport at ORP5- and ORP8-mediated ER-plasma membrane contacts. *Science, 349*(6246), 428–432.

Clarke, R. J., Hossain, K. R., & Cao, K. (2020). Physiological roles of transverse lipid asymmetry of animal membranes. *Biochimica et biophysica acta. Biomembranes*, *1862*(10), 183382.

Cruz-Garcia, D., Ortega-Bellido, M., Scarpa, M., Villeneuve, J., Jovic, M., Porzner, M., Balla, T., Seufferlein, T., & Malhotra, V. (2013). Recruitment of arfaptins to the trans-Golgi network by PI(4)P and their involvement in cargo export. *The EMBO journal*, *32*(12), 1717–1729.

Dang, T. X., Hotze, E. M., Rouiller, I., Tweten, R. K., & Wilson-Kubalek, E. M. (2005). Prepore to pore transition of a cholesterol-dependent cytolysin visualized by electron microscopy. *Journal of structural biology*, *150*(1), 100–108.

Danylchuk, D. I., Jouard, P. H., & Klymchenko, A. S. (2021). Targeted Solvatochromic Fluorescent Probes for Imaging Lipid Order in Organelles under Oxidative and Mechanical Stress. *Journal of the American Chemical Society*, *143*(2), 912–924.

Danylchuk, D. I., Moon, S., Xu, K., & Klymchenko, A. S. (2019). Switchable Solvatochromic Probes for Live-Cell Super-resolution Imaging of Plasma Membrane Organization. *Angewandte Chemie (International ed. in English)*, *58*(42), 14920–14924.

Das, A., Brown, M. S., Anderson, D. D., Goldstein, J. L., & Radhakrishnan, A. (2014). Three pools of plasma membrane cholesterol and their relation to cholesterol homeostasis. *eLife*, *3*, e02882.

De Colibus, L., Sonnen, A. F., Morris, K. J., Siebert, C. A., Abrusci, P., Plitzko, J., Hodnik, V., Leippe, M., Volpi, E., Anderluh, G., & Gilbert, R. J. (2012). Structures of lysenin reveal a shared evolutionary origin for pore-forming proteins and its mode of sphingomyelin recognition. *Structure, 20*(9), 1498–1507.

de Kroon, A. I., Rijken, P. J., & De Smet, C. H. (2013). Checks and balances in membrane phospholipid class and acyl chain homeostasis, the yeast perspective. *Progress in lipid research*, *52*(4), 374–394.

Deng, Y., Rivera-Molina, F. E., Toomre, D. K., & Burd, C. G. (2016). Sphingomyelin is sorted at the trans Golgi network into a distinct class of secretory vesicle. *PNAS 113*(24), 6677–6682.

Ehlen, H. W., Chinenkova, M., Moser, M., Munter, H. M., Krause, Y., Gross, S., Brachvogel, B., Wuelling, M., Kornak, U., & Vortkamp, A. (2013). Inactivation of anoctamin-6/Tmem16f, a regulator of phosphatidylserine scrambling in osteoblasts, leads to decreased mineral deposition in skeletal tissues. *JBMR*, *28*(2), 246–259.

Eising, S., Thiele, L., & Fröhlich, F. (2019). A systematic approach to identify recycling endocytic cargo depending on the GARP complex. *eLife*, *8*, e42837.

Ellison, C. J., Kukulski, W., Boyle, K. B., Munro, S., & Randow, F. (2020). Transbilayer Movement of Sphingomyelin Precedes Catastrophic Breakage of Enterobacteria-Containing Vacuoles. *Current biology*, *30*(15), 2974–2983.e6.

Endapally, S., Infante, R. E., & Radhakrishnan, A. (2019). Monitoring and Modulating Intracellular Cholesterol Trafficking Using ALOD4, a Cholesterol-Binding Protein. *Methods in molecular biology*, *1949*, 153–163.

Ernst, R., Ejsing, C. S., & Antonny, B. (2016). Homeoviscous Adaptation and the Regulation of Membrane Lipids. *Journal of molecular biology*, *428*(24 Pt A), 4776–4791.

Fink, J., & Seibel, J. (2018). Click reactions with functional sphingolipids. *Biological chemistry*, *399*(10), 1157–1168.

Fukasawa, M., Nishijima, M., Itabe, H., Takano, T., & Hanada, K. (2000). Reduction of sphingomyelin level without accumulation of ceramide in Chinese hamster ovary cells affects detergent-resistant membrane domains and enhances cellular cholesterol efflux to methyl-beta -cyclodextrin. *The Journal of biological chemistry*, *275*(44), 34028–34034.

Garbes, L., Kim, K., Rieß, A., Hoyer-Kuhn, H., Beleggia, F., Bevot, A., Kim, M. J., Huh, Y. H., Kweon, H. S., Savarirayan, R., Amor, D., Kakadia, P. M., Lindig, T., Kagan, K. O., Becker, J., Boyadjiev, S. A., Wollnik, B., Semler, O., Bohlander, S. K., Kim, J., … Netzer, C. (2015). Mutations in SEC24D, encoding a component of the COPII machinery, cause a syndromic form of osteogenesis imperfecta. *American journal of human genetics*, *96*(3), 432–439.

Ghanbarpour, A., Valverde, D. P., Melia, T. J., & Reinisch, K. M. (2021). A model for a partnership of lipid transfer proteins and scramblases in membrane expansion and organelle biogenesis. *PNAS*, *118*(16), e2101562118.

Gómez-Muñoz, A., Kong, J. Y., Salh, B., & Steinbrecher, U. P. (2004). Ceramide-1-phosphate blocks apoptosis through inhibition of acid sphingomyelinase in macrophages. *Journal of lipid research*, *45*(1), 99–105.

Granado, M. H., Gangoiti, P., Ouro, A., Arana, L., & Gómez-Muñoz, A. (2009). Ceramide 1-phosphate inhibits serine palmitoyltransferase and blocks apoptosis in alveolar macrophages. *Biochimica et biophysica acta*, *1791*(4), 263–272.

Guillemyn, B., Nampoothiri, S., Syx, D., Malfait, F., & Symoens, S. (2021). Loss of TANGO1 Leads to Absence of Bone Mineralization. *JBMR plus*, *5*(3), e10451.

Gutiérrez-Aguirre, I., Barlic, A., Podlesek, Z., Macek, P., Anderluh, G., & González-Mañas, J. M. (2004). Membrane insertion of the N-terminal alpha-helix of equinatoxin II, a sea anemone cytolytic toxin. *The Biochemical journal*, *384*(Pt 2), 421–428.

Habeck, M., Kapri-Pardes, E., Sharon, M., & Karlish, S. J. (2017). Specific phospholipid binding to Na,K-ATPase at two distinct sites. *PNAS*, *114*(11), 2904–2909.

Han, X., & Gross, R. W. (2003). Global analyses of cellular lipidomes directly from crude extracts of biological samples by ESI mass spectrometry: a bridge to lipidomics. *Journal of lipid research*, *44*(6), 1071–1079.

Han, X., & Gross, R. W. (2005). Shotgun lipidomics: multidimensional MS analysis of cellular lipidomes. *Expert review of proteomics*, *2*(2), 253–264.

Hanada, K., Kumagai, K., Yasuda, S., Miura, Y., Kawano, M., Fukasawa, M., & Nishijima, M. (2003). Molecular machinery for non-vesicular trafficking of ceramide. *Nature*, *426*(6968), 803–809.

Hannun, Y. A., & Obeid, L. M. (2008). Principles of bioactive lipid signalling: lessons from sphingolipids. *Nature reviews. Molecular cell biology*, *9*(2), 139–150.

Hannun, Y. A., & Obeid, L. M. (2018). Sphingolipids and their metabolism in physiology and disease. *Nature reviews. Molecular cell biology*, *19*(3), 175–191.

Harayama, T., & Riezman, H. (2018). Understanding the diversity of membrane lipid composition. *Nature reviews. Molecular cell biology*, *19*(5), 281–296.

Heuck, A. P., Savva, C. G., Holzenburg, A., & Johnson, A. E. (2007). Conformational changes that effect oligomerization and initiate pore formation are triggered throughout perfringolysin O upon binding to cholesterol. *The Journal of biological chemistry*, *282*(31), 22629–22637.

Holthuis, J. C., & Menon, A. K. (2014). Lipid landscapes and pipelines in membrane homeostasis. *Nature*, *510*(7503), 48–57.

Hornig-Do, H. T., Günther, G., Bust, M., Lehnartz, P., Bosio, A., & Wiesner, R. J. (2009). Isolation of functional pure mitochondria by superparamagnetic microbeads. *Analytical biochemistry*, *389*(1), 1–5.

Hotze, E. M., Wilson-Kubalek, E., Farrand, A. J., Bentsen, L., Parker, M. W., Johnson, A. E., & Tweten, R. K. (2012). Monomer-monomer interactions propagate structural transitions necessary for pore formation by the cholesterol-dependent cytolysins. *The Journal of biological chemistry*, *287*(29), 24534–24543.

Huang, D., Xu, B., Liu, L., Wu, L., Zhu, Y., Ghanbarpour, A., Wang, Y., Chen, F. J., Lyu, J., Hu, Y., Kang, Y., Zhou, W., Wang, X., Ding, W., Li, X., Jiang, Z., Chen, J., Zhang, X., Zhou, H., Li, J. Z., … Chen, X. W. (2021). TMEM41B acts as an ER scramblase required for lipoprotein biogenesis and lipid homeostasis. *Cell metabolism*, *33*(8), 1655–1670.e8.

Huang, J., & Feigenson, G. W. (1999). A microscopic interaction model of maximum solubility of cholesterol in lipid bilayers. *Biophysical journal*, *76*(4), 2142–2157.

Huitema, K., van den Dikkenberg, J., Brouwers, J. F., & Holthuis, J. C. (2004). Identification of a family of animal sphingomyelin synthases. *The EMBO journal*, *23*(1), 33–44.

Ikonen E. (2008). Cellular cholesterol trafficking and compartmentalization. *Nature reviews. Molecular cell biology*, *9*(2), 125–138.

Ishitsuka, R., Saito, T., Osada, H., Ohno-Iwashita, Y., & Kobayashi, T. (2011). Fluorescence image screening for chemical compounds modifying cholesterol metabolism and distribution. *Journal of lipid research*, *52*(11), 2084–2094.

Ishitsuka, R., Yamaji-Hasegawa, A., Makino, A., Hirabayashi, Y., & Kobayashi, T. (2004). A lipid-specific toxin reveals heterogeneity of sphingomyelin-containing membranes. *Biophysical journal*, *86*(1 Pt 1), 296–307.

Izquierdo, E., & Delgado, A. (2018). Click chemistry in sphingolipid research. *Chemistry and physics of lipids*, *215*, 71–83.

Jain, A., Beutel, O., Ebell, K., Korneev, S., & Holthuis, J. C. (2017). Diverting CERT-mediated ceramide transport to mitochondria triggers Bax-dependent apoptosis. *Journal of cell science*, *130*(2), 360–371.

Johnson, B. B., & Heuck, A. P. (2014). Perfringolysin O structure and mechanism of pore formation as a paradigm for cholesterol-dependent cytolysins. *Sub-cellular biochemistry*, *80*, 63–81.

Khavandgar, Z., & Murshed, M. (2015). Sphingolipid metabolism and its role in the skeletal tissues. *Cellular and molecular life sciences: CMLS*, *72*(5), 959–969.

Kim, Y. J., Greimel, P., & Hirabayashi, Y. (2018). GPRC5B-Mediated Sphingomyelin Synthase 2 Phosphorylation Plays a Critical Role in Insulin Resistance. *iScience*, *8*, 250–266.

Kinoshita, M., Goretta, S., Tsuchikawa, H., Matsumori, N., & Murata, M. (2013). Characterization of the ordered phase formed by sphingomyelin analogues and cholesterol binary mixtures. *Biophysics, 13*(9), 37–49.

Kinoshita, M., Suzuki, K. G., Matsumori, N., Takada, M., Ano, H., Morigaki, K., Abe, M., Makino, A., Kobayashi, T., Hirosawa, K. M., Fujiwara, T. K., Kusumi, A., & Murata, M. (2017). Raft-based sphingomyelin interactions revealed by new fluorescent sphingomyelin analogs. *The Journal of cell biology*, *216*(4), 1183–1204.

Kishimoto, T., Ishitsuka, R., & Kobayashi, T. (2016). Detectors for evaluating the cellular landscape of sphingomyelin- and cholesterol-rich membrane domains. *Biochimica et biophysica acta*, *1861*(8 Pt B), 812–829.

Kiyokawa, E., Baba, T., Otsuka, N., Makino, A., Ohno, S., & Kobayashi, T. (2005). Spatial and functional heterogeneity of sphingolipid-rich membrane domains. *The Journal of biological chemistry*, *280*(25), 24072–24084.

Klose, C., Surma, M. A., Gerl, M. J., Meyenhofer, F., Shevchenko, A., & Simons, K. (2012). Flexibility of a eukaryotic lipidome--insights from yeast lipidomics. *PloS one*, *7*(4), e35063.

Kobayashi T., Tomishige N., Inaba T., Makino A., Murata M., Yamaji-Hasegawa A., Murate M. (2021). Impact of Intrinsic and Extrinsic Factors on Cellular Sphingomyelin Imaging with Specific Reporter Proteins. *SAGE Journal 4*:1-13.

Koponen, A., Pan, G., Kivelä, A. M., Ralko, A., Taskinen, J. H., Arora, A., Kosonen, R., Kari, O. K., Ndika, J., Ikonen, E., Cho, W., Yan, D., & Olkkonen, V. M. (2020). ORP2, a cholesterol transporter, regulates angiogenic signaling in endothelial cells. *FASEB journal*, *34*(11), 14671–14694.

Kristan, K., Podlesek, Z., Hojnik, V., Gutiérrez-Aguirre, I., Guncar, G., Turk, D., González-Mañas, J. M., Lakey, J. H., Macek, P., & Anderluh, G. (2004). Pore formation by equinatoxin, a eukaryotic pore-forming toxin, requires a flexible N-terminal region and a stable beta-sandwich. *The Journal of biological chemistry*, *279*(45), 46509–46517.

Krogh, A., Larsson, B., von Heijne, G., & Sonnhammer, E. L. (2001). Predicting transmembrane protein topology with a hidden Markov model: application to complete genomes. *Journal of molecular biology*, *305*(3), 567–580.

Lamour, N. F., Subramanian, P., Wijesinghe, D. S., Stahelin, R. V., Bonventre, J. V., & Chalfant, C. E. (2009). Ceramide 1-phosphate is required for the translocation of group IVA cytosolic phospholipase A2 and prostaglandin synthesis. *The Journal of biological chemistry*, *284*(39), 26897–26907.

Lenoir, M., Coskun, U., Grzybek, M., Cao, X., Buschhorn, S. B., James, J., Simons, K., & Overduin, M. (2010). Structural basis of wedging the Golgi membrane by FAPP pleckstrin homology domains. *EMBO reports*, *11*(4), 279–284.

Levental, K. R., Malmberg, E., Symons, J. L., Fan, Y. Y., Chapkin, R. S., Ernst, R., & Levental, I. (2020). Lipidomic and biophysical homeostasis of mammalian membranes counteracts dietary lipid perturbations to maintain cellular fitness. *Nature communications*, *11*(1), 1339.

Leventis, P. A., & Grinstein, S. (2010). The distribution and function of phosphatidylserine in cellular membranes. *Annual review of biophysics*, *39*, 407–427.

Li, Z., Zhang, H., Liu, J., Liang, C. P., Li, Y., Li, Y., Teitelman, G., Beyer, T., Bui, H. H., Peake, D. A., Zhang, Y., Sanders, P. E., Kuo, M. S., Park, T. S., Cao, G., & Jiang, X. C. (2011). Reducing plasma membrane sphingomyelin increases insulin sensitivity. *Molecular and cellular biology*, *31*(20), 4205–4218.

Liu, S. L., Sheng, R., Jung, J. H., Wang, L., Stec, E., O'Connor, M. J., Song, S., Bikkavilli, R. K., Winn, R. A., Lee, D., Baek, K., Ueda, K., Levitan, I., Kim, K. P., & Cho, W. (2017). Orthogonal lipid sensors identify transbilayer asymmetry of plasma membrane cholesterol. *Nature chemical biology*, *13*(3), 268–274.

Lorent, J. H., Levental, K. R., Ganesan, L., Rivera-Longsworth, G., Sezgin, E., Doktorova, M., Lyman, E., & Levental, I. (2020). Plasma membranes are asymmetric in lipid unsaturation, packing and protein shape. *Nature chemical biology*, *16*(6), 644–652.

Lu, C. L., Ortmeier, S., Brudvig, J., Moretti, T., Cain, J., Boyadjiev, S. A., Weimer, J. M., & Kim, J. (2022). Collagen has a unique SEC24 preference for efficient export from the endoplasmic reticulum. *Traffic (Copenhagen, Denmark)*, *23*(1), 81–93.

Ma, Y., Zhang, L., & Huang, X. (2014). Genome modification by CRISPR/Cas9. *The FEBS journal*, *281*(23), 5186–5193.

Maekawa M. (2017). Domain 4 (D4) of Perfringolysin O to Visualize Cholesterol in Cellular Membranes-The Update. *Sensors (Basel, Switzerland)*, *17*(3), 504.

Maekawa, M., & Fairn, G. D. (2015). Complementary probes reveal that phosphatidylserine is required for the proper transbilayer distribution of cholesterol. *Journal of cell science*, *128*(7), 1422–1433.

Maekawa, M., Lee, M., Wei, K., Ridgway, N. D., & Fairn, G. D. (2016). Staurosporines decrease ORMDL proteins and enhance sphingomyelin synthesis resulting in depletion of plasmalemmal phosphatidylserine. *Scientific reports*, *6*, 35762.

Magalhaes, M. A., & Glogauer, M. (2010). Pivotal Advance: Phospholipids determine net membrane surface charge resulting in differential localization of active Rac1 and Rac2. *Journal of leukocyte biology*, *87*(4), 545–555.

Magdeleine, M., Gautier, R., Gounon, P., Barelli, H., Vanni, S., & Antonny, B. (2016). A filter at the entrance of the Golgi that selects vesicles according to size and bulk lipid composition. *eLife*, *5*, e16988.

Makino, A., Abe, M., Murate, M., Inaba, T., Yilmaz, N., Hullin-Matsuda, F., Kishimoto, T., Schieber, N. L., Taguchi, T., Arai, H., Anderluh, G., Parton, R. G., & Kobayashi, T. (2015). Visualization of the heterogeneous membrane distribution of sphingomyelin associated with cytokinesis, cell polarity, and sphingolipidosis. *FASEB journal, 29*(2), 477–493.

Mäkitie, R. E., Blouin, S., Välimäki, V. V., Pihlström, S., Määttä, K., Pekkinen, M., Fratzl-Zelman, N., Mäkitie, O., & Hartmann, M. A. (2021). Abnormal bone tissue organization and osteocyte lacunocanalicular network in early-onset osteoporosis due to SGMS2 mutations. *JBMR plus*, *5*(11), e10537.

Marien, E., Meister, M., Muley, T., Gomez Del Pulgar, T., Derua, R., Spraggins, J. M., Van de Plas, R., Vanderhoydonc, F., Machiels, J., Binda, M. M., Dehairs, J., Willette-Brown, J., Hu, Y., Dienemann, H., Thomas, M., Schnabel, P. A., Caprioli, R. M., Lacal, J. C., Waelkens, E., & Swinnen, J. V. (2016). Phospholipid profiling identifies acyl chain elongation as a ubiquitous trait and potential target for the treatment of lung squamous cell carcinoma. *Oncotarget*, *7*(11), 12582–12597.

Menck, K., Sönmezer, C., Worst, T. S., Schulz, M., Dihazi, G. H., Streit, F., Erdmann, G., Kling, S., Boutros, M., Binder, C., & Gross, J. C. (2017). Neutral sphingomyelinases control extracellular vesicles budding from the plasma membrane. Journal of extracellular vesicles, 6(1), 1378056.

Mesmin B, Bigay J, Moser von Filseck J, Lacas-Gervais S, Drin G, Antonny B. (2013). A four-step cycle driven by PI(4)P hydrolysis directs sterol/PI(4)P exchange by the ER-Golgi tether OSBP. *Cell*, 155(4):830-843.

Mesmin, B., Bigay, J., Polidori, J., Jamecna, D., Lacas-Gervais, S., & Antonny, B. (2017). Sterol transfer, PI4P consumption, and control of membrane lipid order by endogenous OSBP. *The EMBO journal*, *36*(21), 3156–3174.

Meyer zu Heringdorf, D., & Jakobs, K. H. (2007). Lysophospholipid receptors: signalling, pharmacology and regulation by lysophospholipid metabolism. *Biochimica et biophysica acta*, *1768*(4), 923–940.

Mitsutake, S., Zama, K., Yokota, H., Yoshida, T., Tanaka, M., Mitsui, M., Ikawa, M., Okabe, M., Tanaka, Y., Yamashita, T., Takemoto, H., Okazaki, T., Watanabe, K., & Igarashi, Y. (2011). Dynamic modification of sphingomyelin in lipid microdomains controls development of obesity, fatty liver, and type 2 diabetes. *The Journal of biological chemistry*, *286*(32), 28544–28555.

Moser von Filseck, J., Čopič, A., Delfosse, V., Vanni, S., Jackson, C. L., Bourguet, W., & Drin, G. (2015). Phosphatidylserine transport by ORP/Osh proteins is driven by phosphatidylinositol 4-phosphate. *Science, 349*(6246), 432–436.

Munro S. (1995). An investigation of the role of transmembrane domains in Golgi protein retention. *The EMBO journal*, *14*(19), 4695–4704.

Murakami, C., & Sakane, F. (2021). Sphingomyelin synthase-related protein generates diacylglycerol via the hydrolysis of glycerophospholipids in the absence of ceramide. *The Journal of biological chemistry*, *296*, 100454.

Murate, M., Abe, M., Kasahara, K., Iwabuchi, K., Umeda, M., & Kobayashi, T. (2015). Transbilayer distribution of lipids at nano scale. *Journal of cell science*, *128*(8), 1627–1638.

Murshed M. (2018). Mechanism of Bone Mineralization. *Cold Spring Harbor perspectives in medicine*, *8*(12), a031229.

Newton, A.C., & Keranen, L. M. (1994). Phosphatidyl-L-serine is necessary for protein kinase C's high-affinity interaction with diacylglycerol-containing membranes. *Biochemistry*, *33*(21), 6651-6658.

Niekamp P., Scharte F., Sokoya T., Vittadello L., Kim Y., Deng Y., Suedhoff E., Hilderink A., Imlau M., Clarke C., Hensel M., Burd C., and Holthuis J. (2022). Ca^{2+}-activated sphingomyelin scrambling and turnover mediate ESCRT-independent lysosomal repair. *Nature communications (in press).*

Nielsen, I. Ø., Groth-Pedersen, L., Dicroce-Giacobini, J., Jonassen, A., Mortensen, M., Bilgin, M., Schmiegelow, K., Jäättelä, M., & Maeda, K. (2020). Cationic amphiphilic drugs induce elevation in lysoglycerophospholipid levels and cell death in leukemia cells. *Metabolomics : Official journal of the Metabolomic Society*, *16*(9), 91.

Nielsen, I.Ø., Vidas Olsen, A., Dicroce-Giacobini, J., Papaleo, E., Andersen, K.K., Jäättelä, M., Maeda, K., and Bilgin, M. (2020). Comprehensive Evaluation of a Quantitative Shotgun Lipidomics Platform for Mammalian Sample Analysis on a High-Resolution Mass Spectrometer. J. Am. Soc. Mass Spectrom. *31*, 894–907.

Niko, Y., & Klymchenko, A. S. (2021). Emerging solvatochromic push-pull dyes for monitoring the lipid order of biomembranes in live cells. *Journal of biochemistry*, *170*(2), 163–174.

Nilsson, I., Ohvo-Rekilä, H., Slotte, J. P., Johnson, A. E., & von Heijne, G. (2001). Inhibition of protein translocation across the endoplasmic reticulum membrane by sterols. *The Journal of biological chemistry*, *276*(45), 41748–41754.

Olzmann, J. A., & Carvalho, P. (2019). Dynamics and functions of lipid droplets. *Nature reviews. Molecular cell biology*, *20*(3), 137–155.

Panatala, R., Hennrich, H., & Holthuis, J. C. (2015). Inner workings and biological impact of phospholipid flippases. *Journal of cell science*, *128*(11), 2021–2032.

Paradies, G., Paradies, V., Ruggiero, F. M., & Petrosillo, G. (2019). Role of Cardiolipin in Mitochondrial Function and Dynamics in Health and Disease: Molecular and Pharmacological Aspects. *Cells*, *8*(7), 728.

Pekkinen, M., Terhal, P. A., Botto, L. D., Henning, P., Mäkitie, R. E., Roschger, P., Jain, A., Kol, M., Kjellberg, M. A., Paschalis, E. P., van Gassen, K., Murray, M., Bayrak-Toydemir, P., Magnusson, M. K., Jans, J., Kausar, M., Carey, J. C., Somerharju, P., Lerner, U. H., Olkkonen, V. M., Klaushofer K., Holthuis J.C., Makitie, O. (2019). Osteoporosis and skeletal dysplasia caused by pathogenic variants in SGMS2. *JCI insight*, *4*(7), e126180.

Péresse, T., Kovacs, D., Subra, M., Bigay, J., Tsai, M. C., Polidori, J., Gautier, R., Desrat, S., Fleuriot, L., Debayle, D., Litaudon, M., Pham, V. C., Bignon, J., Antonny, B., Roussi, F., & Mesmin, B. (2020). Molecular and cellular dissection of the oxysterol-binding protein cycle through a fluorescent inhibitor. *The Journal of biological chemistry*, *295*(13), 4277–4288.

Pomorski, T.G., and Menon. A.K. (2016). Lipid somersaults: Uncovering the mechanisms of protein-mediated lipid flipping. *Prog. Lipid Res.* 64:69–84.

Presa, N., Gomez-Larrauri, A., Dominguez-Herrera, A., Trueba, M., & Gomez-Muñoz, A. (2020). Novel signaling aspects of ceramide 1-phosphate. *Biochimica et biophysica acta. Molecular and cell biology of lipids*, *1865*(4), 158630.

Quiroga, R., Trenchi, A., González Montoro, A., Valdez Taubas, J., & Maccioni, H. J. (2013). Short transmembrane domains with high-volume exoplasmic halves determine retention of Type II membrane proteins in the Golgi complex. *Journal of cell science*, *126*(Pt 23), 5344–5349.
Quinville, B. M., Deschenes, N. M., Ryckman, A. E., & Walia, J. S. (2021). A Comprehensive Review: Sphingolipid Metabolism and Implications of Disruption in Sphingolipid Homeostasis. *International journal of molecular sciences*, *22*(11), 5793.

Radanović, T., Reinhard, J., Ballweg, S., Pesek, K., & Ernst, R. (2018). An Emerging Group of Membrane Property Sensors Controls the Physical State of Organellar Membranes to Maintain Their Identity. *BioEssays : news and reviews in molecular, cellular and developmental biology*, *40*(5), e1700250.

Ramachandran, R., Heuck, A. P., Tweten, R. K., & Johnson, A. E. (2002). Structural insights into the membrane-anchoring mechanism of a cholesterol-dependent cytolysin. *Nature structural biology*, *9*(11), 823–827.

Reaves, B., & Banting, G. (1992). Perturbation of the morphology of the trans-Golgi network following Brefeldin A treatment: redistribution of a TGN-specific integral membrane protein, TGN38. *The Journal of cell biology*, *116*(1), 85–94.

Renne, M. F., & de Kroon, A. (2018). The role of phospholipid molecular species in determining the physical properties of yeast membranes. *FEBS letters*, *592*(8), 1330–1345.

Rogasevskaia, T., & Coorssen, J. R. (2006). Sphingomyelin-enriched microdomains define the efficiency of native Ca(2+)-triggered membrane fusion. *Journal of cell science*, *119*(Pt 13), 2688–2694.

Rojko, N., Kristan, K. Č., Viero, G., Žerovnik, E., Maček, P., Dalla Serra, M., & Anderluh, G. (2013). Membrane damage by an α-helical pore-forming protein, Equinatoxin II, proceeds through a succession of ordered steps. *The Journal of biological chemistry*, *288*(33), 23704–23715.

Rosen, H., Stevens, R. C., Hanson, M., Roberts, E., & Oldstone, M. B. (2013). Sphingosine-1-phosphate and its receptors: structure, signaling, and influence. *Annual review of biochemistry*, *82*, 637–662.

Rossjohn, J., Feil, S. C., McKinstry, W. J., Tweten, R. K., & Parker, M. W. (1997). Structure of a cholesterol-binding, thiol-activated cytolysin and a model of its membrane form. *Cell*, *89*(5), 685–692.

Roux, A., Cuvelier, D., Nassoy, P., Prost, J., Bassereau, P., & Goud, B. (2005). Role of curvature and phase transition in lipid sorting and fission of membrane tubules. *The EMBO journal*, *24*(8), 1537–1545.

Sato, T. K., Tweten, R. K., & Johnson, A. E. (2013). Disulfide-bond scanning reveals assembly state and β-strand tilt angle of the PFO β-barrel. *Nature chemical biology*, *9*(6), 383–389.

Schön, P., García-Sáez, A. J., Malovrh, P., Bacia, K., Anderluh, G., & Schwille, P. (2008). Equinatoxin II permeabilizing activity depends on the presence of sphingomyelin and lipid phase coexistence. *Biophysical journal*, *95*(2), 691–698.

Sharpe, H. J., Stevens, T. J., & Munro, S. (2010). A comprehensive comparison of transmembrane domains reveals organelle-specific properties. *Cell*, *142*(1), 158–169.

Shevchenko, A., & Simons, K. (2010). Lipidomics: coming to grips with lipid diversity. *Nature reviews. Molecular cell biology*, *11*(8), 593–598.

Slotte J. P. (2013). Molecular properties of various structurally defined sphingomyelins -- correlation of structure with function. *Progress in lipid research*, *52*(2), 206–219.

Slotte J. P. (2016). The importance of hydrogen bonding in sphingomyelin's membrane interactions with co-lipids. *Biochimica et biophysica acta*, *1858*(2), 304–310.

Spandl, J., White, D. J., Peychl, J., & Thiele, C. (2009). Live cell multicolor imaging of lipid droplets with a new dye, LD540. *Traffic 10*(11), 1579–1584.

Stephens D. J. (2012). Cell biology: Collagen secretion explained. *Nature*, *482*(7386), 474–475.

Sugimoto, M., Shimizu, Y., Zhao, S., Ukon, N., Nishijima, K., Wakabayashi, M., Yoshioka, T., Higashino, K., Numata, Y., Okuda, T., Tamaki, N., Hanamatsu, H., Igarashi, Y., & Kuge, Y. (2016). Characterization of the role of sphingomyelin synthase 2 in glucose metabolism in whole-body and peripheral tissues in mice. *Biochimica et biophysica acta*, *1861*(8 Pt A), 688–702.

Suzuki, J., Denning, D. P., Imanishi, E., Horvitz, H. R., & Nagata, S. (2013). Xk-related protein 8 and CED-8 promote phosphatidylserine exposure in apoptotic cells. *Science*, *341*(6144), 403–406.

Suzuki, J., Umeda, M., Sims, P. J., & Nagata, S. (2010). Calcium-dependent phospholipid scrambling by TMEM16F. *Nature*, *468*(7325), 834–838.

Tafesse, F. G., Huitema, K., Hermansson, M., van der Poel, S., van den Dikkenberg, J., Uphoff, A., Somerharju, P., & Holthuis, J. C. (2007). Both sphingomyelin synthases SMS1 and SMS2 are required for sphingomyelin homeostasis and growth in human HeLa cells. *The Journal of biological chemistry*, *282*(24), 17537–17547.

Tanaka, K., Caaveiro, J. M., Morante, K., González-Mañas, J. M., & Tsumoto, K. (2015). Structural basis for self-assembly of a cytolytic pore lined by protein and lipid. *Nature communications*, *6*, 6337.

Thouverey, C., Strzelecka-Kiliszek, A., Balcerzak, M., Buchet, R., & Pikula, S. (2009). Matrix vesicles originate from apical membrane microvilli of mineralizing osteoblast-like Saos-2 cells. *Journal of cellular biochemistry*, *106*(1), 127–138.

Vacaru, A. M., Tafesse, F. G., Ternes, P., Kondylis, V., Hermansson, M., Brouwers, J. F., Somerharju, P., Rabouille, C., & Holthuis, J. C. (2009). Sphingomyelin synthase-related protein SMSr controls ceramide homeostasis in the ER. *The Journal of cell biology*, *185*(6), 1013–1027.

van Meer, G., & de Kroon, A. I. (2011). Lipid map of the mammalian cell. *Journal of cell science*, *124*(Pt 1), 5–8.

van Meer, G., Voelker, D. R., & Feigenson, G. W. (2008). Membrane lipids: where they are and how they behave. *Nature reviews. Molecular cell biology*, *9*(2), 112–124.

Vance JE. Phospholipid synthesis and transport in mammalian cells. *Traffic*. 2015;16(1):1-18.

Venugopal, S., Martinez-Arguelles, D. B., Chebbi, S., Hullin-Matsuda, F., Kobayashi, T., & Papadopoulos, V. (2016). Plasma Membrane Origin of the Steroidogenic Pool of Cholesterol Used in Hormone-induced Acute Steroid Formation in Leydig Cells. *The Journal of biological chemistry*, *291*(50), 26109–26125.0.

Vodicka, P., Mo, S., Tousley, A., Green, K. M., Sapp, E., Iuliano, M., Sadri-Vakili, G., Shaffer, S. A., Aronin, N., DiFiglia, M., & Kegel-Gleason, K. B. (2015). Mass Spectrometry Analysis of Wild-Type and Knock-in Q140/Q140 Huntington's Disease Mouse Brains Reveals Changes in

Glycerophospholipids Including Alterations in Phosphatidic Acid and Lyso-Phosphatidic Acid. *Journal of Huntington's disease*, *4*(2), 187–201.

Wang, B., & Tontonoz, P. (2019). Phospholipid Remodeling in Physiology and Disease. *Annual review of physiology*, *81*, 165–188.

Wang, Y., Hinz, S., Uckermann, O., Hönscheid, P., von Schönfels, W., Burmeister, G., Hendricks, A., Ackerman, J. M., Baretton, G. B., Hampe, J., Brosch, M., Schafmayer, C., Shevchenko, A., & Zeissig, S. (2020). Shotgun lipidomics-based characterization of the landscape of lipid metabolism in colorectal cancer. *Biochimica et biophysica acta. Molecular and cell biology of lipids*, *1865*(3), 158579.

Wenk M. R. (2010). Lipidomics: new tools and applications. *Cell*, *143*(6), 888–895.

Wong, L. H., Gatta, A. T., & Levine, T. P. (2019). Lipid transfer proteins: the lipid commute via shuttles, bridges and tubes. *Nature reviews. Molecular cell biology*, *20*(2), 85–101.

Yamaji-Hasegawa, A., Makino, A., Baba, T., Senoh, Y., Kimura-Suda, H., Sato, S. B., Terada, N., Ohno, S., Kiyokawa, E., Umeda, M., & Kobayashi, T. (2003). Oligomerization and pore formation of a sphingomyelin-specific toxin, lysenin. *The Journal of biological chemistry*, *278*(25), 22762–22770.

Yamaji, A., Sekizawa, Y., Emoto, K., Sakuraba, H., Inoue, K., Kobayashi, H., & Umeda, M. (1998). Lysenin, a novel sphingomyelin-specific binding protein. *The Journal of biological chemistry*, *273*(9), 5300–5306.

Yang, K., & Han, X. (2016). Lipidomics: Techniques, Applications, and Outcomes Related to Biomedical Sciences. *Trends in biochemical sciences*, *41*(11), 954–969.

Yano, M., Watanabe, K., Yamamoto, T., Ikeda, K., Senokuchi, T., Lu, M., Kadomatsu, T., Tsukano, H., Ikawa, M., Okabe, M., Yamaoka, S., Okazaki, T., Umehara, H., Gotoh, T., Song, W. J., Node, K., Taguchi, R., Yamagata, K., & Oike, Y. (2011). Mitochondrial dysfunction and increased reactive oxygen species impair insulin secretion in sphingomyelin synthase 1-null mice. *The Journal of biological chemistry*, *286*(5), 3992–4002.

Yano, M., Yamamoto, T., Nishimura, N., Gotoh, T., Watanabe, K., Ikeda, K., Garan, Y., Taguchi, R., Node, K., Okazaki, T., & Oike, Y. (2013). Increased oxidative stress impairs adipose tissue function in sphingomyelin synthase 1 null mice. *PloS one*, *8*(4), e61380.

Yoshikawa, Y., Yoshizawa, T., Domae, E., Hirai, Y., Kamada, A., Okazaki, T., & Ikeo, T. (2019). Knockdown of sphingomyelin synthase 2 inhibits osteoclastogenesis by decreasing RANKL expression in mouse primary osteoblasts. *Biomedical research, 40*(5), 189–196.

Yu, J., Kim, H. M., Kim, K. P., Son, Y., Kim, M. S., & Park, K. S. (2019). Ceramide kinase regulates the migration of bone marrow-derived mesenchymal stem cells. *Biochemical and biophysical research communications*, *508*(2), 361–367.

Zhang, Y., Le, T., Grabau, R., Mohseni, Z., Kim, H., Natale, D. R., Feng, L., Pan, H., & Yang, H. (2020). TMEM16F phospholipid scramblase mediates trophoblast fusion and placental development. *Science advances*, *6*(19), eaba0310.

Zhou, Y., & Hancock, J. F. (2018). Deciphering lipid codes: K-Ras as a paradigm. *Traffic, 19*(3), 157–165.

8. APPENDIX

8.1. Supplementary figures

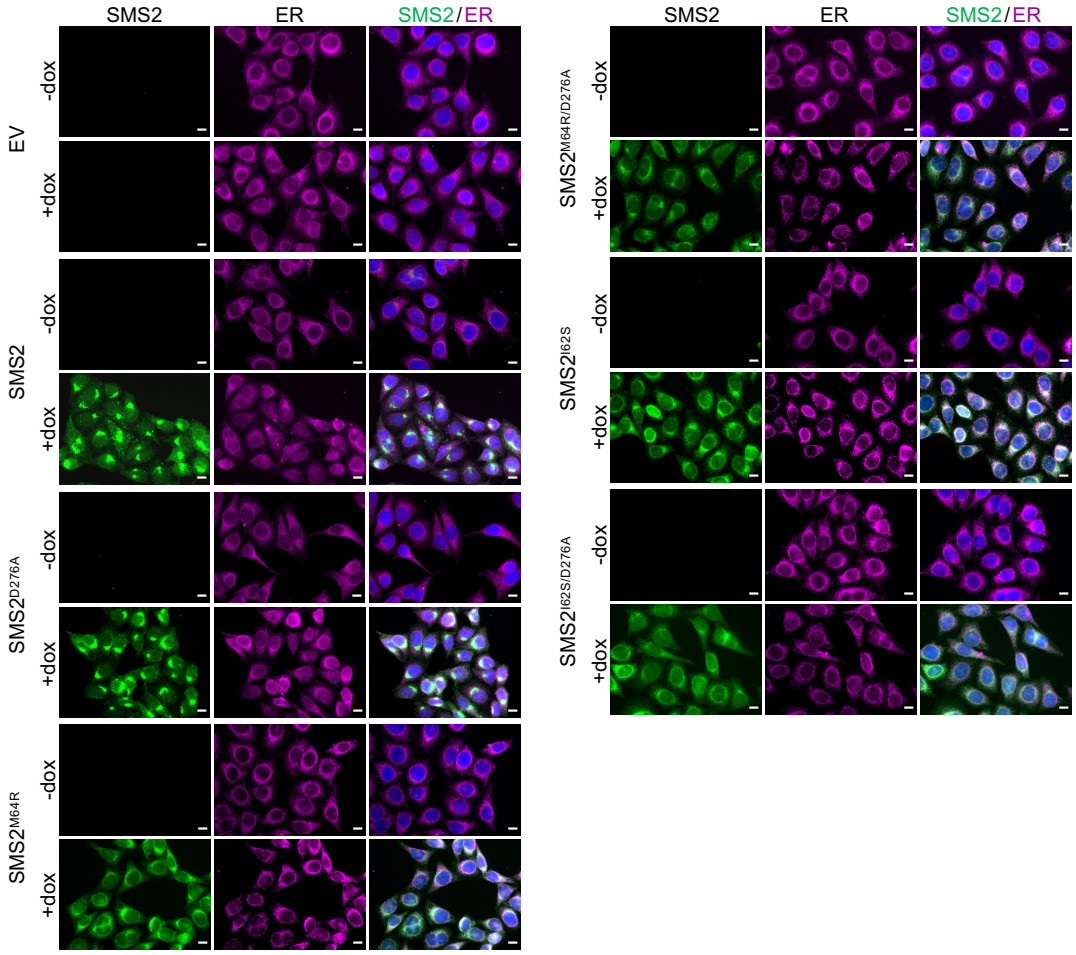

Fig. S1. Doxycycline-induced expression of SMS2 variants in stably transduced HeLa cells. HeLa ΔSMS1/2 cells stably transduced with doxycycline-inducible Flag-tagged SMS2, SMS2^{I62S}, SMS2^{M64R} or their enzyme-dead isoforms (D276A) were grown for 16 h in the absence or presence of doxycycline. Next, cells were fixed, immunostained with α-Flag (*green*) and α-calnexin (*magenta*) antibodies, counterstained with DAPI (*blue*) and imaged by Leica fluorescence microscopy. Scale bar, 10 μm.

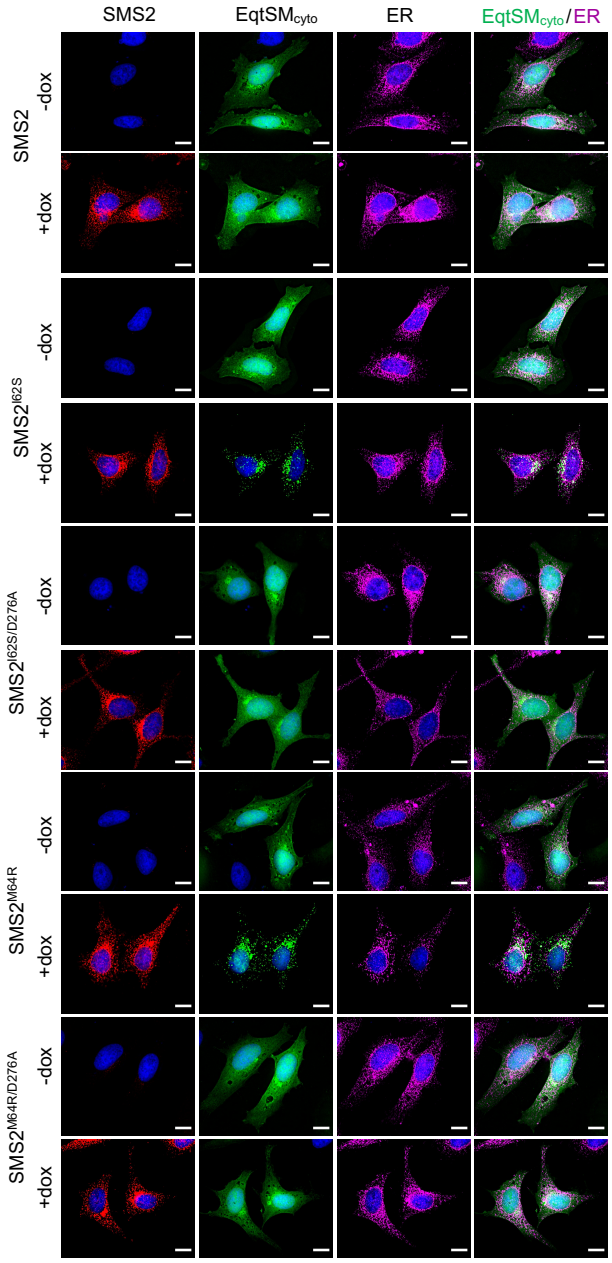

Fig. S2. Mobilization of cytosolic SM reporter EqtSM by pathogenic SMS2 variants relies on a catalytically active enzyme.
HeLa ΔSMS1/2 cells stably transduced with Flag-tagged SMS2, SMS2^{I62S}, SMS2^{M64R} or their enzyme-dead isoforms (D276A) were transfected with GFP-tagged EqtSM$_{cyto}$ (*green*) and grown for 16 h in the absence or presence of doxycycline. Next, cells were fixed, immunostained with α-Flag (SMS2, *red*) and α-calnexin (ER, *magenta*) antibodies, counterstained with DAPI (*blue*) and imaged by DeltaVision microscopy. Scale bar, 10 μm. This figure is related to figure 17.

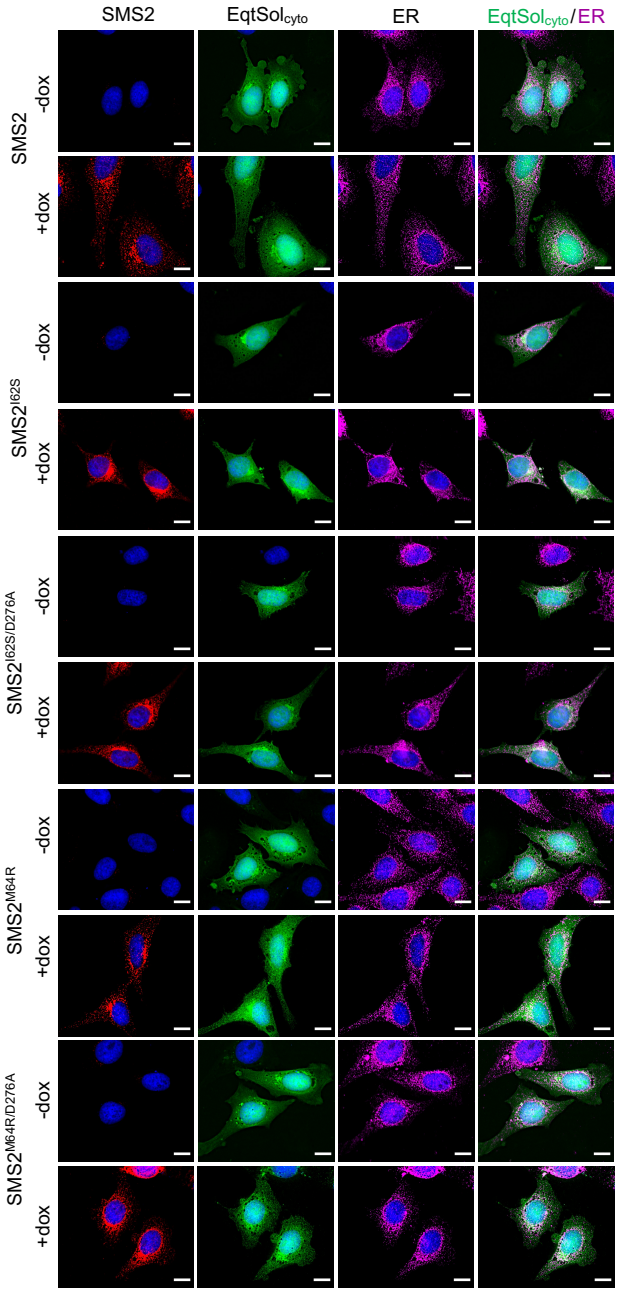

Fig. S3. Pathogenic SMS2 variants fail to mobilize SM binding-defective EqtSol.
HeLa ΔSMS1/2 cells stably transduced with Flag-tagged SMS2, SMS2^{I62S}, SMS2^{M64R} or their enzyme-dead isoforms (D276A) were transfected with GFP-tagged EqtSol$_{cyto}$ (*green*) and grown for 16 h in the absence or presence of doxycycline. Next, cells were fixed, immunostained with α-Flag (SMS2, *red*) and α-calnexin (ER, *magenta*) antibodies, counterstained with DAPI (*blue*) and imaged by DeltaVision microscopy. Scale bar, 10 μm. This figure is related to figure 17.

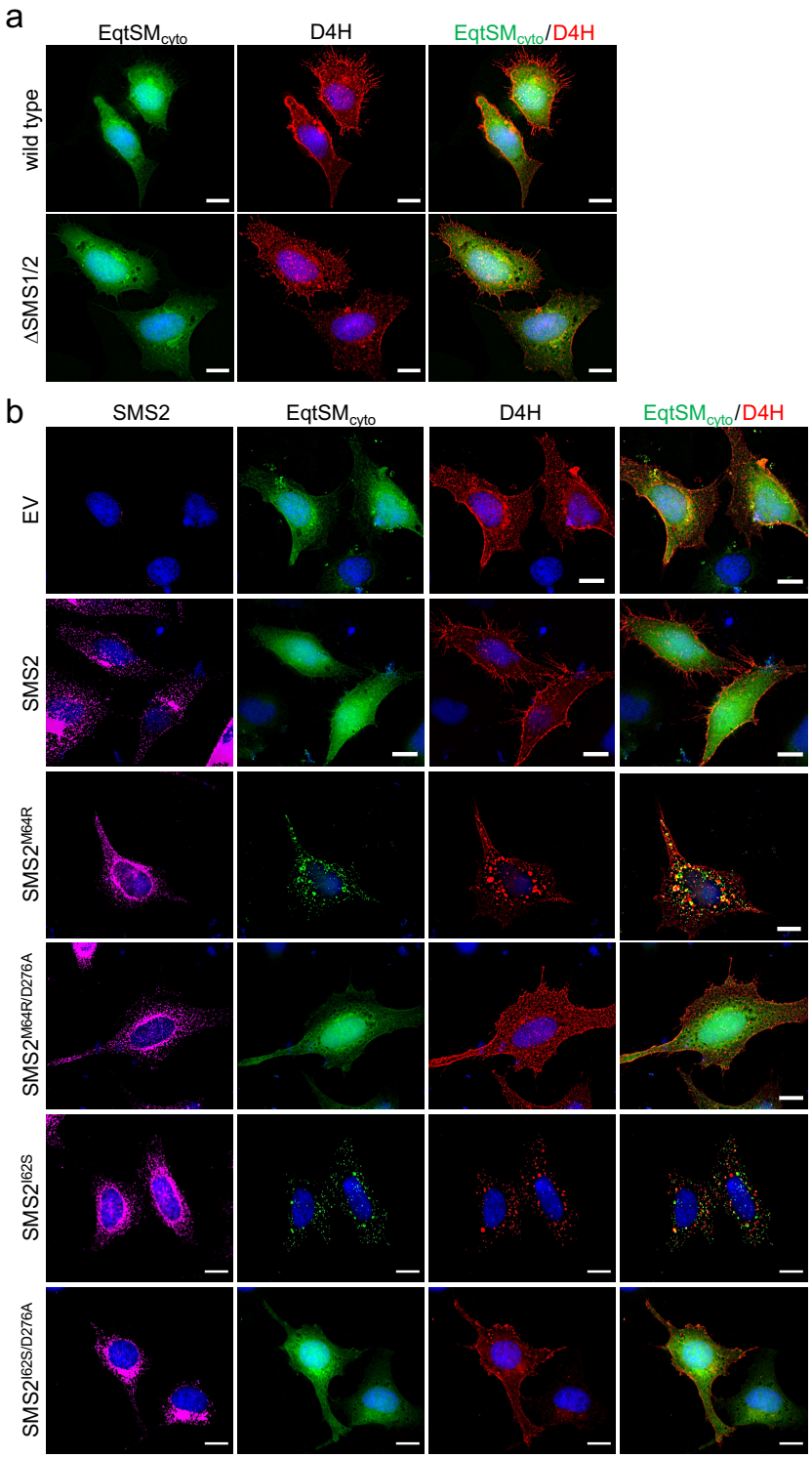

Fig. S4. Pathogenic SMS2 variants perturb subcellular cholesterol pools.
(**a**) HeLa wildtype or ΔSMS1/2 cells were co-transfected with GFP-tagged $EqtSM_{cyto}$ (*green*) and mCherry-tagged D4H (*red*). After 16 h, cells were fixed, counterstained with DAPI (*blue*) and imaged by DeltaVision microscopy. (**b**) HeLa ΔSMS1/2 cells stably transduced with Flag-tagged SMS2, $SMS2^{I62S}$, $SMS2^{M64R}$ or their enzyme-dead isoforms (D276A) were co-transfected with GFP-tagged $EqtSM_{cyto}$ (*green*) and mCherry-tagged D4H (*red*) and then grown for 16 h in the presence of doxycycline. Next, cells were fixed, immunostained with α-Flag antibody (SMS2, *magenta*), counterstained with DAPI (*blue*) and imaged by DeltaVision microscopy. Scale bars, 10 μm.

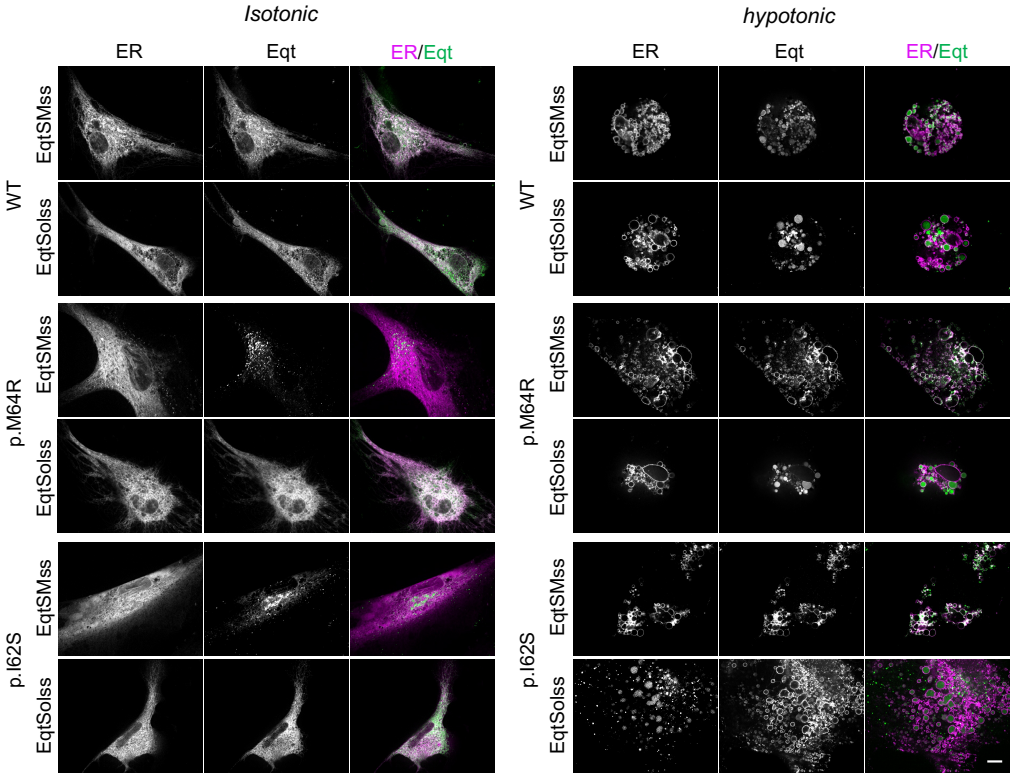

Fig. S5. Patient-derived fibroblasts display aberrant SM distribution.
Control (WT) or patient-derived human skin fibroblasts carrying heterozygous missense variants c.185T>G (p.I62S) or c.191T>G (p.M64R) in *SGMS2* were co-transfected with mCherry-tagged VAP-A (ER, *magenta*) and GFP-tagged EqtSM$_{SS}$ (*green*). Co-transfections with GFP-tagged EqtSol$_{SS}$ served as control. After 16 h, cells were incubated in hypotonic medium (1% Opti-MEM) for 5 min and imaged by spinning disc confocal microscopy. This figure is related to figure 20.

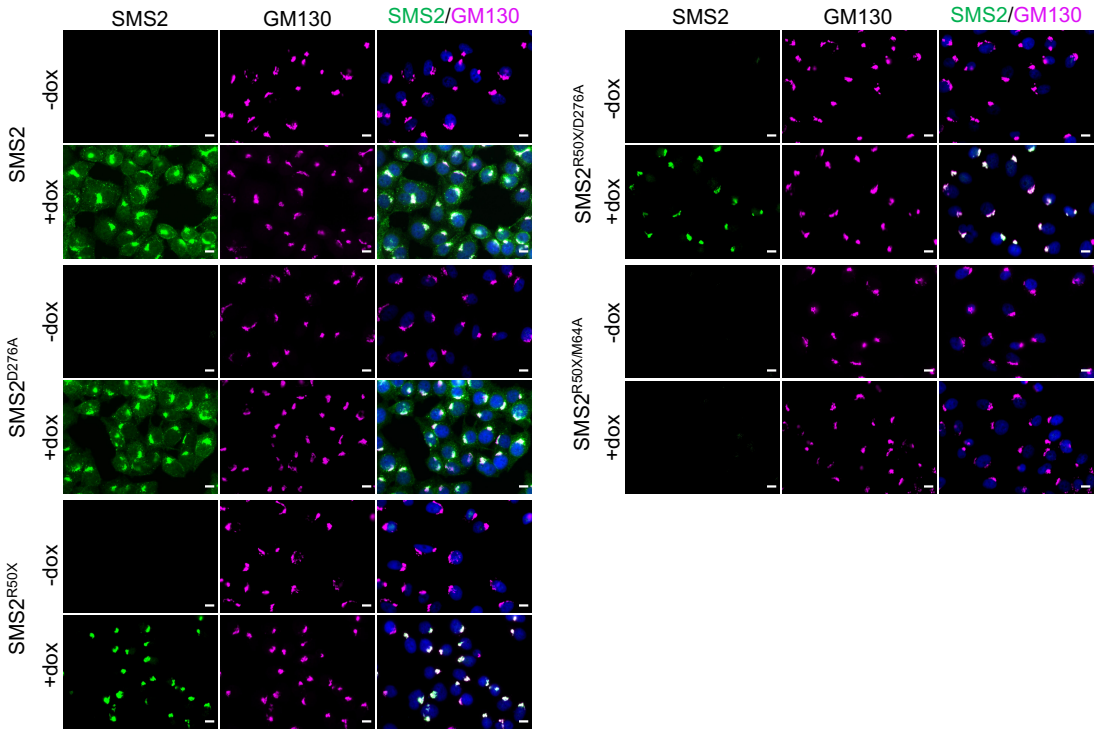

Fig. S6. Doxycycline-induced expression of HA-tagged SMS2 variants in stably transduced HeLa cells.
HeLa ΔSMS1/2 cells transduced with doxycycline-inducible N-terminal HA-tagged SMS2 or $SMS2^{R50X}$, or the enzyme dead isoforms $SMS2^{D276A}$ or $SMS2^{R50X/D276A}$, $SMS2^{M64A}$ or $SMS2^{R50X/M64A}$ were grown for 16 h in the absence or presence of doxycycline. Next, cells were fixed, immunostained with α-Flag (*green*) and α-GM130 (*magenta*) antibodies, counterstained with DAPI (*blue*) and imaged by Leica fluorescence microscopy. Scale bar, 10 μm.

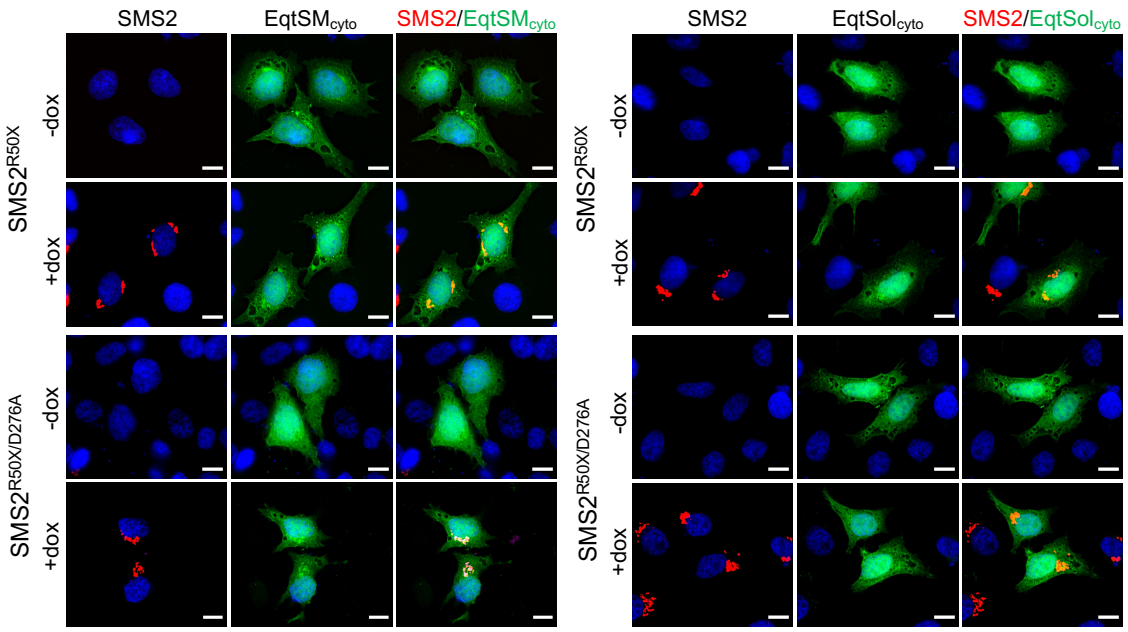

Fig. S7. Pathogenic SMS2^{R50X} does not mobilize EqtSM$_{cyto}$.
HeLa ΔSMS1/2 cells stably transduced with doxycycline-inducible HA-tagged SMS2^{R50X} or SMS2$^{R50X/D276A}$ were transfected with cytosolic GFP-tagged SM reporter EqtSM$_{cyto}$ or its SM binding-defective derivative, EqtSol$_{cyto}$ (Eqt, *green*). Next, cells were treated with doxycycline for 16 h, fixed, immunostained with α-HA antibody (*magenta*), counterstained with DAPI (*blue*) and then imaged by DeltaVision microscopy. Scale bar, 10 μm.

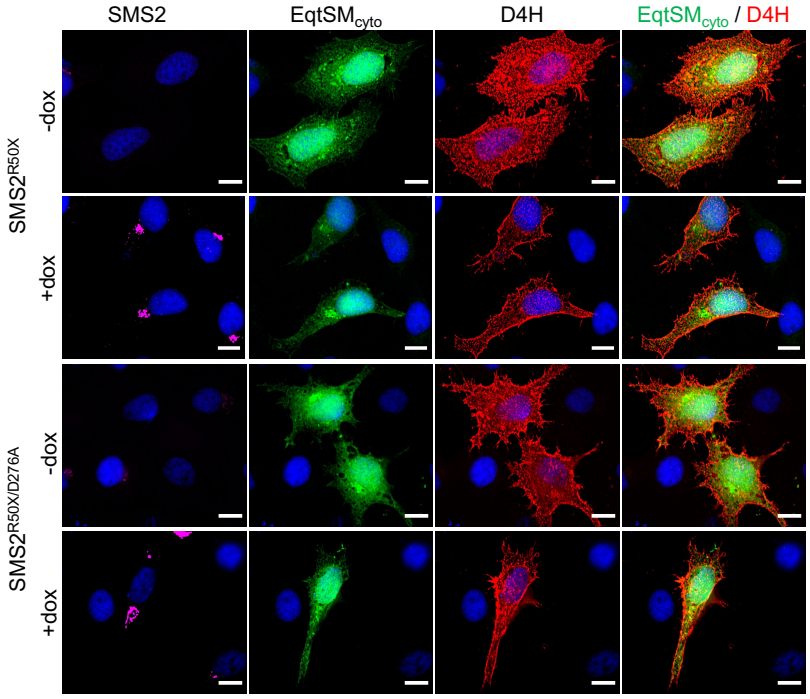

Fig. S8. Pathogenic SMS2^{R50X} does not perturb subcellular cholesterol pools.
HeLa ΔSMS1/2 cells stably transduced with doxycycline-inducible HA-tagged SMS2^{R50X} and SMS2$^{R50X/D276A}$ were co-transfected with cytosolic GFP-tagged SM reporter EqtSM$_{cyto}$ (*green*) and mCherry-tagged sterol reporter D4H (*red*). Next, cells were treated with doxycycline for 16 h, fixed, immunostained with α-HA antibody (*magenta*), counterstained with DAPI (*blue*) and then imaged by DeltaVision microscopy. Scale bar, 10 μm.

8.2. List of antibodies

Table 2. List of antibodies

Antibody	Application and dilution	Organism of origin	Supplier and product code
Primary antibodies			
β-actin	IB 1:50,000	Mouse mAb	Sigma; A1978
β-calnexin	IB 1:1,000	Rabbit pAb	Santa Cruz; sc-11397
β-calnexin	IB 1:1,000 IF 1:200	Goat pAb	Santa Cruz; sc-6495
β-calnexin	IP 1:1,000	Rabbit pAb	Abcam; ab22595
EEA1	IF 1:400	Mouse mAb	Cell Signalling; 48453
ERGIC53	IF 1:400	Mouse mAb	Novus; np62-03381
FLAG	IB 1:1,000 IF 1:400	Mouse mAb	Abcam; ab205606
GM130	IF 1:400	Mouse mAb	BD biosciences; 610823
HA	IB 1:1,000	Rabbit pAb	Invitrogen; 7155000
LAMP-1	IF 1:400	Mouse mAb	Santa Cruz; sc-20011
SMS2	IB 1:1,000	Mouse mAb	Santa Cruz; sc-293384
Mitop60	IB 1:1,000	Mouse mAb	Millipore; MAB1273
Na/K ATPase	IB 1:1,000	Mouse mAb	Santa Cruz; sc-48345
Na/K ATPase	IF 1:400	Rabbit mAb	Abcam; ab-76020
TGN46	IF 1:400	Sheep pAb	Bio-rad; AHP1586
V5	IF 1:400	Rabbit pAb	Sigma; v8137
Secondary antibodies			
Anti Mouse Cy™-5	IF 1:400		JIR; 715-175-150
Anti Rabbit Cy™-2	IF 1:400		JIR; 711-225-152
Anti Goat Cy™-5	IF 1:400		JIR; 705-175-147
Anti Goat Cy™-3	IF 1:400		JIR; 705-165-147
Anti Mouse Cy™-3	IF 1:400		JIR; 715-162-150
Anti Rabbit Cy™-5	IF 1:400		JIR; 711-175-152
Anti Sheep Dylight488	IF 1:400		Bio-rad; STAR88D488GA
Anti-Mouse-HRP	IB 1:5,000	Goat	Thermo Fischer Scientific; 31430
Anti-Rabbit-HRP	IB 1:5,000	Goat	Thermo Fischer Scientific; 31460
Anti-Goat-HRP	IB 1:5,000	Donkey	Thermo Fischer Scientific; PA1-28664

8.3. List of plasmids

Table 3. List of plasmids

Code	Name	Source
0694	pcDNA3.1(+)-FLAG-hSMS2	Pekinnen *et al.*, 2019
0695	pcDNA3.1(+)-FLAG-hSMS2(I62S)	Pekinnen *et al.*, 2019
0696	pcDNA3.1(+)-FLAG-hSMS2(M64R)	Pekinnen *et al.*, 2019
0730	pEFP-C1-Sec16L	Bhattacharyya and Glick 2007
0853	pcDNA3.1(+)-FLAG-hSMSr	J. Parolek dissertation, 2019
0855	pcDNA3.1(+)-FLAG-hSMSr-hSMS1(81-139)	J. Parolek dissertation, 2019
0875	pcDNA3.1(+)-FLAG-hSMSr-hSMS1(81-139; I124S)	J. Parolek dissertation, 2019
0876	pcDNA3.1(+)-FLAG-hSMSr-hSMS1(81-139; M126R)	J. Parolek dissertation, 2019
0877	pcDNA3.1(+)-FLAG-hSMS1ΔSAM	J. Parolek dissertation, 2019
0880	pcDNA3.1(+)-FLAG-hSMSr-hSMS1(81-139) ΔSAM	J. Parolek dissertation, 2019
0897	pcDNA3.1(+)-FLAG-hSMSr-hSMS2(11-77)	J. Parolek dissertation, 2019
0898	pcDNA3.1(+)-FLAG-hSMSr-hSMS2(11-77; I136S)	J. Parolek dissertation, 2019
0899	pcDNA3.1(+)-FLAG-hSMSr-hSMS2(11-77; M138R)	J. Parolek dissertation, 2019
0907	pENTR11	Invitrogen, A10467
0909	pINDUCER20-NEO	Addgene, 44012
0912	pMD2.G	Addgene, 12259
0913	psPAX2	Addgene, 12260
0915	pcDNA3.1(+)-FLAG-hSMS1-ΔSAM(I124S)	J. Parolek dissertation, 2019
0916	pcDNA3.1(+)-FLAG-hSMS1-ΔSAM(M126R)	J. Parolek dissertation, 2019
0917	pcDNA3.1(+)-FLAG-hSMSr-hSMS1(81-139; I124S) ΔSAM	J. Parolek dissertation, 2019
0918	pcDNA3.1(+)-FLAG-hSMSr-hSMS1(81-139; M126R) ΔSAM	J. Parolek dissertation, 2019
0930	pENTR11-FLAG-hSMS2	J. Parolek dissertation, 2019
0931	pENTR11-FLAG-hSMS2(M64R)	J. Parolek dissertation, 2019
0933	pENTR11-FLAG-hSMS2(M64R; D276A)	J. Parolek dissertation, 2019
0936	pINDUCER20-FLAG-hSMS2-Neo	J. Parolek dissertation, 2019
0937	pINDUCER20-FLAG-hSMS2(M64R)-Neo	J. Parolek dissertation, 2019
0938	pINDUCER20-FLAG-hSMS2(D276A)-Neo	J. Parolek dissertation, 2019
0939	pINDUCER20-FLAG-hSMS2(M64R; D276A	J. Parolek dissertation, 2019
0952	pENTR11-FLAG-hSMS2(I62S)	This study
0953	pENTR11-FLAG-hSMS2(I62S; D276A)	This study
0977	pINDUCER20-FLAG-hSMS2(I62S)-Neo	This study
0978	pINDUCER20-FLAG-hSMS2(I62S; D276A)-Neo	This study
1065	pENTR11-FLAG-hSMS2-HA	This study
1066	pENTR11-FLAG-hSMS2(R50X)-HA	This study
1067	pENTR11-FLAG-hSMS2(R50X; M64A)-HA	This study
1068	pENTR11-FLAG-hSMS2(M64A)-HA	This study
1069	pENTR11-FLAG-hSMS2(R50X; D276A)-HA	This study
1070	pENTR11-FLAG-hSMS2(D276A)-HA	This study
1071	pINDUCER20-FLAG-hSMS2-HA-Neo	This study

Table 3. List of plasmids (continued)

Code	Name	Source
1072	pINDUCER20-FLAG-hSMS2(D276A)-HA-Neo	This study
1073	pINDUCER20-FLAG-hSMS2(R50X)-HA-Neo	This study
1074	pINDUCER20-FLAG-hSMS2(R50X; D276A)-HA-Neo	This study
1075	pINDUCER20-FLAG-hSMS2(R50X; M64A)-HA-Neo	This study
1075	pINDUCER20-FLAG-hSMS2(M64A)-HA-Neo	This study
1053	pN1-EqtSM$_{ss}$-oxGFP	Deng *et al.*, 2016
1054	pN1-EqtSol$_{ss}$-oxGFP	Deng *et al.*, 2016
1055	pN1-EqtSM$_{cyto}$-oxGFP	This study
1056	pN1-EqtSM$_{cyto}$-oxGFP	This study
1058	D4H-mCherry	Deng *et al.*, 2016
1101	VAP-A-mCherry	Jain *et al.*, 2017
1102	EqtSM-mKate	Niekamp *et al.*, 2022
1118	pET28a-Eqt-SM-3xFLAG	Deng *et al.*, 2016

8.4. List of oligonucleotides

Table 4. List of oligonucleotides

Name	Sequence (5'-3')
SMS2(I62S)-F	CGGACTATATCCAAAGTGCTATGCCCACTGAATC
SMS2(I62S)-R	GATTCAGTGGGCATAGCACTTTGGATATAGTCCG
SMS2(M64R)-F	CTATATCCAAATTGCTAGGCCCACTGAATCAAGG
SMS2(M64R)-R	CCTTGATTCAGTGGGCCTAGCAATTTGGATATAG
SMS2(D276A)-F	CGAACACTACACTATCGCTGTGATCATTGC
SMS2(D276A)-R	GCAATGATCACAGCGATAGTGTAGTGTTCG
SMS2(R50X)-F	CTTATCCAGTGGGCTGTGAAAAGGCACC
SMS2(R50X)-R	GGTGCCTTTTCACAGCCCACTGGATAAG
SMS2(M64A)-F	ATATCCAAATTGCTGCGCCCACTGAATC
SMS2(M64A)-R	GATTCAGTGGGCGCAGCAATTTGGATAT
Addition of BamHI-FLAG to N-terminus of SMS2	CTGGATCCACCATGGATTACAAGGATGACGACGATAAGATG
Addition of HA-NotI to C-terminus of SMS2	GTCTAGATGCGGCCGCCTTACTAGGCGTAATCCGGCACATCAT AGGGGTAGGTCGATTTCTCATT

8.5. List of sgRNAs

Table 5. List of sgRNAs

Name	Sequence (5'-3')	Source
hSMS1 sgRNA 1	TGATACCACCAGAGTCGCCG	Santa Cruz (no. sc-403382)
hSMS1 sgRNA 2	TTGTACCTCGATCTTACCAT	Santa Cruz (no. sc-403382)
hSMS1 sgRNA 3	TAAGTGTTAGCATGACCGTG	Santa Cruz (no. sc-403382)
hSMS2 sgRNA 1	TAACCGTGTGACCGCTGAAG	Santa Cruz (no. sc-405416)
hSMS2 sgRNA 2	GGTCTTGCATAAGTGTTCGT	Santa Cruz (no. sc-405416)
hSMS2 sgRNA 3	GTTACTACTCTACCTGTGCC	Santa Cruz (no. sc-405416)

8.6. List of tables

8.7. List of figures

8.8. List of abbreviations

Ala	alanine
Arg	arginine
Asp	aspartate
ATP	adenosine triphosphate
BFA	brefeldin A
BSA	Bovine serum albumin
Ca^{2+}	calcium
CDL	calvarial doughnut lesion
Cer	ceramide
Cer1P	ceramide-1-phosphate
CERK	ceramide kinase
CERT	ceramide transfer protein
Chol	cholesterol
CL	cardiolipin
CoA	coenzyme A
COPI	coat protein complex I
COPII	coat protein complex II
CPE	ceramide phosphoethanolamine
CPTP	ceramide-1-phosphate transfer protein
DAG	Diacylglycerol
D4H	Domain 4 with higher affinity
ΔSMS1/2	SMS1 and SMS2 double knock out
ESCRT	Endosomal sorting complexes required for transport
Eqt	equinatoxin
ER	endoplasmic reticulum
EV	empty vector
GlcCer	glucosyl ceramide
HexCer	hexosyl ceramide
Ile	isoleucine
KO	knock out
LBPs	lipid binding proteins
LC-MS	liquid chromatography, mass spectrometry
LLOME	L-leucyl-L-leucine O-methyl ester
Met	methionine
MS	mass spectrometry
nSmase2	neutral sphingomyelinase 2
OSBP	oxysterol binding protein
PAGE	SDS-Polyacrylamide gel electrophoresis
PBS	phosphate buffered saline
PE	phosphatidylethanolamine
PS	phosphatidylserine
PC	phosphatidylcholine
PI	phosphatidylinositol
PI(4)P	phosphatidylinositol (4)-phosphate
PFO	perfingolysin O
PM	plasma membrane
Ser	serine
SM	sphingomyelin
SMS	sphingomyelin synthase
SMS1	sphingomyelin synthase 1
SMS2	sphingomyelin synthase 2
SMSr	sphingomyelin synthase related protein
TLC	thin layer chromatography
TMDs	transmembrane domains

8.9. Publications

Niekamp P., Scharte F., **Sokoya T**., Vittadello L., Kim Y., Deng Y., Suedhoff E., Hilderink A., Imlau M., Clarke C., Hensel M., Burd C., and Holthuis J. C. (2022). Ca^{2+}-activated sphingomyelin scrambling and turnover mediate ESCRT-independent lysosomal repair. *Nature communications* (in press).

Sokoya T., Parolek J., Foged M. M., Danylchuk. D., Bozan M, Sarkar B., Hilderink A., Philippi M., Botto L. D., Terhal P. A., Mäkitie O., Piehler J., Kim Y., Burd C., Klymchenko A., Maeda K., Holthuis J. C. Pathogenic variants of sphingomyelin synthase SMS2 disrupt lipid landscapes in the secretory pathway (submitted).

Sokoya T., Holthuis J. C. Pathogenic non-sense variant p.Arg50* in *SGMS2* gives rise to a functional sphingomyelin synthase that is mistargeted to the early Golgi (manuscript in preparation).

Kol M., Novak A., Morstein J., Schröer C., **Sokoya T**., Mensing S., Korneev S., Trauner D., Holthuis J. C. Optical manipulation of sphingolipid metabolism using photoswitchable sphingosines (manuscript in preparation).

8.10. Erklärung über die Eigenständigkeit der erbrachten wissenschaftlichen Leistung

Ich erkläre hiermit, dass ich die vorliegende Arbeit ohne unzulässige Hilfe Dritter und ohne Benutzung anderer als der angegebenen Hilfsmittel angefertigt habe. Die aus anderen Quellen direkt oder indirekt übernommenen Daten und Konzepte sind unter Angabe der Quelle gekennzeichnet. Bei der Auswahl und Auswertung folgenden Materials haben mir die nachstehend aufgeführten Personen in der jeweils beschriebenen Weise entgeltlich / unentgeltlich geholfen.

1. Experimente mit chimären Proteinen und Domänenaustausch von Mitgliedern der SMS-Familie wurden von Dr. Jan Parolek (Molekulare Zellbiologie, Universität Osnabrück) durchgeführt, sofern angegeben.

2. Massenspektrometrie-basierte Shotgun-Lipidomik wurde durchgeführt von Dr. Kenji Maeda und Dr. Mads Møller Foged von der Cell Death and Metabolism Group, Center for Autophagy, Recycling and Disease, Danish Cancer Society Research Center, DK-2100 Kopenhagen, Dänemark.

Weitere Personen waren an der inhaltlichen materiellen Erstellung der vorliegenden Arbeit nicht beteiligt. Insbesondere habe ich hierfür nicht die entgeltliche Hilfe von Vermittlungs- bzw. Beratungsdiensten (Promotionsberater oder andere Personen) in Anspruch genommen. Niemand hat von mir unmittelbar oder mittelbar geldwerte Leistungen für Arbeiten erhalten, die im Zusammenhang mit dem Inhalt der vorgelegten Dissertation stehen. Die Arbeit wurde bisher weder im In- noch im Ausland in gleicher oder ähnlicher Form einer anderen Prüfungsbehörde vorgelegt.

Osnabrück, den

_____

Tolulope Sokoya

ACKNOWLEDGEMENTS

As I dot the i's and cross the t's of what has been a long journey, I would like to appreciate everyone who has been instrumental in bringing this work to fruition. Firstly, I would like to express my sincere appreciation to **Prof. Joost Holthuis** for giving me the opportunity to come to Germany to do my PhD under his supervision. You have been an immense inspiration to me over the course of this program. Thank you for providing an enabling environment for my development and constantly challenging me to go over and beyond my limit. Your advice, suggestions and critical feedback at every stage has brought this work to this point. You are not just an outstanding scientist but an exemplary leader who truly cares about the development and welfare of everyone working with him. I consider it a great privilege to have worked under your tutelage. Thank you so much for everything!

I would also like to express my deepest appreciation to **Prof. Jacob Piehler**, **Prof Achim Paululat**, and **Dr Florian Fröhlich** for valuable comments regarding this work and for accepting to be my examiners.

Many thanks to **Dr Stefan Walter** and **Dr Rainer Kurre** for help with mass spectrometry and light microscopy respectively. I am very grateful to **Dr Matthijs Kol** whom I have learnt a lot from. Thank you for your invaluable suggestions and expertise that has helped to shape this work. Many thanks to **Dr Sergei Korneev** for providing expertise in lipid synthesis and to **Dr Markus Schneider** for help with everything software. I would like to thank former lab technician, **Dagmar Müller** for creating a pleasant working atmosphere in the lab, and for showing me around Osnabrueck and its environs. Also, to **Angelika Hilderink** and **Britta Fiedler** for providing me with technical support and, **Sigrid Bröcker-Smidt** who always rendered help with the numerous paperwork living in Germany requires.

Special thanks to **Shashank Dadsena** for helping me find my feet in the lab and for the lovely memories outside work. Also, I would like to particularly appreciate the meticulous **Dina Hassan** whom I shared lots of unforgettable memories with during this program. Thank you for always having my back and for the never-ending affirmative words. My gratitude goes to former and current colleagues, **Jan**, **Patrick** and **Michael,** you guys taught me a lot; to **Katharina**, **Elisabeth** and **Manuel**, for all the troubleshooting escapades; to **Christian** and **Milena** for creating nice camaraderie in our office. I would like to acknowledge members of the MIB group- **Steve** and **Aby** for being such jolly colleagues; **Iris** for always initiating pleasant surprises, and **Sylvana** and **Deise** for the friendly banter from time to time. Good luck to you all on your various projects. I would also like to appreciate all the students whom I have had the privilege to supervise over the years. You have provided me with invaluable experience that will serve me for a long time.

My deep gratitude goes to **Pastor Steve Essah**, **Mama Essah** and the entire **Bethesda family** for fellowship all these years. Sincere thanks to **Nana Frimpong** for being an incredible brother and supporter; to **Bob** and **Agatha** for all the memories we shared; to the **Bakare** family for always welcoming me in their home. I would also like to appreciate my dear friend and sister, **Dr Caroline Lumosi** who made Osnabrueck feel like home. Thank you for the often-kind words and good counsel. Special thanks to my friend of more than a dozen years, **Tobi Adeosun**. You are a friend that sticks closer than a brother. I genuinely

appreciate you. In the same vein, I would like to appreciate **Babs Owolodun**, my brother and friend, thanks for your unending support. **Olaitan Ayoola**, thanks for always showing concern for my work. **Ayomide Adeyemi**, you never stopped checking up, I appreciate you. I would like to specially mention **Dr Olubukola Oyebode** who answered my call every time I reached out. Thank you for helping me stay motivated when the steps were steep.

I would like to thank my number-one supporters- my parents, **Mr** and **Mrs J.F. Sokoya** and my siblings, **Esther** and **Dorcas**. You have shown unending belief in me as long as I can remember. This one is for you! To **Prof Ebun Oduwole**, I sincerely appreciate everything that you have done for me all these years. Thank you for good counsel, guidance and mentorship. To the **Ogundeyi**, **Oduwole**, **Womiloju**, **Badejo**, **Anifowose** and **Tanimowo** families, this would not have been possible without you, thank you for always showing concern for my work. Most importantly, I would like to thank my wife, **Temiloluwa**, thank you for standing by me through thick and thin. I am really grateful to have you by my side.

When all is said and done, I give all the glory to **God** whose grace has made this possible!